UNIVERSITY OF OKLAHOMA

GRADUATE COLLEGE

FUNCTIONALIZATION OF MESOSTRUCTURED SILICA CATALYSTS TO

IMPROVE STABILITY AND DECREASE LEACHING DURING C-C BOND

FORMING REACTIONS IN THE LIQUID PHASE

A THESIS

SUBMITTED TO THE GRADUATE FACULTY

in partial fulfillment of the requirements for the

Degree of

MASTER OF SCIENCE

By

SANTIAGO JOSÉ UMBARILA GARCÍA
Norman, Oklahoma
2017

FUNCTIONALIZATION OF MESOSTRUCTURED SILICA CATALYSTS TO
IMPROVE STABILITY AND DECREASE LEACHING DURING C-C BOND
FORMING REACTIONS IN THE LIQUID PHASE

A THESIS APPROVED FOR THE
SCHOOL OF CHEMICAL, BIOLOGICAL AND MATERIALS ENGINEERING

BY

<div style="text-align:right">

_____
Dr. Daniel E. Resasco, Chair

_____
Dr. Steven P. Crossley

_____
Dr. Lance L. Lobban

</div>

To God

He gave me the opportunity to be here serving Him and being a testimony of His word,

the word of truth.

To my family in blood, Gustavo Umbarila, Marcela Garcia, Carolina Umbarila and Felipe Umbarila who support me and encourage me to reach this new step being my strength to accomplish it

To my second family, Hugo Herrera, Yolanda Araque, Catherin Herrera and Valeria Herrera to be my strength, my support, and my guides during all my master degree because they helped me to become this dream real.

Acknowledgements

First, I would like to thank God because He gave me the strength, the knowledge and the wisdom to reach this goal. He gave me the opportunity to learn and share with incredible people in the laboratory. He is my all.

I would like to express my gratitude to my advisor, Dr. Daniel Resasco for giving me the opportunity to pursue my degree under his guidance. For all his mentorship and advice to help me to develop my professional and personal skills to become a better researcher and chemical engineer, his experience and guidance were critical to becoming this dream real.

I would like to thank my committee members, Dr. Steven Crossley and Dr. Lance Lobban, and Dr. Bin Wang for all his advice, for the meetings, and the discussions that addressed the development of this thesis. Special thanks to Dr. Tawan Sooknoi, Dr. Daniel Santanaraj, Dr. Qiaohua Tan and Dr. Xiang Wang for all the critical discussions in the understanding of this thesis.

I would like to thank Valeria Herrera, to be that essential part of my life that never let me fall, who was always there with a word to encourage me, for being my family and my support in all the hard moments, for her patience and her love during all the development of my thesis. She has been with me not only in my professional development but my personal life becoming that family that God gave me because without her this would not be possible.

unconditional love, patience, and encouragement to reach this **goal to shine the dark days with a word of love. I would never forget all they gave me during this time.**

TABLE OF CONTENTS

List of Tables

List of Figures

Abstract

The ordered mesoporous silica materials such as MCM-41 and SBA-15 have raised special attention because of its chemical and thermal stability. Several studies have been reported the ubiquitous modification method of the silica surface through conventional conventional grafting (CG) and co-condensation (CC) functionalization [1–6]. The CG modifies the surface of the silica through sylilation process of the free surface-silanols with organosilanes. On the other hand, the CC method uses the TEOS as the building block for silica structure in the one-pot mixture with organosilanes as functional moieties. The resulting hybrid materials has mesoporous hexagonal structure together with organic functional groups anchoring on the surface.

It has been reported that the created Si-O bonds obtained from conventional functionalization process are thermally stable, mostly in mild conditions, which in turn prevents the loss of those active moieties via the leaching or decomposition. Nevertheless, there are a few works reporting the leaching phenomena happened in more severe chemical conditions in either non-polar or polar solvents. The lack of comprehensive examination, as well as plausible solutions, for the leaching problem in the literature limits the application of the materials for many harsh chemical processes. Therefore, in this study, the fundamentals behind the leaching phenomenon will be investigated at the molecular level by utilizing advanced techniques comprising Fourier-Transform Infrared Spectroscopy (IR), Transmission Electron Microscopy (TEM), Solid-State Nuclear Magnetic Resonance (NMR) of ^{29}Si, ^{1}H and cross polarization ^{1}H-^{29}Si, X-ray Diffraction (XRD).

In this study, a new synthesis method, called dry-grafting method, will be proposed to provide a novel and simple way to synthesize stable non-leaching catalysts for acid-catalyzed reaction, even under severe conditions (polar solvents, high temperature, etc). The catalytic stability is examined by the alkylation between cyclopentanol (CPOL) and m-cresol as a model compound reaction, which is practically relevant to biomass conversion into chemicals and alternative transportation fuels.

CHAPTER 1: Catalytic Upgrading of Biomass

1.1. Introduction

1.1.1. Biomass as an alternative source of chemicals and fuels

Over the past 50 years, the average global temperature has increased at the fastest rate in recorded history as a consequence of the global warming phenomenon. This phenomenon not only affects the global temperature but favors some adverse parallel effects in the environment. They include melting of the glaciers, extreme weather conditions, destruction of the agriculture and extinction of natural habitats. Global warming is linked to the uncontrolled production of CO_2, air pollutants and greenhouse gases that are collected in the atmosphere. Since the greenhouse gases are primarily produced from fossil fuels (coal, natural gas, and oil) their substitution for clean energy sources has raised high attention in the research community for the last decade.

For instance, biomass is highly abundant, renewable and carbon neutral. These characteristics make it a promising alternative to substitute for the petroleum based resources[5–7]. Biomass can be transformed to produce valuable chemicals and fuels by using thermochemical methods as liquefaction, pyrolysis, torrefaction, and gasification. Therefore, different studies predict the biomass will be a major source of chemicals by 2030 being responsible for the production of 20% of fuels and 25% of chemicals in the US[4,8,9].

In the gasification process, the biomass is transformed into synthesis gas (Syngas, a mixture of CO and H_2 in particular quantities)[5]. Syngas undergoes Fisher-Tropsch reaction to produce alkanes or methanol which is further upgraded to fuels via the Methanol-To-Gasoline process to high-quality gasoline[5,10].

1
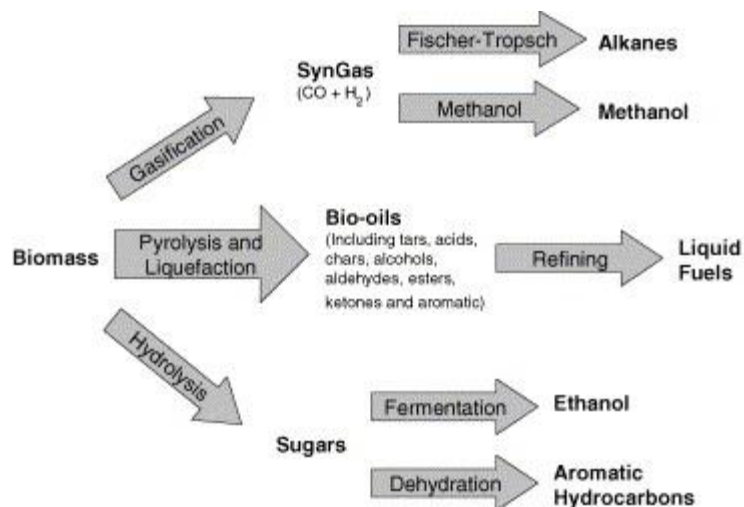
Figure 1 Strategies for the upgrading of biomass to chemicals and fuels[5]

The steps of the gasification process involve drying the raw biomass, the thermal decomposition via pyrolysis, partial combustion of some gases, and finally the gasification. The feedstock biomass is dried to optimize the energy consumption during the gasification because of loss of energy due to vaporization of water during the gasification. The resulted biomass is pyrolyzed to thermally degrade the hemicellulose, lignin, and cellulose from the biomass. The product from the pyrolysis is a mixture of light gases, as CO, H_2 and CH_4, condensable liquids, as tar, oil, and naphtha, and solid char. This mixture is sent to gasification in the presence of air, oxygen or water. Depending on the substrate used to gasify, the heating value of the products will change, obtaining the highest heating value with oxygen and the lowest with air[11–13]. The main advantage of gasification is that the energy is packed in the chemical bonds of the CO and H_2[5,14]. However, gasification is not economically suitable when the production of fuels and chemicals is a desired pathway because of the high cost involved in the further catalytic upgrading. Consequently, the pyrolysis of biomass has attracted more attention due to the high yields of bio-oil obtained[15,16].

The pyrolysis consists of treating the biomass at successively higher temperatures in the absence of air to thermally decomposed the hemicellulose, cellulose, and lignin from the biomass in smaller and more desirable molecules[2,7]. The optimal conditions of the pyrolysis of the biomass have been widely studied to optimize the temperature and residence time of the reactor since those conditions directly affect the distribution of the products. The traditional pyrolysis results in a complex mixture of different compounds with different functionalities known as "bio-oil"[7,15,17]. Those functionalities make the bio-oil chemically unstable that even at room temperature they react together via slow polymerization to form resins hard to upgrade. Therefore, an additional separation strategy is required to improve the catalytic upgrading of the bio-oil.

Conventional thermal separation methods as distillation cannot be implemented because of the low stability of the bio-oil at high temperatures favoring itself polymerization. The extraction with solvents is an alternative to selectively separate the sample through chemical affinity of the solvent with some of the compounds, but this alternative is not efficient because some compounds are not soluble in even organic or water phase creating a triphasic system composed by organic, water and insoluble phase[2,15,16].

New ways to produce a more stable and upgradable bio-oil are important to overcome the challenging separation and its complexity. For instance, Pollard et al. (2012)[16] proposed a new systematic strategy that combines the separation and thermal conversion of the biomass using fast pyrolysis and trapping the vapors in two different stages. The mentioned system consists in rapidly heated of the biomass to ~500°C in the absence of

air with residence times of 1-2 s. The obtained products have a yield of ~70%. The residues of that process are composed of noncondensable gases, solid char, and ashes[16].

A different approach for the bio-oil separation consists in the thermal fractionation of the pyrolysis. This process takes advantage of the various decomposition temperatures of the constituents of the biomass. The hemicellulose decomposes at low temperature, cellulose at medium temperatures and lignin in a broader range of temperatures. In the end, three vapors streams are obtained that can be directly upgraded[15]. The thermal staging of the biomass produces a more stable bio-oil which results in a promising platform for the fuels and chemicals production. Therefore, the next challenge is the understanding and developing of upgradable catalytic routes. Investigating the fundamentals behind the reactions is essential to control and optimize processes, as well as to design and synthesize new catalysts that selectively upgrade the bio-oil to more desirable products[15].

1.2. Catalytic upgrading of the thermal fractionation of the pyrolysis.

1.2.1. Catalytic upgrading of the first stage of the fractionated fast pyrolysis

The thermal fractionation of biomass produces three different stages. The first cut is attributed to the decomposition of the hemicellulose at 270°C which mainly produces light acids. The acetic acid is the most abundant compound from this cut and is one of the most problematic compounds in the bio-oil because of its acidity. It is responsible for the corrosive properties of the bio-oil while promotes the polymerization of the others compounds. Consequently, the catalytic upgrading of those stages is required to increase

4

the stability of the bio-oil while decreasing the oxygen content and increases the carbon retention[15].
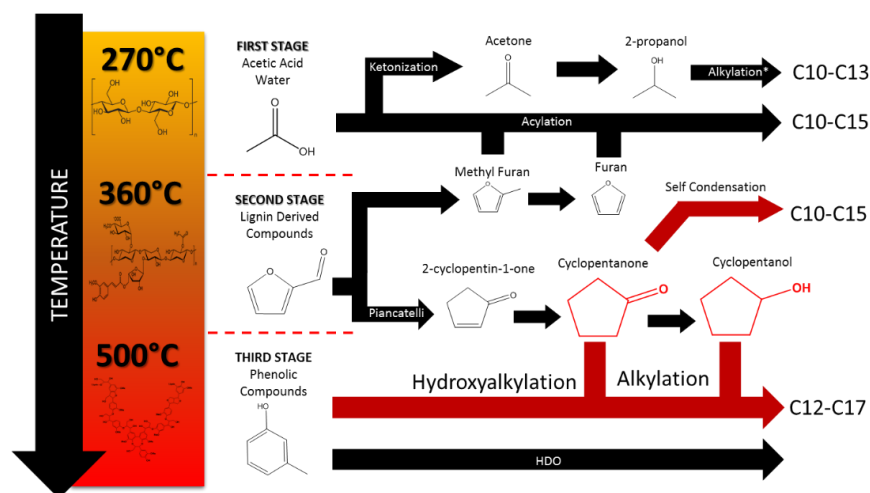
Figure 2 Catalytic upgrading of the different stages obtained from the thermal fraction of the pyrolysis. The graph was constructed based on the references [17,20–24]

One of the proposed pathways to upgrade acetic acid is via ketonization to produce acetone, CO_2, and H_2O. Although; acetone is a highly desired product because of its widespread industrial uses as solvent or reagent, the ketonization has the disadvantage to lose carbon in the form of carbon dioxide[18,25,26]. Therefore, Abhishek et al. (2016) proposed a combined upgrading strategy between the first and the second stage (See second stage explanation below). It is plausible for the ketonization mechanism that acetic acid undergoes via acyl formation route to produce acetone. The formation of that species on the catalyst surface is redirected, under the low temperatures, to make favorable the acylation of the furanics over the ketonization[21].

1.2.2. Catalytic upgrading of the second stage of the fractionated fast pyrolysis

The second stage of the fractionated pyrolysis of biomass corresponds to the dehydration of the cellulose and some hemicellulose fragments[15]. This stage contains heterocyclic compounds of four and five carbons (Furanics and pyranics respectively) which are highly reactive and quickly polymerize forming humins. Itself polymerization of the furanics and pyranics is accelerated with the increment of the temperature[24,27,28].

Several studies have focused in the upgrading of the second stage of the biomass using furfural as a model compound to selectively produce cyclopentanone, furfuryl alcohol or methyl furan[6,15,18,28,29]. It has been found the furanics from the second stage undergo via different hydrogenolysis and decarbonylation reactions to produce several ring opening products. Another interesting approach is the hydrogenation of the carbonyl group of furfural followed by the hydrogenation of the furanic ring that subsequently undergoes ring opening reaction to produce 1,5-Pentanediol used as a monomer in the polymer industry[30–34].

The cyclopentanone production is one of the most desired pathways because cyclopentanone is widely used as a building block for the aldol condensation reaction. The conversion of furfural to cyclopentanone can be carried out using a metal catalyst such Ru, Ni or Pd which, in the presence of H_2 will hydrogenate the carbonyl group of the furfural leading the formation of furfuryl alcohol. The former product undergoes via ring rearrangement reaction in an acid environment to form 2-cyclopente-1-one that under H_2 environment produces cyclopentanone as is proposed by Hronec (2012) in liquid phase[24]. Recent evidence in our group, have shown the furfural can directly produce cyclopentanone in the gas phase.

1.2.3. Catalytic upgrading of the third stage of the fractionated fast pyrolysis

The decomposition of the lignin from the biomass leads the production of oxygenated aromatics that typically contains one to three oxygens found in the way of phenolic or methoxy groups. The phenolics produced on this stage are highly desired due to their chemical similarity with the actual gasoline products. Those products can be directly added to the gasoline pool upon deoxygenation[15,22].

One possible pathway to eliminate the oxygen from the oxygenated aromatics while remaining constant the carbon content of the stream is the trans-alkylation and deoxygenation of the methoxy groups and phenolics groups. To evaluate the trans alkylation strategy Boonyasuwat et. al (2013) [35] studied a couple of bifunctional metal/oxide catalysts such as Ru/SiO_2, $Ru/\gamma-Al_2O_3$, and Ru/TiO_2. They proposed as a pathway of reaction the direct deoxygenation of guaiacol over the metal via C-O hydrogenolysis reaction to produce catechol and anisole and a secondary trans-alkylation to form xylenols, cresols, phenols, methylguaiacol, methylcatechol as well of catechol. Those products undergo via hydrodeoxygenation to produce aromatics that are used in the gasoline pool[35,36].

Another interesting approach is the combined upgrading strategy between the first and the third stage of the thermal fractionated pyrolysis of the biomass through the alkylation of the highly electronegative aromatic ring with light alcohols. This approach involves the presence of Bronsted solids as Hβ and HY zeolites which have been shown to have good activity for these reactions[23].

1.2.4. Bronsted acid solids as a catalyst for the upgrading of biomass derive compounds

Zeolites have a high performance for the alkylation and aldol condensation reactions. However, it has been shown that condensed hot water collapses its crystalline framework [37–40]. The destruction of the structure was previously explained by Zhang et. al (2015)[41]; they reported the determining factor for the zeolite stability under hot liquid water is the density of the defects in the surface that is the free silanols. The high hydrophilicity presented for those Si(OH) structures allow the water molecules to nucleate and wet the surface. They are not only responsible for the wetting but also are more reactive toward water favoring the hydrolysis of the SiO_2 structures. An alternative to improve the stability of the zeolite to water attack is the functionalization of the silanols with hydrophobic trichloro organosilanes. The functionalization not only helps to keep the water off from the catalyst but also reduces the free silanols on the surface on the zeolite causing a decrease in the hydrolysis rate of the SiO_2 structures. However, under equilibrium conditions water diffuses into the zeolite producing the collapse[37].

The ordered silica MCM-41 and SBA-15 have raised a particular attention because of its properties such as high surface area, mechanical, thermal and chemical stability, and high adsorption capacity. However, the acidity of these materials is low which makes them inactive for most of the reactions. On the other hand, the stability of MCM-41 and SBA-15 to water attack has been proved to be higher than in zeolites[42]. Therefore, the functionalization of these materials is a promising alternative to increase the acidity that at the same time increases the hydrothermal stability.

Different methods have been proposed to functionalize the ordered mesoporous silica. The post-synthetic functionalization or grafting is based on the modification of the surface silanols in the silica surface, prior synthesized, using tri-alkoxy organosilanes $(R_1O)_3(SiR_2)$ or chloro organosilanes $(Cl_nSiR_{(4-n)})$ (n=3, 2, 1) [43]. During the grafting of MCM-41, the Si(OH) structures react with the precursors forming a stable Si-O-Si bond between the functionalization and the mesostructured silica.

Another proposed method is the direct synthesis or co-condensation. This approach uses the organosilanes as a building block of the silica in a one pot mixture with the TEOS; the resulting material is a hybrid organic-inorganic crystalline material composed of organosilanes and silanes groups. However, it is claimed those catalysts are efficient only in nonpolar organic solvents due of the extensive leaching of the active sites in polar solvents [44,45].

As a result, this work investigates the catalytic activity and the molecular characterization of functionalized MCM-41 via conventional grafting (CG), and co-condensation for potential application in the upgrading of biomass derived compounds. It is proved those methods are inefficient in the presence of either polar or nonpolar environments. Therefore, a new alternative method to functionalize mesostructured silica is presented to produce a stable catalyst that will not leach under those environments. The molecular characterization is provided via characterization techniques as XRD. FTIR and CP NMR. Also, the stability of this new material was tested with the alkylation of cyclopentanol and m-cresol as a model compound since it is a highly desired reaction for the catalytic upgrading of biomass.

CHAPTER 2: Alkylation and Aldol condensation reactions

2.1. Abstract

Biomass is a suitable alternative to produce fuels and chemicals through the thermal fractionation of the pyrolysis following by the catalytic upgrading of the different stages. The upgrading of biomass requires the increase of the carbon number in the molecule while the total carbon is conserved in the former products. As a result, the aldol condensation of ketones and aldehydes and the alkylation of aromatics with alcohols are a promising route to catalytically upgrade biomass derived compounds[15]. In this chapter, a theoretical framework and preliminary results of those sets of reactions are presented as potential pathways to produce compounds into the gasoline pool.

2.2. Introduction

2.2.1. Aldol condensation reaction as strategy to increase the carbon content

The condensation of ketones via de aldol condensation reaction produces a α, β-unsaturated oxygenates with higher carbon number and lower oxygen content. Those products undergo via hydrodeoxygenation forming compounds with characteristics in the fuel range. However critical deactivation of the catalyst has been reported[3].

The aldol-condensation reaction of carbonyl groups, over a basic metal oxide catalyst, consists of four different steps. The $^\alpha$H-abstraction to form the enolate, frequently called enolate formation, the C-C coupling, re-protonation and dehydration (Figure 3). The first step initiates with the adsorption of the carbonyl groups over the Lewis acid metal on the

catalyst. The strong interaction of the high electronegative oxygen atom pulls over the acid α-Hydrogen from the adsorbate forming the enolate on the catalyst surface[3].
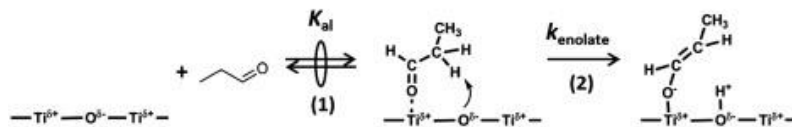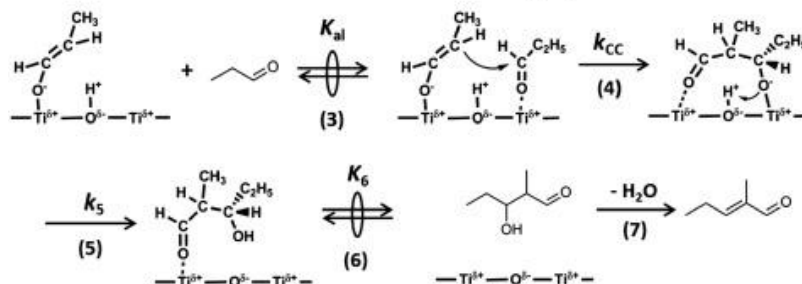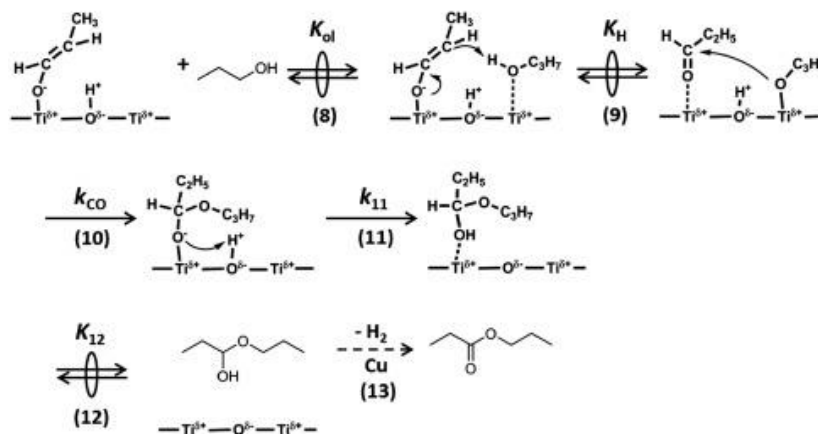
Figure 3 Aldol-condensation and esterification reaction mechanism of propanal over TiO₂ (anatase)[3]

The forming enolate in the surface interacts with an adsorbed carbonyl, resulting in an electrophilic attack by the carbon in the enolate to the carbonyl adsorbed species to form a new C-C bond. The previously abstracted $^{\alpha}$H is re-protonated to the adsorbate compound, following by desorption of the hydrated ketonic species which are dehydrated to form the α,β-unsaturated oxygenates. The former unsaturated product is attributed to be the responsible for the fast-catalytic deactivation presented in this reaction.

11

The deactivation of the catalyst has been explained because of the presented unsaturation on the aldol-condensation products leading the coke formation and subsequent deactivation of the catalyst. In order to avoid the fast deactivation of the catalyst, the hydrogenation of the unsaturated products was evaluated using a 10% Cu/SiO_2 in physical mixture with TiO_2 (P25). It has been reported, in the hydrogenation of propanal, that the presence of a hydrogenation metal such a Cu (10% Cu/SiO_2) leads to the formation of 1-propanol (Hydrogenation of propanal) and the double bond unsaturation presented in the products. The carbonyl hydrogenation reaches a fast-equilibrium conversion resulting in a kinetically similarity of 1-propanol and propanal[3,44,45]. Therefore, there was observed a negligible deactivation mainly because of the hydrogenation of the double bond in the products.

The presence of the alcohol in the reaction medium, open a new pathway through the esterification of the enolate on the surface and the subsequent alcohol (Figure 3). Wang *et al*. (2016) showed the selectivity of the products (esterification/aldol condensation) changes following the ratio between 1-propanol/propanal, however, the overall rate of consumption of the reagent does not alter the mentioned ratio. The authors claimed the esterification and aldol-condensation reactions share the same rate determining step (RDS). As a result, the C-C bond formation cannot be the RDS because it happens exclusively on the aldol condensation leading to the conclusion that α-Hydrogen abstraction is the RDS for the mentioned catalyst over TiO_2(P25) and TiO_2 (anatase) since it is the common intermediate in both catalytic routes.

On the other hand, evidence has shown the nature of the catalyst directly changes the RDS in the reaction. Herrmann *et.al*. (2017)[46], have found a shift in the RDS in the

aldol condensation reaction over solid Bronsted acids as aluminosilicates following an Eley-Rideal mechanism. The proposed mechanism starts with the protonation of the ketone over a Bronsted acid site that further undergoes tautomerization. The resulting tautomer on the surface interacts with another ketone from the bulk producing the aldol product. They claimed the RDS for this reaction is the C-C bond formation. The resulted tertiary alcohol quickly dehydrates over the acid site producing the α,β- unsaturated oxygenate[46]. Despite the results shown via isotopic effect and DFT calculations, recent studies from our group in the aldol condensation of cyclopentanone suggested the nature of the RDS strongly depends on the nature of the adsorbate producing a shift in the RDS.

It is evident the fast deactivation of the catalyst during the aldol condensation is problematic. An alternative is the use of mesoporous hexagonal silicas over the aluminosilicates because of the higher pore size to decrease the deactivation. The functionalized MCM-41 is a potential solution to avoid the deactivation due to the relatively higher pore size (30A) and the high surface area (~750 m^2/g). In this chapter, preliminary results of the aldol condensation of cyclopentanone over sulfonated MCM-41 are shown as an alternative for the catalytic upgrading of the biomass derived compounds.

2.2.2. Alkylation of phenolic with alcohols and olefins

From the first stage of the thermal fractionated pyrolysis of the biomass acetic acid represents one of the most abundant compounds. One alternative to the upgrading of the acetic acid is the ketonization reaction over oxides to produce acetone which has been shown to be an important catalytic route on this stage[15]. The production of 2-propanol from acetone is efficient under hydrogenation pathways and highly desirable due to the

stability of this alcohol. However, the carbon content is low to be used as a fuel. One strategy to increase the carbon number is the alkylation between small light alcohols, which are known to be effective alkylating agents[38,47,48], and the phenolics produced in stage 3. This approach not only results beneficial due to the increasing in the carbon retention in the liquids but also dramatically enhances the bio-oil stability by decreasing the acidity[15].

The increasing of temperature may favor the degradation and polymerization reactions in the bio-oil which results problematic for fuels production from biomass[15]. Therefore, it is required to investigate the alkylation on the liquid phase. Gonzalez *et al.* (2015)[23] investigated the kinetics of the alkylation of m-cresol and 2-propanol over HY30 catalyst. They reported two catalytic routes for the alkylation, the C-O alkylation and the C-C alkylation being the former one faster, but the reversible character of this pathway makes the C-C alkylation products to be the main products during this alkylation[22,23,47,49].

Although, secondary alcohols such 2-propanol are effective alkylating agents it is important to consider the dehydration reaction of this type of alcohols that occurs quickly over a Bronsted solid acid. In the alkylation of m-cresol with 2-propanol, the dehydration reaction is too fast that the former olefin becomes the major alkylating agent. This product not only alkylates m-cresol but also favors the oligomerization reaction which creates high molecular weight products that block the active sites and deactivate the catalyst.

The abundant water in the bio-oil is problematic for the zeolites because of the low hydrothermal stability presented for this type of catalyst[37,39]. One alternative is the substitution of the aluminosilicates materials for sulfonic functionalize mesostructured

silica as MCM-41-SO₃H. That class of materials has higher hydrothermal stability, and similar acid strength than its counterpart, the zeolist[50]. However, one disadvantage of this materials is the lack of the confinement characteristics offered by zeolites as HZSM-5, HY30, and Hβ. Consequently, more research is required to analyze the performance of the sulfonated mesostructured silica. In this section, the alkylation of m-cresol with two alcohols, 2-propanol, and cyclopentanol was carried out under liquid phase conditions using MCM-41-SO₃H as a catalyst. It was found that the catalyst behaves similarly than HY30 but with the advantage of better hydrothermal stability.

2.3. Materials and Experiments

2.3.1. Catalyst synthesis

The conventional grafted MCM-41-SH (CG) was fabricated as follows; the commercial MCM-41 was mixed with toluene and the organosilanes in the ratio of 25 mL of Toluene/g of MCM-41 and 5.38 mmol of organosilane/g of MCM-41. The solution was placed in a reflux system with stirring and N_2 bubbling at 40°C for 12 h. and further washed a room temperature with Methanol and deionized water. The material was dried overnight at 80°C. The synthesis of MCM-41-SH (DG) was performed as explained in *Chapter 3*, the commercial MCM-41 was impregnated via dry incipient impregnation with a mixture of 2.5 mL of Methanol/g of MCM-41 and the desired functionalization (5.38 mmol of functionalization/g of MCM-41). The resulting solid was placed in the Parr Reactor working as an autoclave and heated up to 180°C followed by a high-temperature wash with decalin/MeOH solution (50% v/v).

The resulting MCM-41-SH (CG/DG) was oxidized using H_2O_2 as an oxidative agent in a ratio of 25 mL/g of MCM-41-SH for 24 h. The resulted MCM-41-SO₃H catalyst

was washed at room temperature dried overnight at 80°C. The acid content was evaluated using TPO-TGA in a Netzsch STA-449 F1 Thermal Analysis.

2.3.2. Catalytic activity measurements

The liquid phase alkylation and aldol condensation reaction were carried out in a Mini bench top Parr pressure reactor of 160 mL (Model Parr 4564) equipped with a Parr 4848 Reactor Controller for temperature, stirring and a transducer for pressure measurement. In a typical experiment, the catalyst MCM-41-SO$_3$H (150 mg) was mixed with the solvent (80 L) and pressurized with N$_2$. The mixture was heated to 200°C/250°C. In a separated vessel, the reactants were bent making a solution (with base of the reaction conditions) of 1M of m-cresol and 0.5M of Cyclopentene/Cyclopentanol/2-propanol (CPEN/CPOL/2-propanol) for the case of the alkylation and 0.5M of cyclopentanone(CPO) for the aldol condensation. The solvent was added until complete 100 mL of total volume in the reaction. The reactants solution was placed in a separate vessel and injected into the reactor reaching a final pressure of 800 psi.

After of reaction, the reactor was cooled down to room temperature and depressurized to atmospheric pressure. The catalyst was separated from the liquids using a syringe filtration system to avoid vaporization of products. The liquid was analyzed with GC-FID for product quantification and GC-MS for products identification[51].

2.4. Results and Discussion

2.4.1. Alkylation of m-cresol with IPA
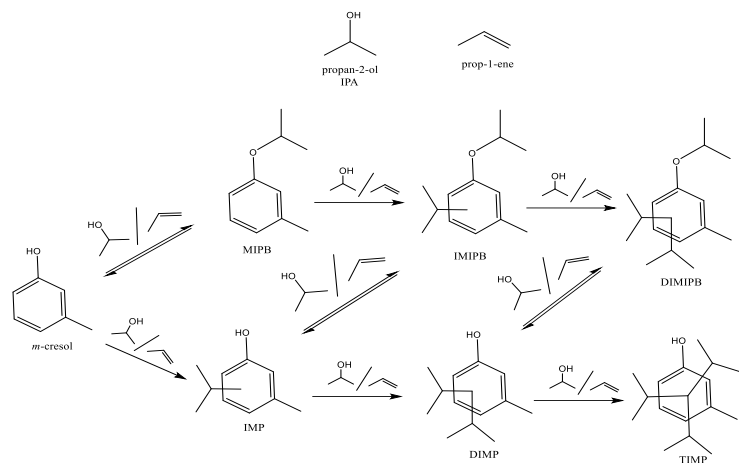
16

Figure 4 Pathway of reaction for the alkylation of m-cresol and 2-propanol. Taken from Gonzalez-Borja et. al. (2015)[23]

The dehydration of IPA to produce propylene over Bronsted acid sites has been shown to be fast under the tested reaction conditions[23]. Those compounds act as an alkylating agent to the aromatic ring of m-cresol or the phenolic group. As a consequence, two routes are identified in the alkylation of m-cresol with IPA (Figure 4 Pathway of reaction for the alkylation of m-cresol and 2-propanol. Taken from Gonzalez-Borja et. al. (2015)**[23]**).
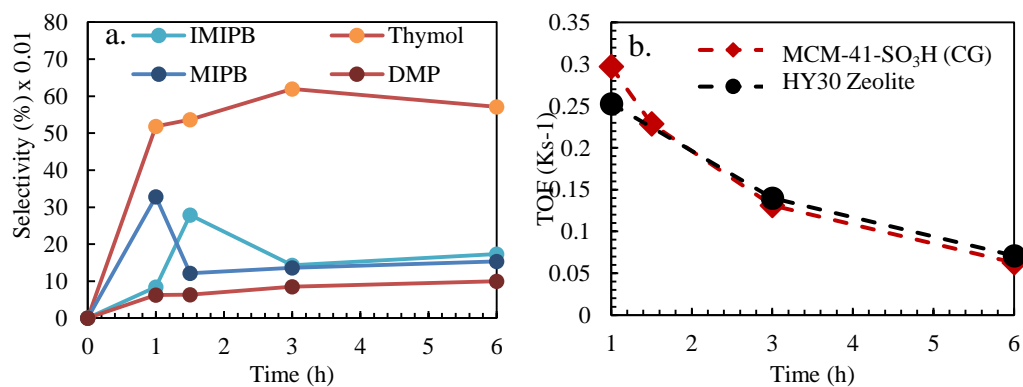
Figure 5 a. Product distribution for the alkylation reaction of m-cresol with IPA at 200°C and 850 psi of N_2, b. TOF during the alkylation of m-cresol with IPA at 200°C and 850 psi of N_2 and 50 mg of MCM-41-SO$_3$H (1.01 mmol H$^+$/g cat) and 10 mg of HY30 (0.248 mmol H$^+$/g cat)

The first pathway is the reversible C-O alkylation followed by a C-C alkylation and the second route is the directly C-C alkylation to form the primary product thymol which is sequentially alkylated to form DIMP and TIMP. As noted by Gonzalez-Borja et al[23] the major product during the reaction was thymol corresponded to the first C-C alkylation product. Also, the decrease in the concentration of the MIPB after 1 h of reaction is a solid evidence of the reversibility of the reaction (Figure 5.a). The product distribution for the alkylation of m-cresol with IPA over MCM-41-SO$_3$H (CG) is similar in comparison with the zeolite HY30 discarding any possibility of shape selectivity effects.
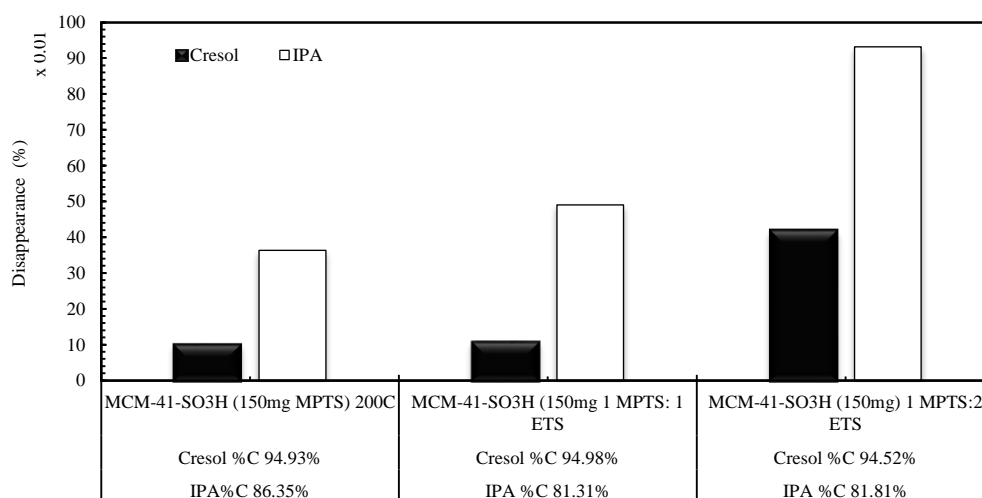
Figure 6 Effect of the hydrophobization of the MCM-41-SO₃H with Ethyl trichloro silane. The number below the labels indicate the carbon balance for each compound.

The understanding of the possible consequences of the water during the reaction over MCM-41-SO$_3$H (CG) was carried out via the functionalization of the catalyst with hydrophobic moieties in mixture with sulfonic groups. The presence of the hydrophobization on the catalyst increases the rate of reaction because it reduces the adverse effect the water does over the catalyst concluding that as the hydrophobic

moieties in the catalyst increase the amount of water on the surface decreases. As an explanation for that phenomenon, the hydrophobic groups helps to avoid poison of the catalyst because of water or may favor the desorption of the products avoiding the deactivation.

2.4.2. Alkylation of m-cresol with CPOL

The upgrading of biomass derived compounds through the alkylation of m-cresol and IPA is an interesting strategy that combines the upgrading of the first and third stage of the fractionated biomass. Parallels, the upgrading of the second and third stage is possible through the alkylation of m-cresol and CPOL. Similarly to the alkylation of m-cresol with IPA, CPOL is dehydrated to produce cyclopentene and undergoes via etherification to produce diciclopentyl ether. The former olefin and the alcohol act as alkylating agents. The ring of m-cresol is alkylated via C-O or C-C alkylation forming the products described in Figure 7. No evidence has been seen to stand that cyclopentene can undergo via C-O alkylation indicating this alkylation possible undergoes via etherification mechanism.
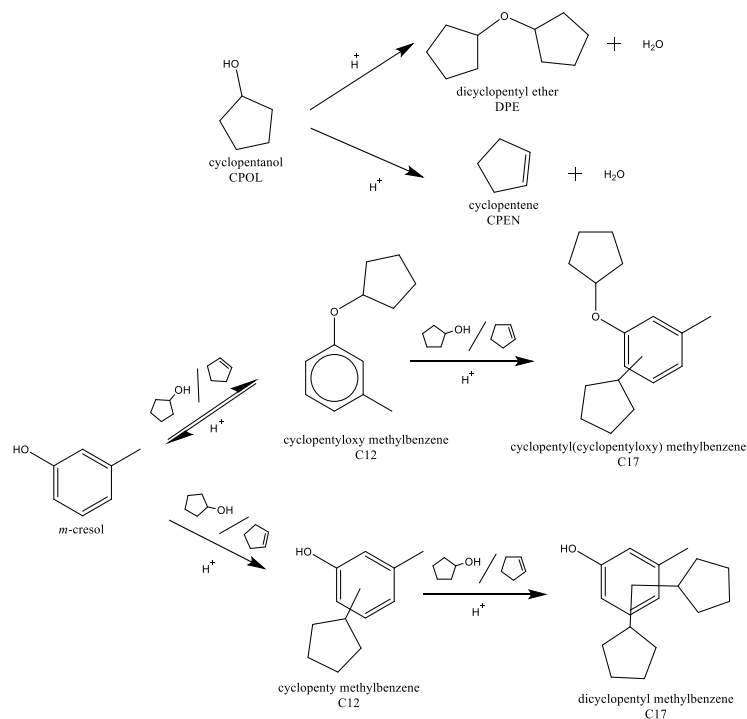
Figure 7 Pathway of reaction for the alkylation of m-cresol and CPOL

The product distribution for the alkylation of m-cresol and CPOL is shown in Figure 8. The main product of the reaction was CPEN followed by the main alkylated products C12 and small yields of C17 corresponded to the second alkylation reaction. It is noticeable from the Figure 8 and Figure 9.a the dehydration reaction is faster than the alkylation, and quickly create an environment reach on cyclopentene. As a result, recognizing that cyclopentanol and cyclopentene act as alkylating agent, the principal alkylating agent for this reaction is CPEN. However, more detailed kinetical experiments are required to understand this reaction completely.

20
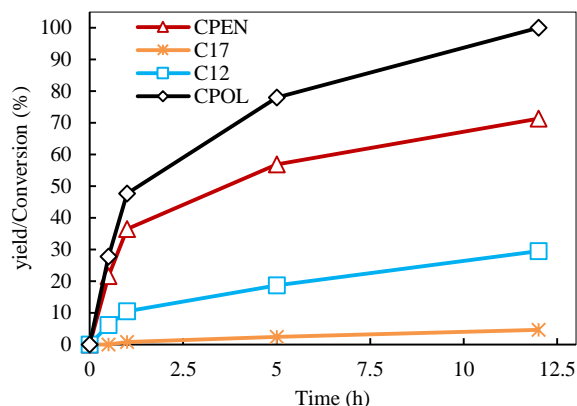
Figure 8 Product distribution for the alkylation of m-cresol (1.0M) and CPOL (0.5M) at 200ºC and 850 psi of N$_2$ with 150 mg of MCM-41-SO$_3$H (1.01 mmol H$^+$/g cat).

The C-O alkylation of m-cresol results to be predominant over the C-C alkylation (Figure 9.b). However, the ratio between C-O to C-C alkylation decreases as the conversion increases. That change of selectivity over time can is explained because the C-O alkylation is reversible leading to enhance the formation of irreversible C-C alkylated products. Also, the environment becomes richer in the olefin than the alcohol leading to the increase of the C-C net alkylation rate over the C-O net alkylation rate. To clarify the nature of this reaction, a detailed micro kinetics study is required.
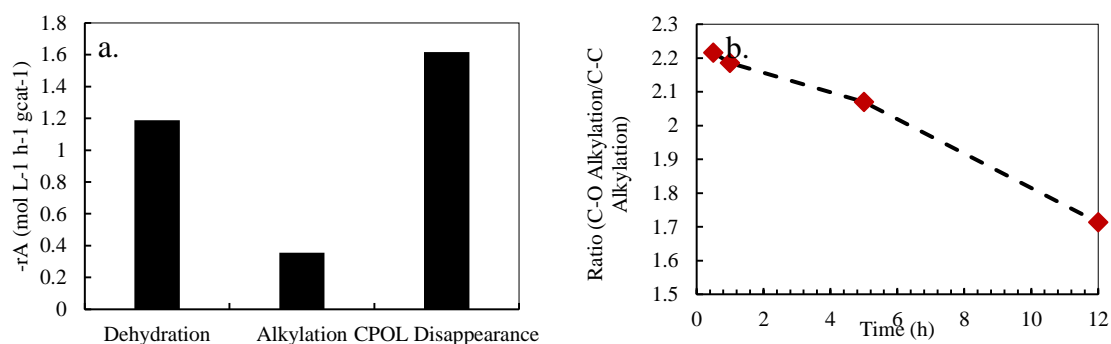
Figure 9 a. rate of dehydration and alkylation of cyclopentanol and b. Ratio of C-O alkylation and C-C alkylation for the alkylation of m-cresol (1.0M) and CPOL (0.5M) at 200ºC and 850 psi of N$_2$ with 150 mg of MCM-41-SO$_3$H (1.01 mmol H$^+$/g cat)

2.4.3. Aldol condensation of cyclopentanone (CPO) over MCM-41-SO$_3$H

21

The self-condensation of CPO take place over oxides and Bronsted acid sites as was shown in our group. During the self-condensation, CPO is activated leading to a nucleophilic attack to form the tertiary C10-alcohol. The former alcohol undergoes dehydration to form the conjugated C10 products that can interact with another CPO to produce the C15 products. The formation of the alcohol during the aldol-condensation route is well known in the literature. However, no detectable amounts are observed after the reaction, indicating the dehydration becomes easy and fast during the aldol condensation (Figure 10).

An interesting product was detected and is identified as *Tri* in Figure 10. The mechanism to produce trisannelated benzene is illustrated in Figure 11. Once the C10 product is formed there are two possibilities for the second aldol condensation reaction, the activation of the cyclopentanone or the activation of the C10 product. Depending on which one is activated it will lead the formation of C15 and i-C15 product shown (Figure 11). The isomer i-C15 in the surface of the catalyst can undergo via cyclization/dehydration mechanism to form a more stable aromatic product without oxygen content and high carbon number. It results in an attractive alternative for the upgrading of cyclopentanone. However, the yield of this product is low even at high temperatures as is shown in

Figure 12.
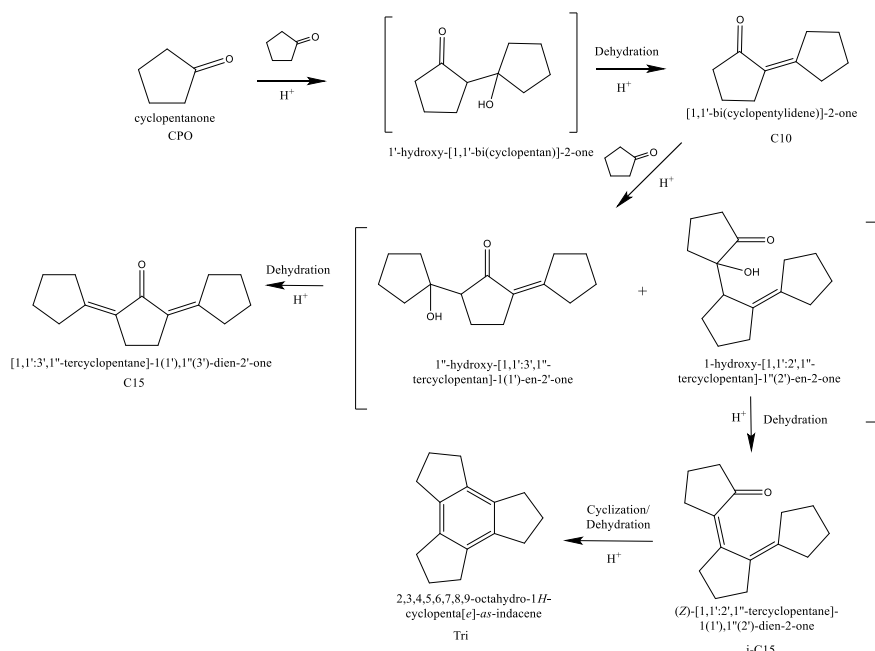
Figure 10 Pathway of reaction for the self-aldol-condensation of CPO over MCM-41-SO₃H (DG)
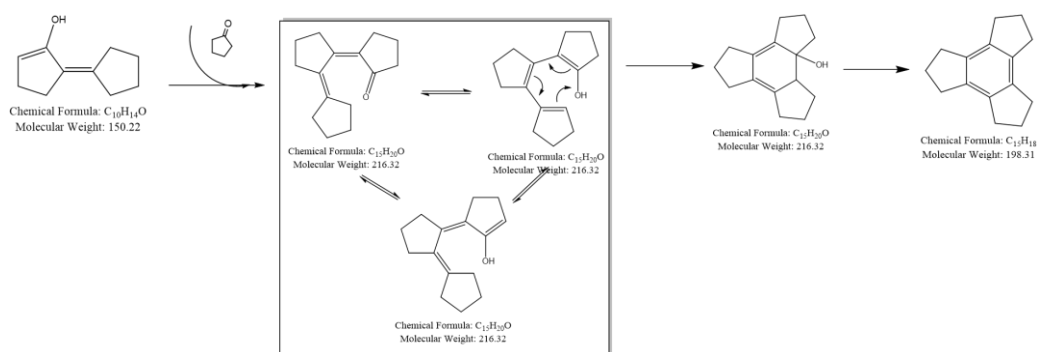
Figure 11 Reaction mechanism for the formation of the trisannelated benzene.

The aldol condensation of CPO was tested at different temperatures, and the results are presented in

Figure **12**. The formation of aldol condensation products is low at 150°C with only presence of the first condensed products. However, the increase of the reaction

23

temperature dramatically decreases the activity of the catalyst as well of the carbon balance. With the negligible formation of C15 products. Low temperatures enhance the selectivity of C10 products increasing, increase the carbon balance and the catalyst life during the reaction. The deactivation of the catalyst results problematic due of the fast deactivation after 30 min where the conversion keeps increasing but no presence of products was identified. As a result, the understanding of the catalyst deactivation is required to enhance the life of the catalyst.
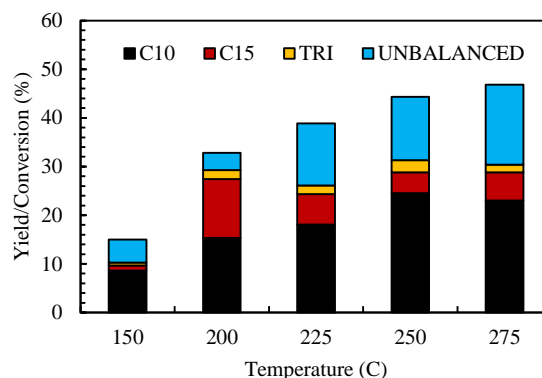
Figure 12 Product distribution for the self-condensation of cyclopentanone (0.5M) over MCM-41-SO$_3$H (DG, 1.05 mmol H$^+$/g cat) after two h of reaction and 850 psi of N$_2$

To further understand the nature of the deactivation, the temperature of 250°C was chosen to carry out the experiments, and Figure 13 is presenting the product distribution. After 30 minutes of reaction, the yields of the products on the reaction does not represent a significant change, but the conversion of CPO keeps increasing. That behavior can be attributed to a thermodynamic equilibrium of the reaction. However,

more experiments are required to clarify if the reaction reaches the thermodynamic equilibrium.
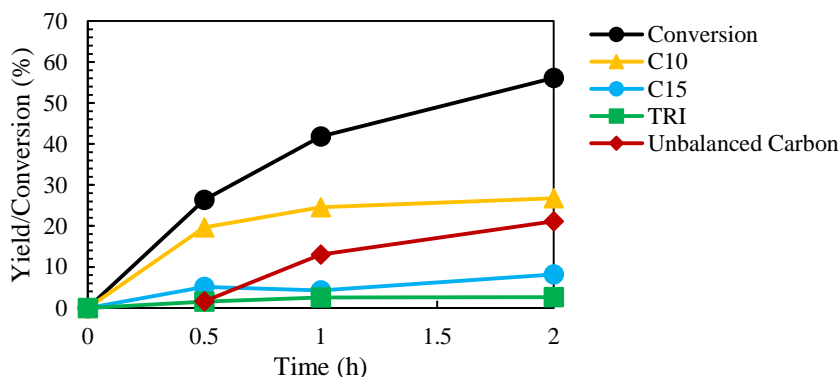
Figure 13 Product distribution of cyclopentanone (0.5M) over MCM-41-SO₃H (DG, 1.05 mmol H⁺/g cat) after 2 h of reaction at 250°C and 850 psi of N₂

It is hypothesized the deactivation of MCM-41-SO₃H (DG) is because the strong interaction of the products with the catalyst hindering the product desorption and favor the coke formation. An evidence of this phenomena was observed when the used catalyst was washed with acetone, and the resulted liquid was analyzed with a GC-MS. Compounds with MW of 150 (C10), 216(C15) and 286 were identified in the surface of the catalyst. The last one is associated with oligomers in the catalyst are too heavy to desorb from the catalyst.

The hydrophobization is a promising strategy to increase the life of the catalyst through the anchoring of carbon chains that may favor the products desorption. Figure 14 presented the results when a hydrophobized catalyst was tested; Those results were evaluated under the same acid density and preliminary results shown no difference in the activity of the catalyst. The similarity observed is explained because of the presence of isolated hydrophobic islands on the surface of the materials where no real effect is applied

in the catalyst. To test this procedure is required to fabricate a catalyst via co-impregnation of the acid moieties with the hydrophobic carbon chains to obtain a homogeneous surface without isolated islands.
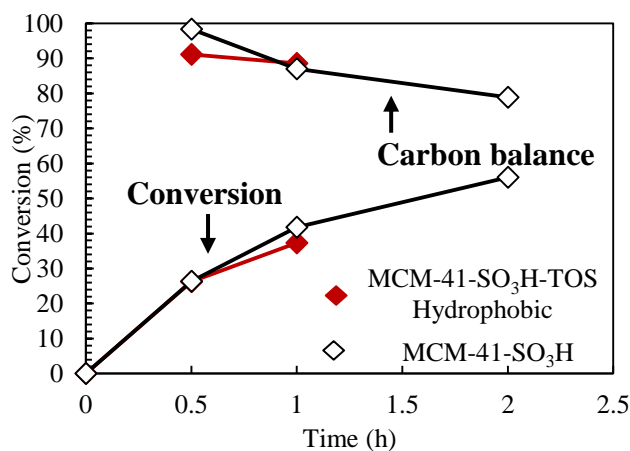
Figure 14 Hydrophobization effect on the surface of the sulfonated MCM-41 (0.6 mmol of H$^+$/ g cat). The catalyst was prepared via sequential impregnation in the dry grafting procedure impregnating first the MPTS followed by the triethoxy(octyl)silanes (TOS). The reaction was carried out at 250°C, 850 psi of N$_2$ and initial concentration of CPO of 0.5M

2.5. Conclusions

The MCM-41-SO$_3$H is a promising strategy for the upgrading of the biomass deriving compounds due to the similarity presented with the HY30 zeolite presenting a similar acid strength with the advantage of higher hydrothermal stability. However, the water presents an effect that requires being understood in deep to understand the real role of the water when interacting with acid groups. On the other hand, this catalyst presents a fast deactivation in the aldol condensation reaction, even though it is justified because of the strong adsorption of the products with the catalyst, more studies are required to understand, and possibly increase the catalytic activity of the catalyst to avoid the deactivation.

CHAPTER 3: Novel functionalization method of mesostructured silica with trialkoxi-organosilanes to produce a stable acid catalyst for C-C bond forming reactions

This work has contributions of *Tuong V. Bu, Tawan Sooknoi*[†] from School of Chemical, Biological and Materials Engineering, University of Oklahoma, 100 East Boyd Street, Norman, Oklahoma, 73019, United States.

3.1. Graphical Abstract
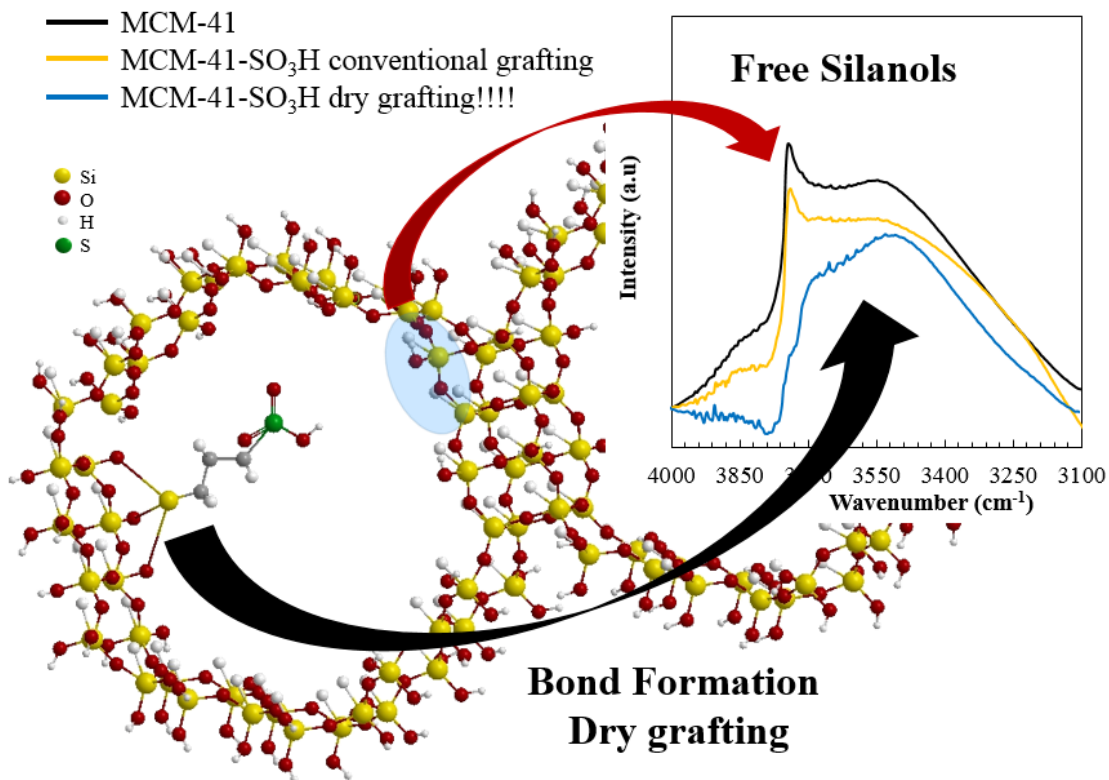
3.2. Abstract

Ordered mesoporous silica such as MCM-41 and SBA-15 have attracted attention because of its unique structure and stability. However they need to be functionalized in order to be active for acid/catalyze reactions. Several studies have reported the functionalization of the silica through conventional grafting (CG) and co-condensation

(CC) methods. The CG method modifies the surface via silylation of the free silanols with organosilanes. In contrast, the CC method uses TEOS as a building block for generating the silica structure in a one-pot mixture with organosilanes, which act as functional moieties. The resulting hybrid material has the characteristic mesoporous hexagonal structure together with organic functionalities in the surface.

The former Si-O bonds during CG functionalization have been reported to be stable, but only under rather mild conditions, therefore not leaching of active moieties is observed. There are only a few studies reporting leaching under more severe reaction conditions in either nonpolar polar solvent. In this study, the leaching process was investigated at the molecular level by utilizing a combination of techniques including Fourier-Transform Infrared Spectroscopy (IR) Transmission Electron Microscopy (TEM), Solid-State Nuclear Magnetic Resonance (NMR) of ^{29}Si, ^{1}H and cross polarization ^{1}H-^{29}Si, and X-ray Diffraction (XRD).

Also, a new synthesis method named as "dry grafting" is proposed. This approach provides a novel and simple way to synthesize stable non-leaching materials useful as catalysts in acid-catalyzed reactions, even under severe conditions such as polar solvents and high temperatures. The catalytic stability is examined for the alkylation reaction of m-cresol and cyclopentanol (CPOL) which has practical relevance for biomass conversion into fuels and chemicals.

Key words: MCM-41, SBA-15, functionalization, conventional grafting, co-condensation, dry grafting, leaching, alkylation

3.3. Introduction

In response to the rising industrial demand for renewable and clean energy in the recent years, many efforts have been made to develop commercial processes and catalysts that efficiently produce bio-based chemicals and transportation fuels through the catalytic upgrading of the biomass derived compounds. Lately, mesoporous materials have attracted the attention of scientists as interesting catalytic materials[4–8]. Unlike their microporous counterpart, the mesoporous catalysts are less affected by mass transfer constraints, which is a tremendous advantage in the biomass conversion when dealing with large molecules. Among the family of siliceous and highly-ordered mesoporous materials, MCM-41 and SBA-15 are promising alternatives for heavy hydrocarbon production due to their mechanical, thermal, chemical stability and tunable pore size[9–16]. The more open porous structure allows the accommodation of bulky intermediate transition state as well as fast diffusion within catalyst cavities leading to the enhancement of the rate of those quick reactions which are usually limited by mass transfer in microporous catalysts [17]. Their well-defined channels and the tunable pore-size could potentially increase the selectivity of the desired products during reactions[18]. Furthermore, the high density of surface free silanols provides the capability to modify the acidity of the material through silylation to anchor acid sites such as sulfonic groups, which has been found to be relevant for many acid-catalyzed reactions[19–22]. Two major techniques have been reported to be used in order to synthesize this type of hybrid inorganic-organic mesoporous materials comprising: co-condensation and grafting method[8,11,23–26].

Both methods presented high stability of the former Si-O bonds between the mesostructured silica and the functional moieties. Nevertheless, some studies in more severe chemical conditions and using either non-polar [1–3] or polar solvents[27] showed strong evidence of leaching. Those studies are summarized in **Table 1**. According with literature, the leaching of functional groups is facilitated at high temperature and in presence of polar solvents, where the hydrolysis of either Si-C or C-C bonds are accelerated, resulting in the loss of active sites to the solution. The origin of this problem is still unclear and require a comprehensive examination to reach plausible solutions.

Table 1 Literature overview of the catalytic activity of the functionalized mesostructured silica.

Reaction	Catalyst[a]	Solvent	T (°C)	Stability	Reference
Esterification acetic acid with methanol	SiO_2-SO_3H[b]	Methanol	60	No leaching	86
Esterification of fatty acids with methanol	SBA-15-SO_3H[c] SBA-15-SO_3H[d] SiO$_2$ -SO_3H[d]	Methanol	60	No Leaching Leaching	72
Etherification of glycerol with isobutene	SBA-15-SO_3H[e] SBA-15-SO_3H[d]	Glycerol	75	No Leaching	87
Aldol condensation of phenol with acetone	MCM-41-SO_3H[c] MCM-41-SO_3H[d]	Phenol	70-100 150	No Leaching	88
Esterification of fatty acids with ethanol	PS/nPMA-SiO_2 HNs[c,f] PS–C$_8$–SiO_2 HNs[c,f] PMA–C$_8$–SiO_2 HNs[c,f]	Ethanol	80	Leaching No Leaching	58
Dehydration of fructose	SBA-15-SO_3H[c] SBA-15-SO_3H[d]	H2O DMS[h]	120	Leaching No Leaching	89
Esterification of flotation beef tallow with methanol	SBA-15-SO_3H[d] SBA-15-SO_3H-Pr[d]	Methanol	120	Leaching	90
Hydrolysis of cellobiose	SiO_2-NP-SO_3H[g]	Water	175	Leaching	91

[a] **The catalyst was synthetized using MPTS as a precursor following by oxidation to SO_3H**
[b] **Incipient wetness impregnation of the precursor at room temperature**
[c] **Catalyst functionalized using CC method**
[d] **Catalyst functionalized using CG method**
[e] **Conventional grafting assisted by microwaves**
[f] **hybrid mesoporous silica hollow nanospheres (HNs), PS: Polystyrene, PMA: poly(methyl acrylate), C8: functionalized with TOS**
[g] **Conventional grafting using different solvents (Ethanol, methanol, acetonitrile, toluene) of silica-coated magnetic nanoparticles of $CoFe_2O_4$**

Therefore, in this study the source of leaching phenomenon at the molecular level was investigated. A new synthesis method, denominated as dry grafting, is proposed as a novel and simple way to synthesize stable catalysts for acid-catalyzed reaction, even under severe conditions. The alkylation of cyclopentanol and m-cresol was used as a probe reaction to investigate the stability of the functionalized catalysts to polar and nonpolar environments at high temperature (200-250°C) toward the leaching phenomenon.

3.4. Materials and Experiments

3.4.1. Chemicals and Materials

MCM-41 (Type A) and SBA-15 purchased from ACS Materials were dried at 400°C for 12 h in N$_2$ flow (99.999%, Airgas). (3-Mercaptopropyl) Trimethoxysilane (95% purity, Aldrich, MPTS), ethyl (trichloro)silane (99%, Sigma-Aldrich, ETS), Trimethoxy(octyl)silane (90% purity, Aldrich, TOS) and Trimethoxy(propyl)silane (97% purity, Aldrich, TPS), were used as provided. Anhydrous toluene (99.8%, Sigma-Aldrich) and methanol anhydrous (99.8%, Sigma-Aldrich) were employed as solvent and diluent agent in the catalyst synthesis procedure. Before being used, toluene and methanol were pretreated with silica-alumina molecular sieves (Zeochem) and activated overnight at 300°C. A hydrogen peroxide aqueous solution (30 wt. %, EMD Millipore) was utilized as an oxidized agent to convert the thiol groups of MPTS to R-SO$_3$H groups. m-cresol (99%), cyclopentanol (99%) and decahydronaphthalene, mixture cis + trans (99%) were obtained from Sigma-Aldrich.

3.4.2. Conventional grafting of mesostructured silica (MCM-41)

In a typical synthesis, the pretreated MCM-41 was dispersed in toluene (25 mL of Toluene/g of MCM-41) and heated up to 40- 110°C with constant stirring and N_2 bubbling in a reflux system. Once the temperature was stable, the desired organosilane compounds were injected into the dispersion (5.38 mmol/g of MCM-41). The solution was then stirred at a constant temperature with constant N_2 bubbling for 12 h. The solid was separated by using a vacuum filtration system (Pore size of filter 0.22 μm) and washed with toluene, acetone, and water to remove the residual organosilane on the surface. The resulting catalyst (MCM-41-SH) was dried at 80°C overnight. The -SH groups were converted to active sulfonic groups via the oxidation process in a solution of H_2O_2 (25 mL/ g of MCM-41-SH) at 40°C for 12 h. The resulted catalyst (MCM-41-SO$_3$H) was filtrated under vacuum conditions and washed with an excess amount of acetone and deionized water to remove H_2O_2 remaining. After that, the catalysts were dried overnight at 80°C in a vacuum oven.

3.4.3. One-step co-condensation of SBA-15-SH

The co-condensation procedure was conducted as reported by Stucky (2000)[35]. The Pluronic 123 (4 g, PEG: 30 wt %. Aldrich, P123) was dissolved in a solution of 1.9 M of HCl and prepared at room temperature. The temperature of the solution was stabilized to 40°C. Tetraethyl orthosilicate (>99.0%, Aldrich) was added to the mixture and pre-hydrolyzed for 45 mins, followed by the addition of the trialkoxy-organosilane (MPTS). The mixture was stirred for 20 hrs at 40°C and aged at 100°C for 24hrs without stirring. The solid (SBA-15-SH) was recovered by filtration. The surfactant template was removed by washing with methanol in reflux system (400 mL of Methanol/1.5 g SBA-15-SH).

3.4.4. Post-synthetic functionalization of mesostructured silica via novel dry grafting (DG)

Herein, we are proposing new synthesis method to synthesize active and stable functionalized catalysts. In a typical synthesis, dried MCM-41 was impregnated via incipient impregnation with a solution of trialkoxy-organosilanes (5.11 mmol/g of MCM-41and methanol (2.5 mL/g of MCM-41). The obtained solid was placed in a sealed Mini Bench Top Parr reactor 4564 and heated to 180°C for 12 hrs. The boiling point of the MPTS was employed as a reference to choose the operating temperature. After the thermal treatment, the obtained solid was washed in-situ with methanol under stirring at 200°C. Further oxidation of the thiols groups was carried out with a solution of 30% H_2O_2. The catalyst washed at room temperature with methanol and dried at 80ºC overnight.

3.4.5. Characterization of the mesostructured silicas

The surface area, pore size, and volume pore were evaluated using N_2 physisorption at -198°C in a micromeritics ASAP 2020 through the Brunauer-Emmett-Teller method (BET). Prior adsorption, the samples were degassed for 6h under vacuum conditions at 250°C. A Perkin–Elmer Spectrum 100 FTIR equipped with a high-temperature DRIFT (diffuse reflectance infrared Fourier transformation) cell (HVC, Harrick) with CaF_2 windows was used to study the surface chemistry of the functionalized silica. The samples were pretreated in-situ at 250°C for 1 h under He flow (30 mL/min) to remove water physically adsorbed on the catalyst surface. The cell was cooled down to 50°C, and the DRIFT spectra were collected 64 times with a resolution of 1 cm^{-1} as reported by Zapata

et. al (2013)[36]. Solid state NMR was used to evaluate the silicon structures and the functionalization modes presented on the catalyst after of each synthesis process.

The structural characterization was examined with Small Angle X-ray diffraction experiments (XRD) recorded in D8 Series II X-ray diffractometer (BRUKER AXS), in reflection geometry using CuKα radiation generated at 40 kV and 35 mA in the 2θ range from 2° to 60°. The topology and morphology of the catalysts were studied by scanning electron microscopy (SEM) and transmission electron microscopy (TEM). The SEM was conducted on a FIB Zeiss NEON 40 High-Resolution Scanning Electron Microscope operated at 5 kV. The TEM was analyzed in a JEOL JEM-2100 Scanning Transmission Electron Microscope operating at 200 kV, and the images were recorded using a CCD camera. The samples were prepared by suspending 2-5 mg of sample in 10 mL of 2-propanol, followed by the deposition over a copper grid coated with carbon and dried at 80°C.

The organic content of the catalysts was evaluated via thermogravimetric analysis coupled with temperature program oxidation (TGA-TPO) using a Netzsch STA-449 F1 Jupiter. In a typical experiment, the functionalized material (30 mg) was placed in a crucible with a constant flow of Ar (40 mL/min) and air (10 mL/min). The cell was preheated to 40°C then increased to 700°C with a ramping rate of 3°C/min. The combustion gases (CO_2, SO_2) were analyzed with an on-line mass chromatograph Aeolos QMS 403C.

3.4.6. Catalytic reaction measurements

The liquid phase alkylation was carried out in a Mini Bench Top Parr pressure reactor of 160 mL (Model Parr 4564) equipped with a Parr 4848 Reactor Controller at 200oC,

300 psi with the reactant concentration of 1.0 M m-cresol and 0.5 M Cyclopentanol (CPOL). The collected liquid was analyzed with a GC-FID and GC-MS equipped with a Phenomenex capillary column (ZB-1701, 15 m x 0.25 mm x 0.25 µm).

The leaching test was designed to investigate the stability of the studied catalysts at severe reaction condition. The experiments include two steps. First, the alkylation reaction was carried out at 200-250°C, 1hr, and 850 psi under solvent or free condition. After of the reaction, the catalyst was separated out of the reaction mixture. A fraction of the obtained liquid was collected for GC analysis while the remaining liquid product was placed back in the clean reactor, re-run at 250°C for 12 h, 850 psi without the addition of catalysts (Step 2). The concentrations of products and reactants were compared between the first and second step. The increase of any alkylated product concentration suggests that the leaching of sulfonic group happened, where the reaction is homogeneously catalyzed.

3.5. Results and Discussions

3.5.1. Catalytic test of the acid functionalized mesostructured silica

The reaction pathways for the alkylation of m-cresol and CPOL are presented in the Figure 15 Firstly, CPOL undergoes via itself etherification and dehydration over the catalyst surface to produce di-cyclopentyl ether (DPE) and CPEN respectively. Besides, CPOL and CPEN alkylate m-cresol via C-O or C-C alkylation forming the initial C12 products. Further C-C alkylation of those products forms the C17 products shown in Scheme 1. No trace of tri-alkylated products was detected even at high conversions (~90%).
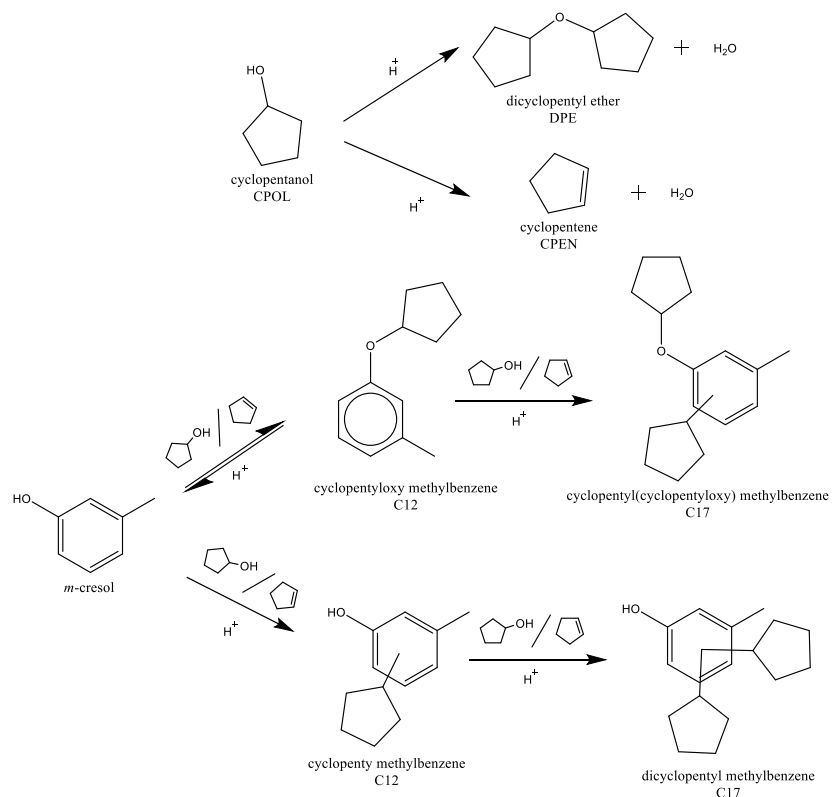
Figure 15 *Pathway of reaction for the alkylation between m-cresol and CPOL*

A series of mesoporous silica-based catalysts with different preparation methods were screened for the catalytic performance as well as the stability for the alkylation reaction including MCM-41-SO$_3$H (CG), MCM-41-SO$_3$H (DG), and SBA-15-SO$_3$H (CC). **Figure 1** shows the relative change of product yields in the designed leaching test with different catalysts and under different conditions. Upward bars represent the positive net production while the downward ones stand for the disappearance of a species.

It is noticeable that under free solvent conditions MCM-41-SO$_3$H (CG) and SBA-15-SO$_3$H (CC) severely leach the functional moieties as is observed by the increment in the concentration of the alkylated products C12 and C17. Since no thermal reactions were detected under the evaluated conditions, the difference in those concentrations is related to homogeneous activity caused by the solubilized sulfonic functional groups in the

reaction mixture. Interestingly, the leaching of MCM-41-SO₃H (CG) seems to stop under

nonpolar solvent (decalin). The polarity of CPOL and m-cresol lead to the formation of a

harassment environment that at high temperature may favor the leaching of the functional

moieties either by solubilization of the physically adsorbed sulfonic groups near the

surface or hydrolysis of the SiO_2 structure. During reaction under free solvent conditions,

the water produced is enough to form condensed water on the system. The condensed

water can nucleate on the surface and favore the hydrolysis of the Si-O-Si structures[37]. In

contrast, the distinction in polarity of the sulfonic functionality and decalin harnesses the

leaching.
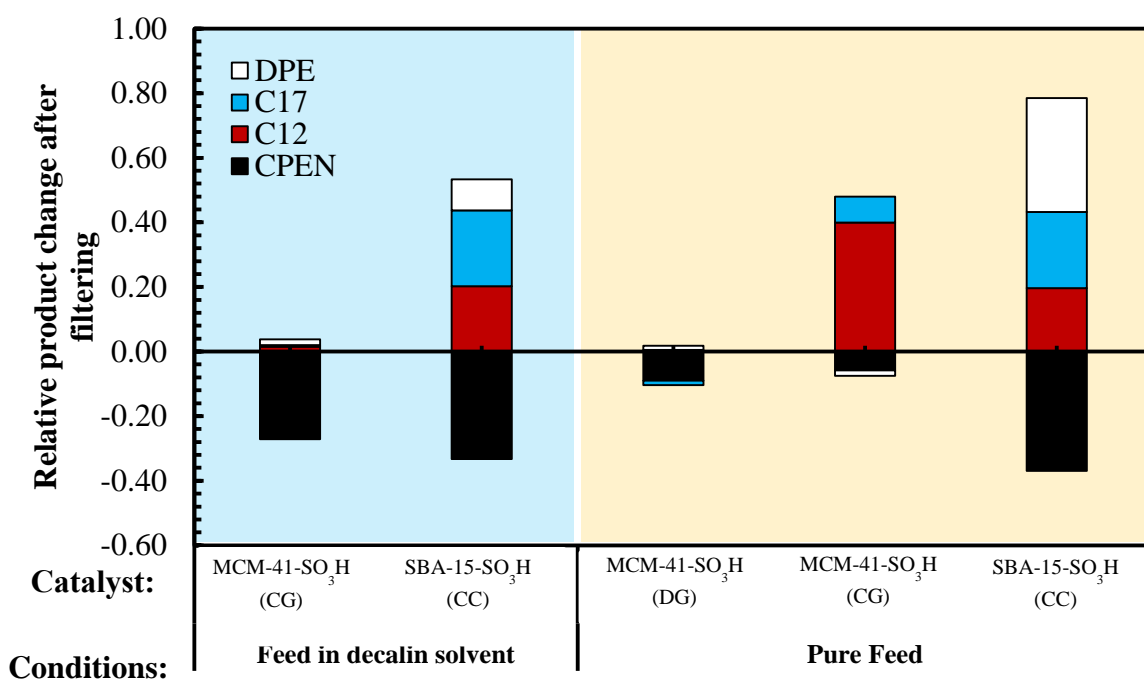
Figure 1. The net production of products after leaching test. The reaction was first carried out at 250°C, 850 psi of N₂ for 2hrs. The obtained filtrate was then re-run without the addition of solid catalysts at 250°C, 850 psi of N₂ for another 14hrs

The loss of the functional moieties on SBA-15-SO₃H (CC) through leaching still

occurs severely in both polar and non-polar solvents. Surprisingly, the catalysts

synthesized by dry-grafting method did not present a net production of alkylated products

after the leaching test even under polar solvent conditions (**Figure 1**). The minor CPEN

consumption, in this case, is due to polymerization. The stability presented by DG

catalysts is an interesting □DPE ■C17 ■C12 ■CPEN ◆Conversion ı solidly anchored

on the surface regardless of their strong interaction with the polar medium including m-

cresol, CPOL, and in-situ generated water.
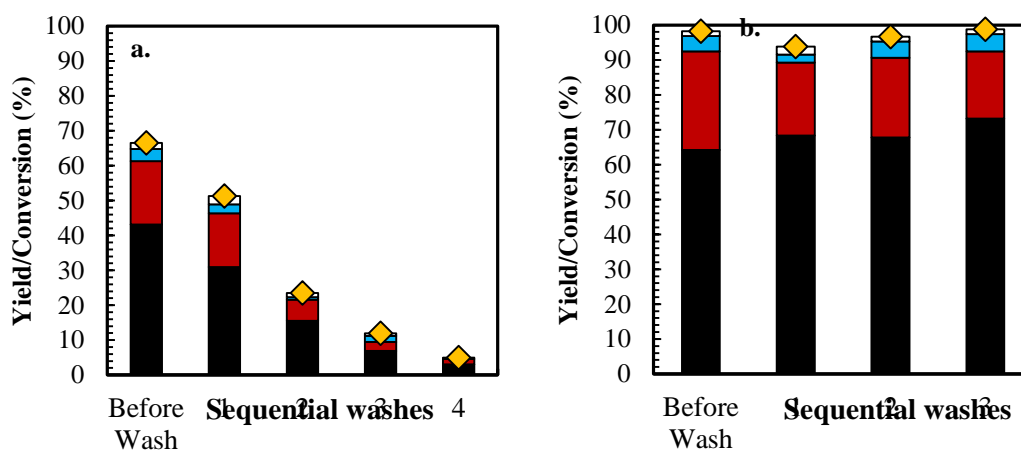
Figure 2. Catalytic activity for the alkylated products over the functionalized MCM-41after multiple sequential washes with methanol at 200°C for 6 h a) MCM-41-SO₃H (CG) and b) leaching test result for MCM-41-SO₃H (DG). The reactions were carried out at 200°C under 850 Psi of N₂ and CPOL and m-cresol concentrations of 0.5 and 1.0 M respectively.

The stability of the MCM-41-SO₃H synthesized from CG and DG methods was

further tested via multiple sequential washes with MeOH at 200°C (**Figure 2**). After each

wash, the solid was recovered and used it to run the alkylation reaction at 200°C and 850

psi of N₂. The strong interaction of methanol with the sulfonic groups via hydrogen

bonding will facilitate the leaching of the functionalization that is physically adsorbed on

the surface. Another important factor is the presence of free silanols on the surface that

under methanol environment may enhance the hydrolysis of the Si-O-Si structure as was

presented for Zhang (2015)[37]. As expected, the activity of MCM-41-SO₃H (CG)

gradually drops after each methanol wash, demonstrating the leaching of functional

moieties when contacted with the strongly polar medium as methanol. In contrast, the catalytic performance of MCM-41-SO$_3$H (DG) remains unchanged.

Furthermore by using NMR and FT-IR, the ineffectiveness of conventional grafting method in forming a chemically stable Si-O bond was shown. The leaching of the functional moieties could be overlooked when operating at low temperatures as is mostly reported in the literature. It is evident that the temperature is a key factor in the leaching phenomenon favoring it. Probably, the leaching of the functional moieties could be explained by the covalent bond formation with the mesostructured silica and the available free silanols on the surface which, in the case of CG catalysts, is not efficiently produced resulting in a high density of free silanols on the MCM-41 surface.

3.5.2. Structure analysis of the functionalized MCM-41 and SBA-15

The N$_2$ adsorption isotherms for the functionalized MCM-41 and SBA-15 materials (Figure S1) show the type IV isotherms characteristic of the mesoporous materials. It is observed that an increase of the functionalization degree (Table S1) is followed by a decrease of surface area and pore size, which is associated with the occupation of alkyl and alkyl-sulfonic functionalization on the surface.

The XRD spectrum of MCM-41 displays a Bragg's diffraction at 2.16°, 3.76° and 4.34° on the planes indexes (1 0 0), (1 1 0) and (2 0 0) respectively observed for the hexagonal arrangement of the mesostructured silica (**Figure *16***). This structure is confirmed unaltered in all the cases as shown by HRTEM (Figure S4). The decrease in XRD peak intensity of the functionalized silica (MCM-41-ETS (CG) and MCM-41-SO$_3$H (DG)) at (1 0 0), (1 1 0) and (2 0 0) plans is an indication for crystallinity lost due to the

grafting with the organosilanes, creating a more amorphous surface[38–41]. Interestingly, the decrease of crystallinity on MCM-41-SO₃H (DG) is more significant compared to the others, which consequently agree with BET results. That is, higher functionalization degree reduces the crystallinity at the surface as well as the porosity, surface area, and pore volume of the modified materials.
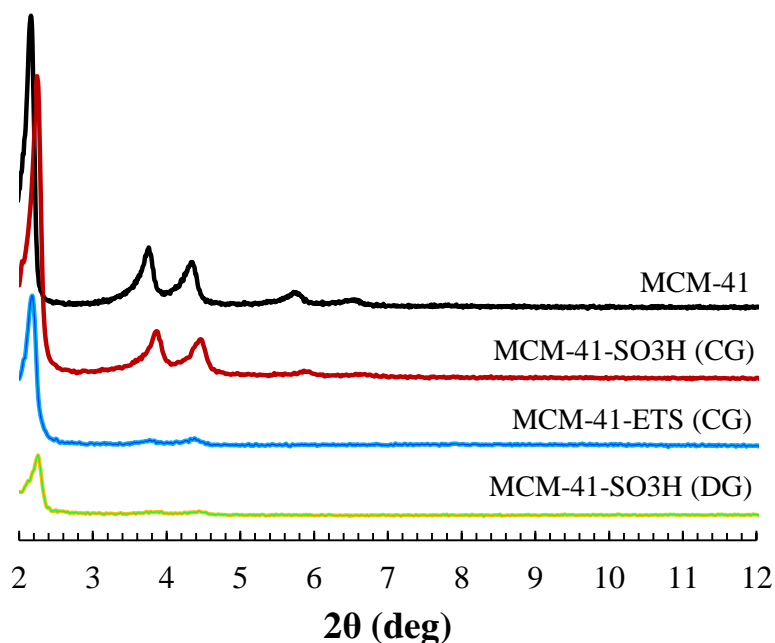
Figure 16 SAXS spectra for the functionalized and no functionalized MCM-41.

A typical TGA-TPO experiment for a functionalized silica shows three different regions. The first region ranges from 40°C to 150°C at which the physically adsorbed water on the surface desorbs. It can be seen that the presence of alkyl-sulfonic functionalization increases the amount of physisorbed water whereas the alkyl functionalization decreases it (Figure S1). This effect is more evident when the catalysts were functionalized with longer C_8 alkyl chain (TOS) than with ETS where no water was released. The second observable region (typically from 200° to 550°C) corresponds to

the thermal degradation of the functionalization. In this region, the Si-C, C-C, and C-S

bonds are thermally decomposed into CO_2, SO_2, and H_2O. The mass loss and

corresponding signal of emitting gases were used to quantify the amount of

functionalization on the mesostructured silica (**Table 1**). The final region starts at 550°C,

in line with thermal dihydroxylation of the single and germinal silanols on the surface[42].

The composition and retention of the functionalization for the different

synthesized catalysts are summarized in **Table 1**. First, it is noticeable the

functionalization with trialkoxy organosilane (ex: MPTS) precursor through CG method

presents low efficiency of silylation (~6%). In contrast, ETS precursor is more efficient

for the grafting process, resulting in the highest retention of the functionalization (~38%).

This is due to the greater reactivity of trichloro organosilanes with the surface silanol in

comparison with trialkoxy organosilanes. The low degree of functionalization of CG

method might be caused for the low silylation temperature (40°C) that is only effective if

trichloro organosilanes precursors are used. By increasing the functionalization

temperature in the well-controlled environment (DG method), a clear improvement in the

retention of the functionalization with trialkoxy organosilanes is exhibited because the

formation of the covalent bonds between the functionalization moieties and the MCM-41

surface is facilitated. No much difference in grafting efficiency between those two

synthesis methods when trichloro organosilanes such as ETS or TOS are used.

Table 2. Composition of the mesostructured silica after functionalization through CG, CC, and DG

Material	Synthesis method	Precursor (mmol/g cat)[a]	Functionalization (mmol/g cat)[b]	Retention of functionalization (%)[c]
MCM-41	Commercial	-	3.11-3.74[d]	-
MCM-41-SO$_3$H	CG	MPTS (5.11)	0.31	6.25
MCM-41-ETS[c]	CG	ETS (5.11)	2.71	38.92
SBA-15-SO$_3$H	CC	MPTS (5.11)	0.97	-
MCM-41-SO$_3$H	DG	MPTS (5.11)	0.82	17.87

MCM-41-TOS	DG	TOS (5.11)	1.40	32.67

CG: Conventional Grafting, CC: Co-condensation, DG: Dry Grafting.
[A] Functionalization added to the synthesis process
[b] Calculated from the TGA-TPO results (See Figure S2).
[c] Amount of functionalization after of the leaching of the moieties.
[d] Theoretical estimation of the OH^{-} groups on the surface reported by Ref [39,42]

The disappearance of the surface free silanols (**Figure 2**) is expected due to the consumption of –OH group via the silylation process to form Si-O-Si-R$_1$ bonds, along with the appearance of regions corresponding to C-H bonds vibration. According to literature, the DRIFT spectra in the area between 4000 to 3100 cm^{-1} and 3150 to 2400 cm^{-1} are assigned to the stretching vibration of surface –OH and CH$_2$/CH$_3$ respectively[33,36]. Examination of the catalyst surface by FT-IR shows that all the samples functionalized with trialkoxy organosilanes by CG method resulted in high content of free surface silanols. It has been previously stated in this work that CG is not a suitable method to anchor trialkoxy organosilanes moieties due to their weak activity. Weak vibration signal intensity of alkyl chains in the region of 3150 to 2400 cm^{-1} strongly supports this observation since their surface properties are relatively analogous to those of un-functionalized MCM-41. These results can be related to the lack of bond formation during the functionalization (**Figure 2a**).

In contrast, switching grafting moiety from trialkoxy to trichloro organosilanes, results in an apparent disappearance of free surface silanols and a noticeable increase in the C-H vibration signal. This is further evidence for the higher reactivity of the trichloro-organosilanes in comparison with the trialkoxy-organosilanes. The low functionality degree of MCM-41-SO$_3$H-CG samples demonstrates that the temperature is simply not high enough to successfully overcome the energy barrier of the silylation reaction between Si-OCH$_3$ and the surface silanols. Increasing the synthesis temperature up to

110°C seems not sufficiently to speed up the grafting process. The inactive functional groups remaining on the surface would exist in the form of physical adsorbed via Van de Walls forces or might undergo water-assisted itself polymerization to form POSS (Polyhedral Oligomeric Silsesquioxane) structures [4,43,44]. Either of these existing structures would allow the solubilization in a polar solvent. It is worth noting that this leaching process is slow in the low-temperature process. Therefore, washing the solid with polar/non-polar solvents at low temperature would not effectively help to clean the surface of the adsorbed functional moieties.

The high activation energy of the new Si-O bond formation between Si-$(OCH_3)_3$ and surface OH, requires a higher temperature to be activated. The use of solvents in synthesis procedure typically limits the grafting temperature according to their boiling point. Therefore, avoiding the utilization of a solvent and restricting the presence of water during the synthesis are the two fundamentals behind the dry grafting method. This solvent-free procedure allows to push up the upper limit of functionalization temperature to the boiling point of functional moieties. Additionally, the absence of water in surrounding environment hinders the formation of POSS structure on the catalyst surface and therefore, preventing the leaching.
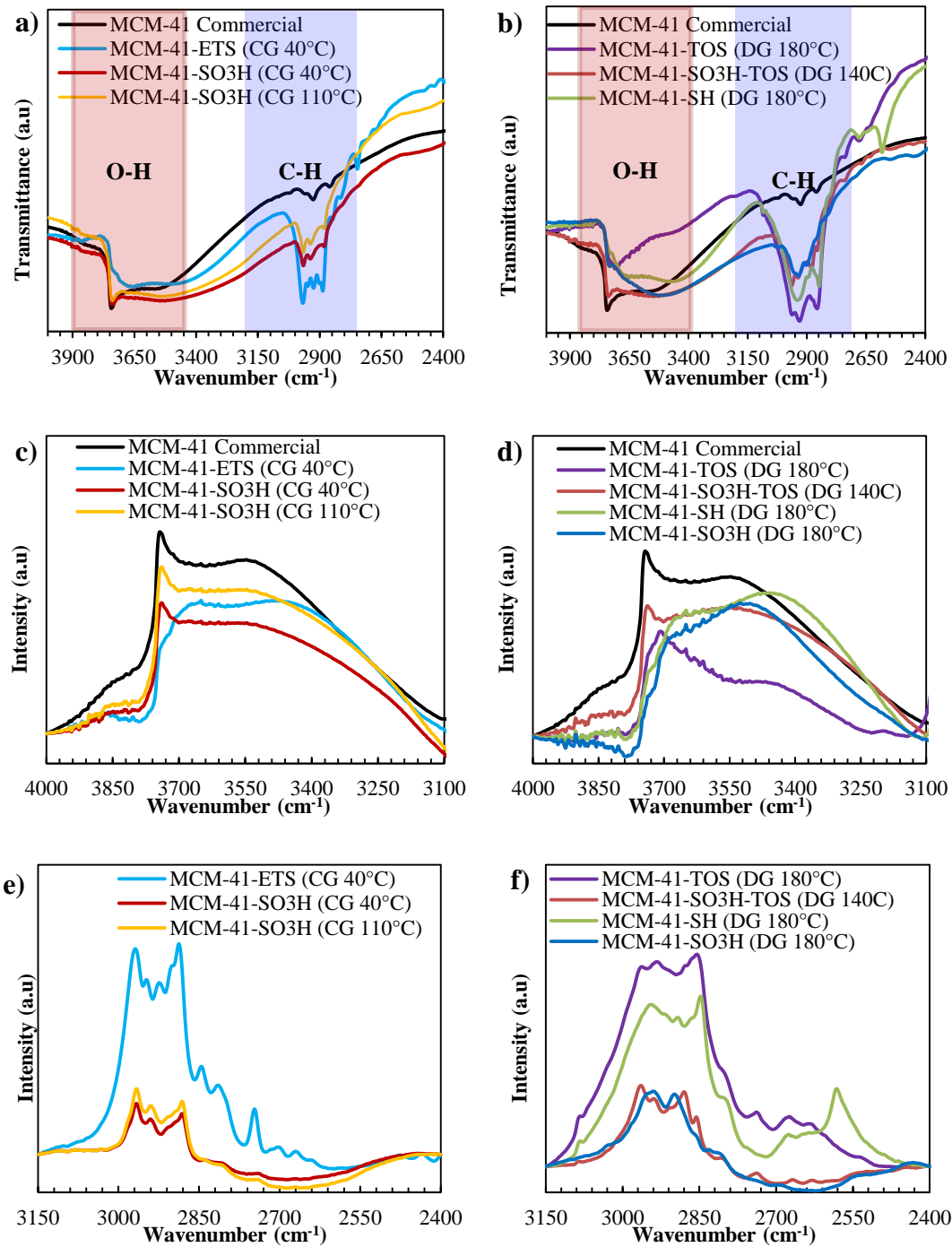
Figure 17. FTIR spectrum at 50°C for the functionalized MCM-41 via CG: conventional grafting and DG: dry grafting the temperatures besides the method indicates the temperature synthesis of each sample; a) FT-IR spectra of the CG catalyst, b) Spectra of the DG catalyst, c) O-H vibration region for CG catalyst, d) O-H vibration region for DG catalyst, e) C-H vibration region for CG catalyst subtracting the MCM-41 pattern, f) C-H vibration region for DG catalyst subtracting the MCM-41 pattern
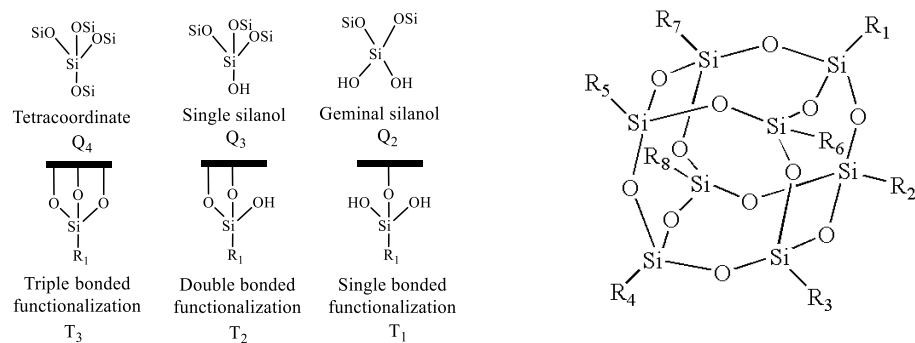
Figure 18 Different grafting modes on MCM-41@MPTS/ETS/TOS[42,45]

As expected, all the samples synthesized by DG presented a decrease in the free silanols density on the surface (**Figure 2b**) together with an increase in the band assigned to the alkyl chain compared to those of parent MCM-41. The band in the region of ~2550 cm^{-1} belongs to the vibration of –SH group (MCM-41-SH-DG), which disappeared after undergoing oxidation by H_2O_2 to form –SO_3H (MCM-41-SO3-DG) group.

1H-29Si CP-NMR analysis reported by Zhao et al. [42] has confirmed the existence of different modes of silica surface including the tetracoordinate Si-$(OSi)_4$ (Q_4 at -111pm), single/hydrogen-bonded Si-$(OSi)_3$-(OH) (Q_3 at -101ppm) and germinal silanol Si-$(OSi)_2$-$(OH)_2$ (Q_2 at -92ppm) siloxanes. On the other hand, the functionalization produces organosilanes structures in the form of T^m=RSi$(OSi)_m$-$(OH)_{3-m}$, m=1–3. Comprising T_1 at (single bonded), T_2 at -57ppm (double bonded) and T_3 at -65ppm (triple bonded) as shown in Figure 18[11,24,46–48].
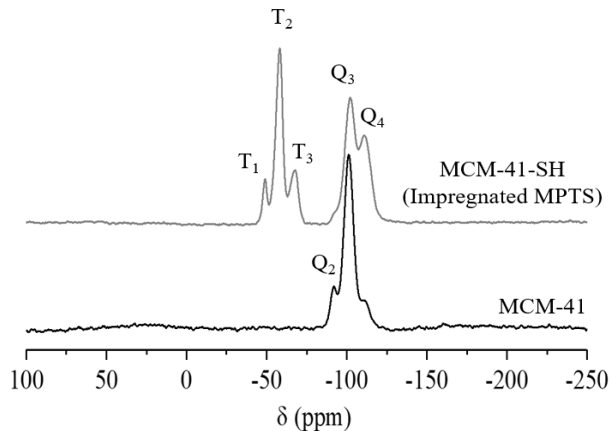
Figure 19 1H-29Si CP-NMR spectra for the pattern MCM-41 and impregnated MCM-41 with MPTS.

The siloxane composition provides information about the bulk as well as free surface structures of the silica material, that are not silylated by functional moieties. It is well known that those organosilane structures would have a characteristic chemical shift because of their particular surrounding chemical environment. That means a chemically surface-bonded organosilane species would have a chemical shift value different from physically adsorbed ones. To prove the idea, the physical impregnation of MPMS on MCM-41 was carried out without any further treatment. Surprisingly, the presence of T_1, T_2, and T_3 structures in that sample are clearly observed, which indicates that the appearance of those peaks is not strong evidence for successful functionalization. The interference caused by the saturated occupation of physisorbed organosilanes on the surface might be a possible explanation for this misleading observation (See *Figure 3*).

In agreement with FT-IR analysis, the 1H-29Si CP-NMR analysis shows a decrease of free surface silanols on MCM-41-ETS (CG) and MCM-41-SO₃H (DG) samples due to the bond formation between the organosilanes and the surface silanols whereas MCM-41-SO₃H (CG), on the other hand, does not.

46
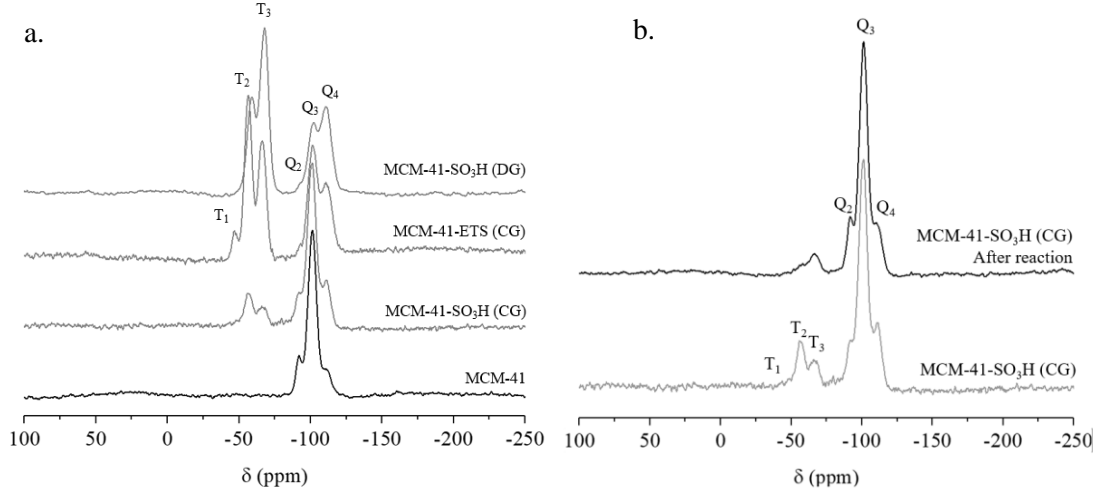
Figure 20 1H-29Si CP-NMR spectra: a. Comparison between the grafting methods evaluated, b. Conventional grafting sample before and after alkylation reaction between cyclopentanol and m-cresol reaction under free-solvent conditions at 250°C, 850 psi, 150 mg of cat and 2h of reaction.

In line with that, the efficiency of grafting process, evaluated by the degree of functionalization (DeF) (Eq. 1), demonstrates high value for MCM-41-SO3H (DG) and MCM-41-ETS (CG) (84.13% and 89.45%, respectively). Only 36.5% of the silanols on the surface of MCM-41-SO3H (CG) sample presented functionalization, and only 20.7% of DeF remained after the leaching test.

$$DeF = \frac{3T_3 + 2T_2 + T_1}{3T_3 + 2T_2 + T_1 + 2Q_2 + Q_3} \quad (1)$$

$$Relative\ intesity = \frac{\sum_{i=1}^{3} T_i}{\sum_{i=1}^{3} T_i + \sum_{i=2}^{4} Q_i} \quad (2)$$

$$Surface\ composition = \frac{Q_i}{\sum_{i=2}^{4} Q_i} \quad or \quad \frac{T_i}{\sum_{i=1}^{3} T_i} \quad (3)$$

The surface composition of siloxane and organosilane structures (Equation 2 and
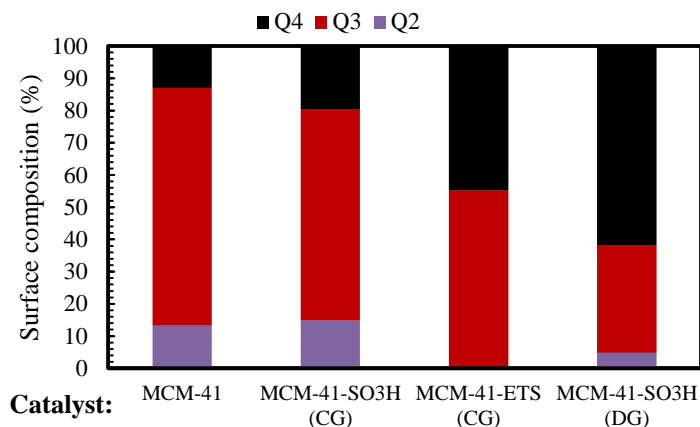
3) are shown in   . First, it

can be seen from Figure 21 that the dominant mode of functionalization on the surface of

MCM-41-SO3-CG is the T2 mode. The relative intensity drops after the leaching test

proved that certain amount of grafted moieties was lost into the solution. Interestingly,

the dominant mode of functionalization switches from T_2 to T_3, the most stable anchored

way. A similar composition is observed in the case of MCM-41-SO$_3$H-DG catalyst which

is the only catalyst obtained that even under harsh chemical environment does not leach.

Two explanations might be possible to the leaching phenomenon, when the surface is

dominated by the most stable T3 mode, it is protected or at least strongly resisted from

the attack of leaching agent (polar solvent) via solubilization or; the successful titration

as well of the decrease in the surface free silanols increase the stability of the material

reducing the hydrolysis of the Si-O-Si bond as was observed by Zhang (2015)[37].

Opposite, MCM-41-PI sample demonstrates a relatively highest T_2 and T_1 composition

compared   to   any   other   samples.   .
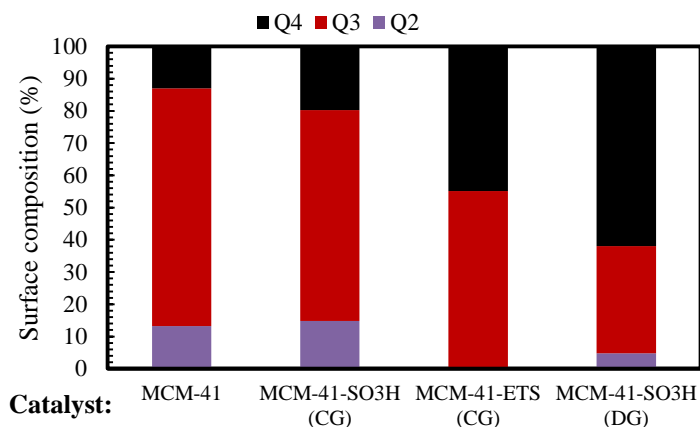
.b) shows comparable distribution of siloxane structures between MCM-41-SO3H-CG (fresh and spent) and parent MCM-41, indicating that the ineffective functionalization does not alter the silica surface. It is supported by the fact that the siloxane structure of MCM-41-ETS-CG and MCM-41-SO3H-DG are remarkably changed after being functionalized.
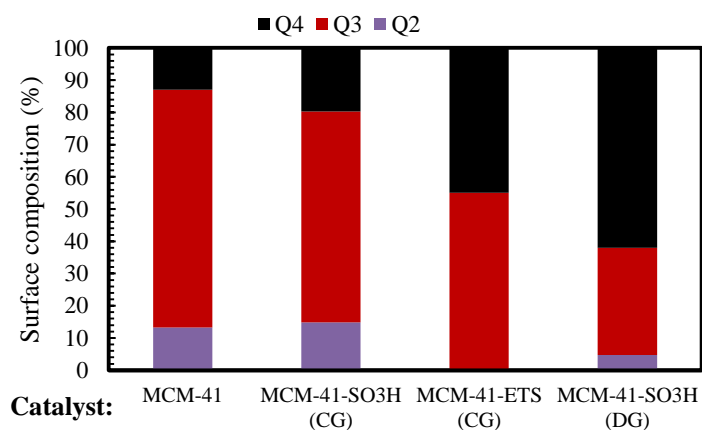
Figure 21 Surface composition of the functionalized MCM-41 through conventional and dry grafting

The presented results are substantial evidence to show that the conventional grafting is not effective when trialkoxy organosilanes are used as a precursor because the possible presence of water. Moreover, the temperature is not high enough to activate the $(R_1\text{-}O)_3$-Si bonds presented in the functionalization. However, the novel proposed method dry

grafting solves the problems related to the leaching in the presence of polar solvents creating a stable material whit promising alternatives to be used in different areas of study.

3.6. Conclusions

The novel proposed method in this study, dry grafting, is an alternative for the functionalization of mesoporous materials through the grafting of the silica surface. It has been proved, the successful creation of a covalent bond between the functionalization and the material which is stable in the presence of polar and nonpolar solvents. The low chemical stability presented by the CC and CG methods make them not suitable to be used in catalytic reactions at high temperature and polar solvent conditions because those conditions may favor the leaching.

3.7.Supplementary Information

3.7.1. Thermo Gravimetical Analysis and functionalization loading calculation

— TGA — H_2O — SO_2 — CO_2
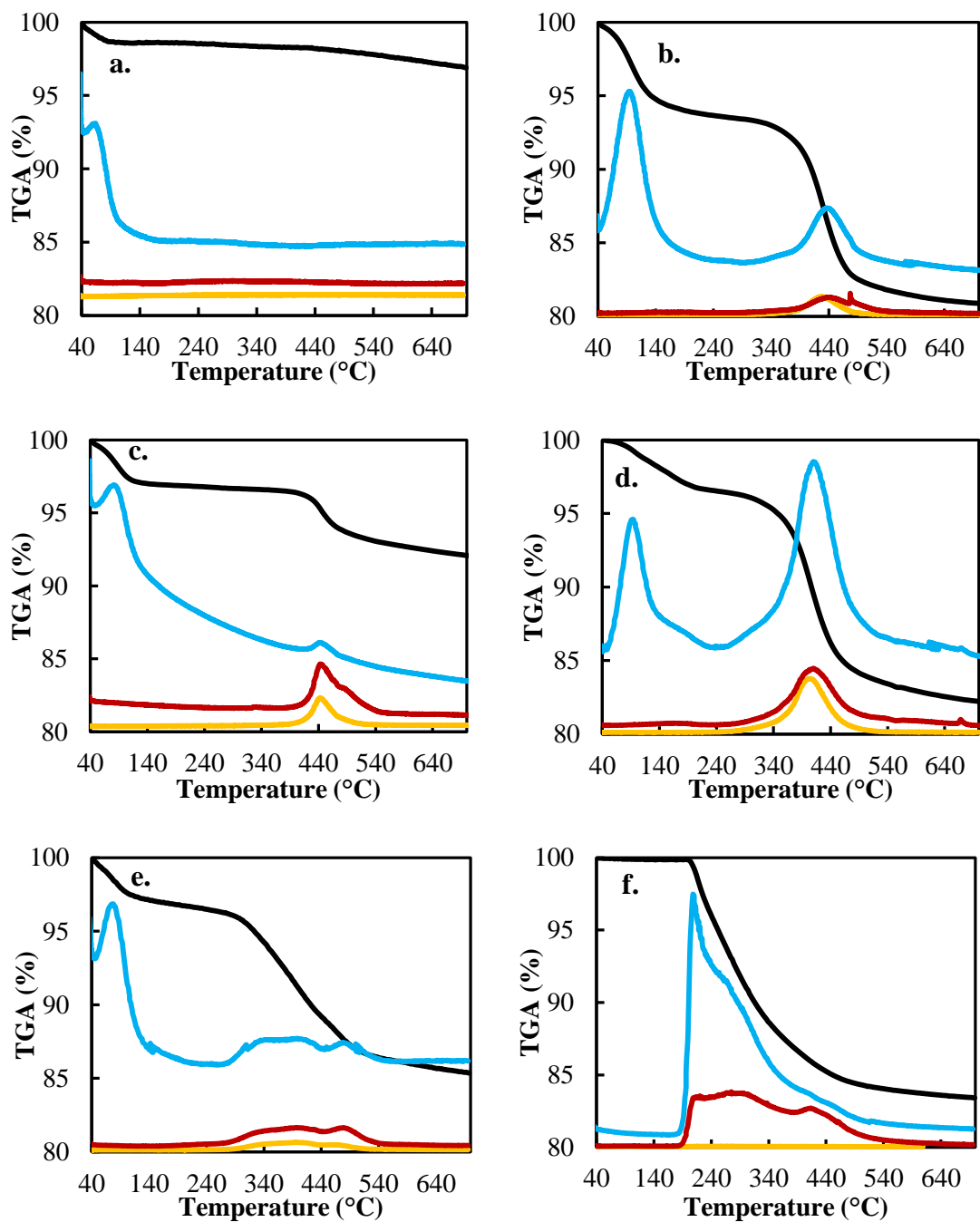
Figure S1 TGA-TPO decomposition analysis for the functionalized silica: a. MCM-41, b. SBA-15-SO₃H (CC), c. MCM-41-SO₃H (CG), d. MCM-41-ETS (CG), e. MCM-41-SO₃H (DG), f. MCM-41-TOS (DG) TGA-TPO patter decomposition of MCM-41-SO₃H obtained from dry grafting.

3.7.2. **N_2 isotherms of adsorption and desorption over the functionalized and unfunctionalized mesostructured.**
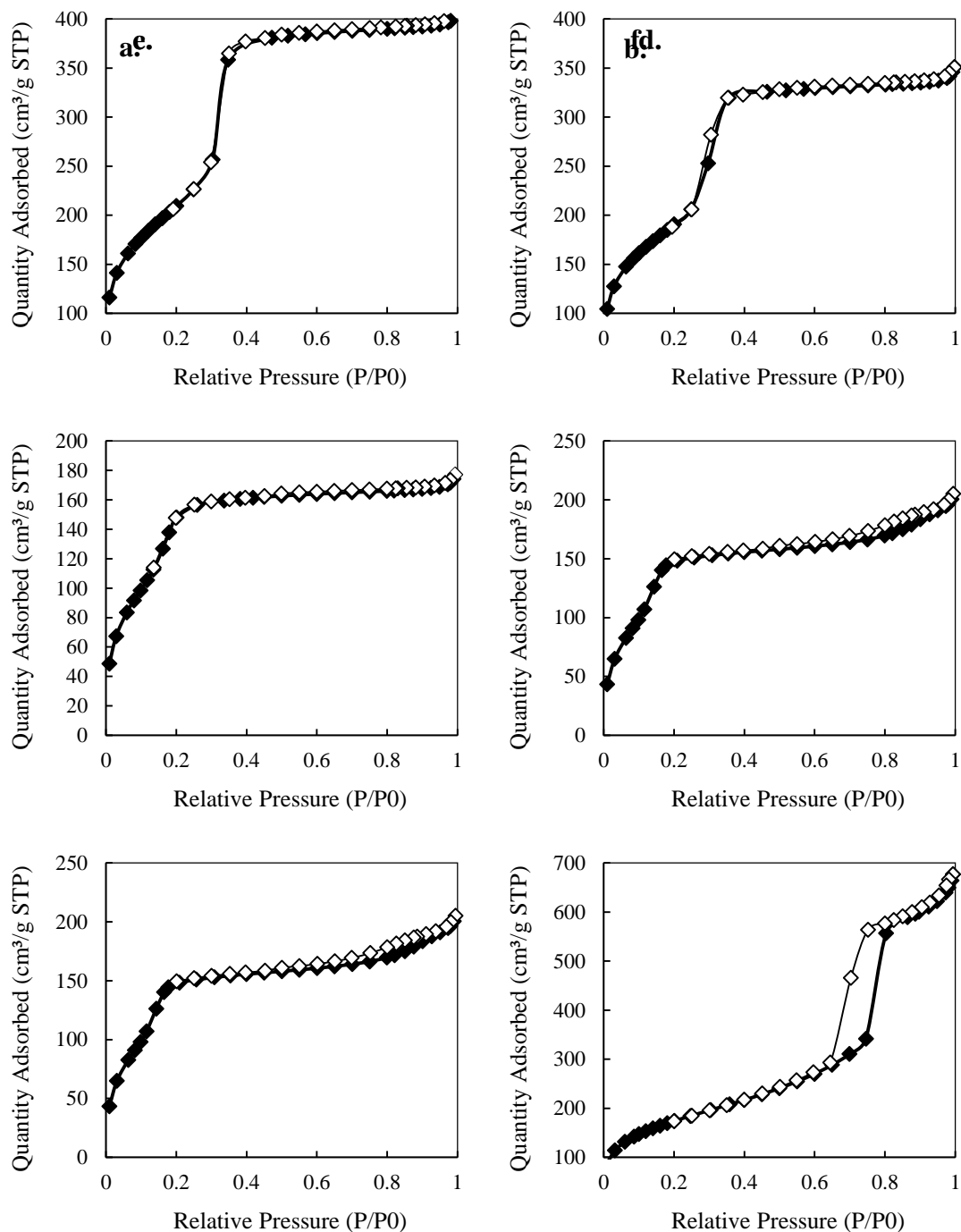
Figure S2 Isotherms of adsorption and desorptions for: a. MCM-41, b. MCM-41-SO₃H (CG), c. MCM-41-ETS (CG), d. MCM-41-SO₃H (DG), e. MCM-41-TOS (DG) f. SBA-15-SO₃H (CC). (♦) Isotherm od adsorption, (◊) Isotherm of desorption.

Table S1 Surfaces properties of functionalized and unfunctionalized mesostructured silica. The surface area and pore diameter were calculated using BET method. The pore volume was obtained with the BJH method

Sample	Surface Area (m^2/g)	Diameter (Å)	Pore Volume (cm^3/g)
MCM-41	728.84	32.28	0.61
MCM-41-SO$_3$H (CG)	690.87	30.42	0.52
MCM-41-ETS (CG)	620.67	16.99	0.26
MCM-41-SO3H (DG)			
MCM-41-TOS (DG)	675.61	17.82	0.3
SBA-15-SO3H (CC)			

The Table S1 and Figure S2 shown the surface properties and N$_2$ isotherms for the functionalized and unfunctionalized silica respectively. It is shown that the surface area decreases as well of the pore diameter of the silica when the grade of functionalization increase. Intrinsically, the functionalization of the silica changes the surface properties because of the adding of moieties in the pore which directly affects the pore diameter. The higher decrease of surface area and pore diameter was observed for the MCM-41-ETS (CG) while the lower decrease was observed for the MCM-41-SO$_3$H (CG) that agrees with the conclusion presented in the current investigation where the conventional grafting results inefficient for trialkoxy organosilanes moieties

All the evaluated samples present hysteresis between the adsorption and desorption isotherms. However, is more noticeable the hysteresis presented by the co-condensed SBA-15. That typically behavior (Type IV Isotherms) shown that the materials employed in this paper are classified as mesoporous materials

3.7.3. Thermo stability of MCM-41-SO$_3$H (DG)
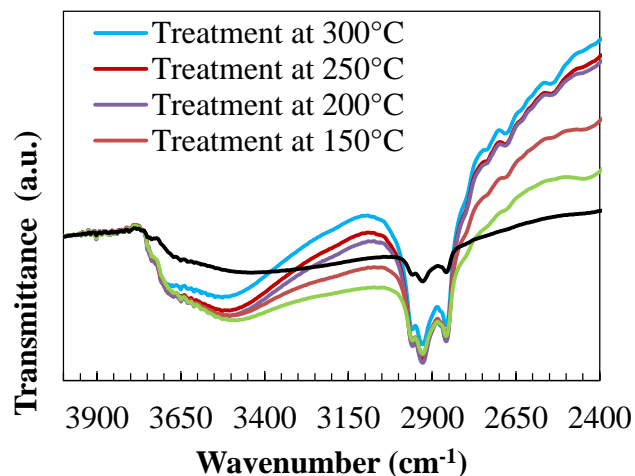
Figure S3 DRIFT spectra at 50C for MCM-41-SO$_3$H (DG 180°C) treated at different temperatures in constant flow of He.

The thermal stability of MCM-41-SO$_3$H (DG) was evaluated in situ in the FTIR cell (High temperature DRIFT HVC cell). The sample heated up in presence of He at 10°C/ min until reach the desire temperature and keep it constant for 1 h. Following of the thermal treatment, the cell was cold down to 50°C and the DRIFT spectra was collected. The results are presented in the Figure S3. It is noticeable the increases of the signal in the region of 3700 to 3100 cm^{-1} (corresponded to the O-H stretching vibration) with the increment of the temperature. This behavior is explained because of the desorption of the physisorbed water on the surface reducing the interference on the IR signal. The C-H vibration region (2800-2600 cm^{-1}) presence a clear band which remain constant whit the increase in the temperature indicating high stability of the Si-C bond under the tested conditions. No loses of functionalization was detected during these experiments, consequently, is concluded that under the tested conditions the functionalization is thermal stable at a temperature of 300°C.

3.7.4. Transmission electron microscopy images of the functionalized silica

      a.   **b.**
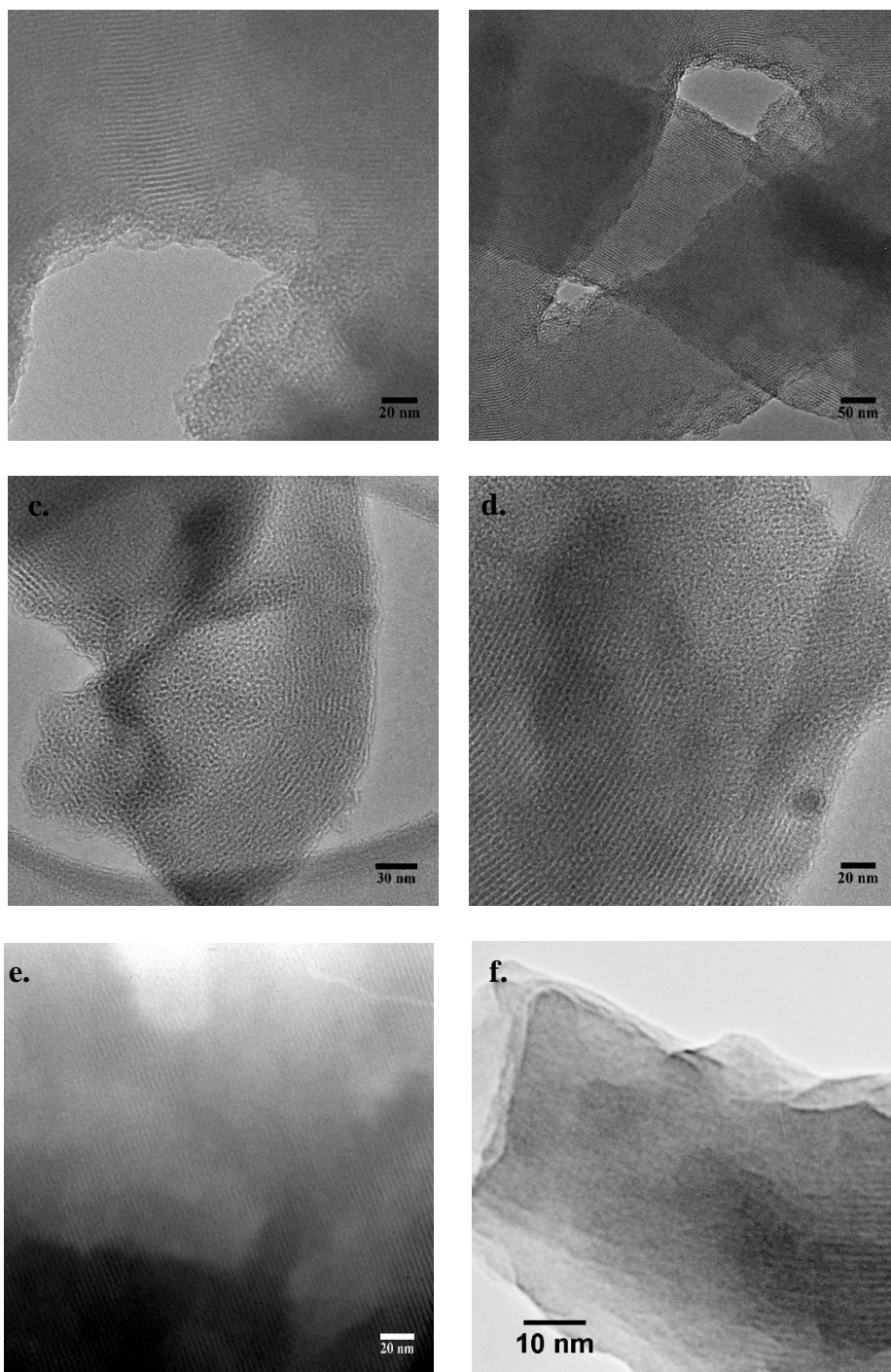
Figure S4 HRTEM for the functionalized and unfunctionalized MCM-41: a-b MCM-41, c-d MCM-41-SO₃H (DG), e. MCM-41-SO₃H (CG) after 4 sequential methanol washes at 200°C for 6h and f. MCM-41-SO₃H (CG)

3.7.5. Dry grafting over SBA-15 with trialkoxyorgano silanes
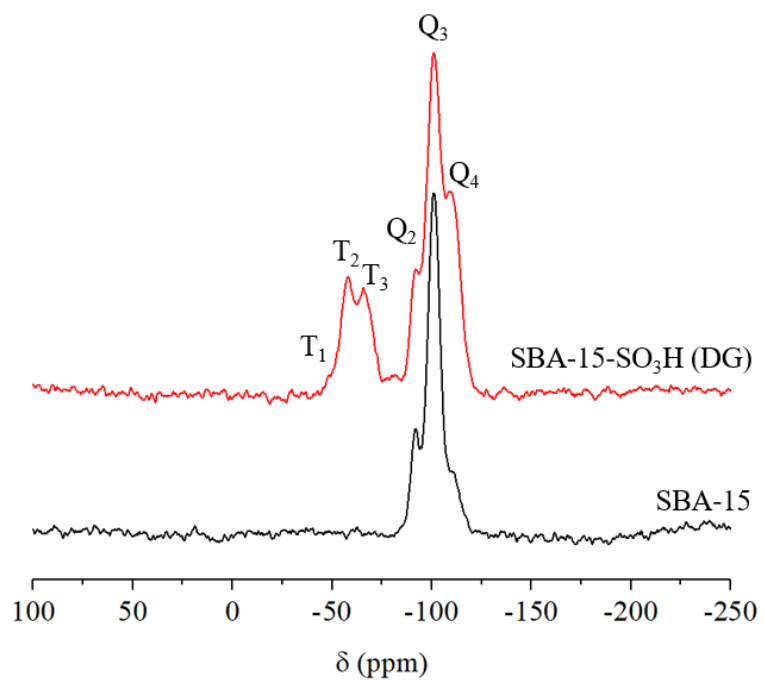
Figure S5 1H-29Si NMR for SBA-15-SO₃H (DG)

CHAPTER 4: Probing the active sites in Zr$_6$ UiO66 metal-organic framework by a synergic combination of catalytic investigation and DFT calculation

4.1. Graphical Abstract
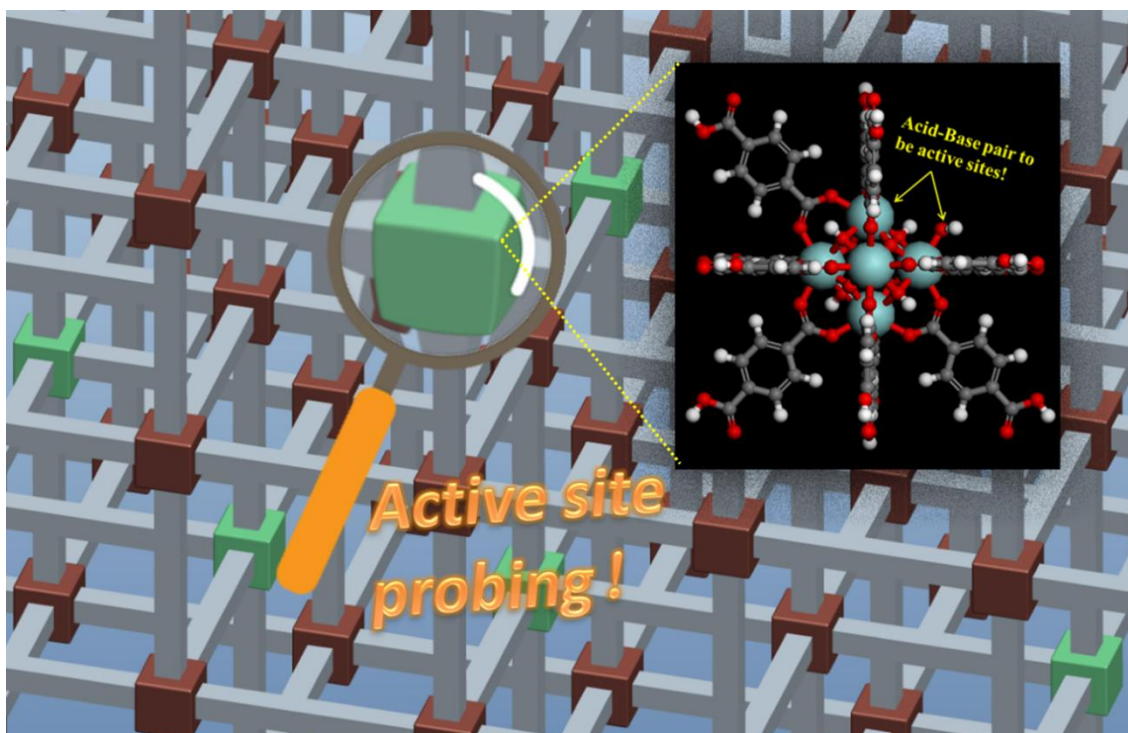
4.2. Abstract

Metal-organic frameworks (MOFs) constructed from Zr$_6$-based nodes have lately received considerable attention in heterogeneous catalytic applications for their excellent chemical reactivity and exceptional thermal and chemical stability. In this paper, Zr$_6$ UiO66 has been successfully applied in the self-condensation of cyclopentanone (CPO), an important platform chemical produced from biomass, to produce longer chain chemicals which can be used as petroleum additives. The Zr$_6$ UiO66 showed high catalytic activity and structure stability in the liquid phase aldol condensation reaction

with the TOF of 0.6 s^{-1}, higher than the most commonly used ZrO$_2$. Different experimental probing and density functional theory calculations were used to elucidate the precise active sites topology of the Zr$_6$-based framework UiO66. Our results conclude that the ortho-unsaturated Zr and the -OH group are the defect site of UiO66 acting as an active "acid-base" pair catalyze the CPO self-condensation reaction.

Key Words MOF, UiO66, biomass, cyclopentanone, aldol condensation, active sites, acid base pair.

4.3. Introduction

Metal-Organic Frameworks (MOFs) are a class of crystalline materials constructed from the linking of inorganic and organic units through coordinative bonding, posing properties with high stability, tunable metrics, organic functionality, and ultrahigh porosity[92–94]. These properties, together with the extraordinary degree of variability for both the organic and inorganic components of their structures, make MOFs widely regarded as promising materials for applications in gas storage, catalysis, separations, drug delivery, sensors and other clean energy applications[95–99]. The structural Nano-porosity of MOF materials places them at the frontier between zeolites and surface metal-organic catalysts. Researchers have high expectations for MOFs in catalysis because of the high concentration of metal ions dispersed in a micro- or mesoporous matrix. However, the activity of current MOFs rarely approaches other microporous solids, e.g., zeolites. One possible reason is fully coordinated framework metal ions makes MOFs lack of accessible active sites. Also, partly because of the lower stability of MOFs in comparison to e.g. zeolites that in some cases the reactants seem to break the metal-linker bonds, results in the MOF structure collapse[100].

Recently, a kind of zirconium (Zr_6 nodes)-based 12-coordinated metal-organic framework (Zr_6 UiO66, UiO: University of Oslo) attracted great attention because of its ultra-high surface area and super thermal stability (stable up to 773K) in air compared to those of other MOFs[101]. Zr_6 UiO66 has the highest coordination number among all the reported MOFs so far. Each zirconium metal cluster center is connected to 12 benzene-1,4-dicarboxylate (BDC) linkers to form the 3D framework. In addition, the combination of the strong Zr-O bonds and the ability of the inner Zr_6 cluster to rearrange reversibly upon dehydroxylation or rehydratation of μ_3-OH groups without detrimental effects on the stabilities of the connecting dicarboxylate bridges lead to a strong resistance towards DMF, ethanol, and other chemicals[102,103]. These attributes make Zr_6 UiO66 framework an outstanding candidate for practical catalysis applications. Moreover, it was proposed recently that although a perfect Zr_6 UiO66 crystal has a 12-connected framework structure, in real samples, the number is always less. H. Wu *et al*. found that about one out of 12 linkers are missing in Zr_6 UiO66[104]. The number of node defect can actually be tuned up by using HCl as modulator, as reported by M. J. Katz *et al*.[105]. The defect sites in Zr_6 UiO66 may thus result in high activity in catalysis applications. Noteworthy, a wide-ranging perspective of Zr_6 UiO66 application in catalysis is opened by the ability to adjust their acid-base or/and redox properties by variation both nature of metals and organic ligands[100,106].

Various catalytic reactions have been conducted using Zr_6 UiO66 as efficient heterogeneous catalyst. However, researchers have different opinions on the nature of the active site in Zr_6 UiO66 for different reactions. In particular, it has been difficult to accurately assign where the active site is and even hardly to comprehensively describe

the nature of the active site. F. Vermoortele et al. [100] reported that Zr_6 UiO66 is highly active in Lewis acid catalyzed cross-aldol condensation of benzaldehyde and heptanal. J. Kim et al. [107] demonstrated that catalytic activities of Zr_6 UiO66 correlate with their Lewis acid-base properties in cycloaddition of CO_2 to styrene oxide. J. T. Hupp et al. [105]demonstrated that the combination of the strong Lewis-acidic Zr^{IV} and bridging hydroxide anions led to the high activity of Zr_6 UiO66 in the biomimetic catalysis of the methanolysis and hydrolysis of methyl paraoxon. On the other hand, S. H. Jhung et al[108] demonstrated that Zr_6 UiO66 has both Lewis acid and Lewis base properties and the catalytic properties of these materials depend on amount and type of functional groups presented in the linker units. They also found that the catalytic activity of metal carboxylates correlated with the amount of basic sites and the strength of the interaction between metal and oxygen in the "M^{+n}-O^{2-} Lewis acid-base" pair in the condensation reaction of benzaldehyde and malononitrile[109]. Meanwhile, V. V. Speybroeck et al.[110] pointed out that Zr-Lewis acid site and an oxo-atom basic site serve as active site in the cross-aldol condensation reaction of heptanal with benzaldehyde. D. Farrusseng et al.[111] demonstrate that (surface) defects are at the origin of the catalytic activities and the vacancy of ligands or linkers systematically generates (surface) terminations which can possibly show Lewis and/or Brønsted acid-basic features. While R. C. Klet et al.[112] pointed out that Brønsted acidity present in the nodes of Zr_6 UiO66 frameworks by using the potentiometric acid-base titration method.

Conversion of biomass-derived cyclic ketones to a monocondensed product through aldol condensation has great potential for the synthesis of a renewable high-density fuel[17,113]. Cyclopentanone (CPO) is an important platform compound from the selective

hydrogenation of furfural, which has been produced on an industrial scale by the hydrolysis-dehydration of the hemicellulose[27]. Thus, CPO self-condensation reaction is a very important reaction in biofuel upgrading and has attracted increasing attention. Modulated Zr_6 UiO66 should be a good candidate for its high specific surface area, efficient defect sites and tailored mesoporous structure[100,114]. In this paper, we apply the Zr_6 UiO66 catalyst in the aldol condensation of CPO. More importantly, we adopt series of experiments along with the density functional theory (DFT) calculations to systematically probe the nature of active sites in Zr_6 UiO66.

4.4. Materials and Experiments

4.4.1. Catalyst preparation

This work was developed as a collaborative project with Xiang Wang, Qiaohua Tan, Duong T. Ngo from: School of Chemical, Biological and Materials Engineering, University of Oklahoma, 100 East Boyd Street, Norman, Oklahoma, 73019, United States. The catalyst synthesis and characterization was developed by Xiang Wang, the density functional theory calculations by Qiaohua Tan and deactivations studies by Duong T. Ngo

The chemicals used in the synthesis process include DMF (dimethylformamide, anhydrous, 99.8%), H_2BDC (terephthalic acid, 98.9%), $ZrCl_4$ ($\geq$99.9%, trace metals basis), FA (formic acid, reagent grade, $\geq$95%) and methanol (anhydrous, 99.8%), which were all obtained from Sigma-Aldrich. The chemicals were used without further purification. Zr_6 UiO66 MOF was synthesized by scaling-up a previous solvothermal procedure (P. Behrens et al.[102]) with some changes in $ZrCl_4$: H2BDC: DMF: FA ratio.

The schematic of the modulated process for preparation of Zr_6 UiO66 MOF is shown as Figure 22. Typically, 166mg of H_2BDC, 37.8 mL formic acid and 233mg of $ZrCl_4$ were put into a caped glass bottle and sonicated for 30 minutes in 300ml of DMF. After the mixture was standing in an electric oven at 120°C K for 24 h, the synthesized white crystalline powder was entirely washed by DMF for 3 times and then soaked in DMF at 80°C for 12h. The obtained samples were then soaked in and washed with methanol in the same way as described for washing with DMF for 3 times in 3 days. After separated by centrifugation, the solid sample was dried under vacuum at 120°C for 24 h in a vacuum oven.
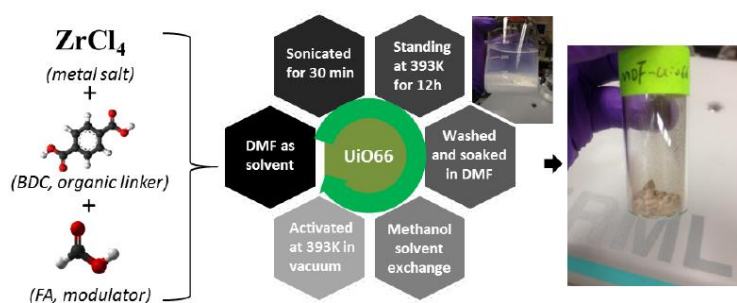
Figure 22 Schematic description of the solvothermal process used for the preparation of d-Zr_6 UiO66

4.4.2. Catalyst characterization

Powder X-ray diffraction (PXRD) patterns were collected on a D8 Series II X-ray diffractometer (Bruker AXS) that uses Cu Kα radiation (λ=1.54059Å) generated at 40 kV and 35 mA. The scans covered the 2θ range from 3 to 70°. Thermogravimetric (TG) analysis of the Zr_6 UiO-66 MOF was conducted with Netzsch STA 449 F3 Jupiter equipment, under a flow of He (50 mL/min). N_2 physisorption was performed on a Micromeritics ASAP 2020 unit in the P/P_0 range of 0.01-0.995. Prior to analysis, the samples were degassed *in situ* at 120°C for 24 h. The micropore volume was derived from

the *t*-plot method (relative pressure range: 0.2−0.6, dose: 7.28 cm^3/g STP, equilibration time: 30s), and the total pore volume was determined at $P/P_0 = 0.995$. The mesopore size distribution was obtained by applying the BJH method to the desorption branch of the isotherm. DRIFT spectra were recorded at a resolution of 4 cm^{-1}, accumulating 64 scans, on a PerkinElmer Spectrum 100 FTIR, equipped with a high temperature DRIFT cell (HVC, Harrick) with CaF_2 windows. The MOF sample (100 mg) was loaded in the cell, heated *in situ* up to 50-300°C under 50 mL/min He, kept at this temperature for 5h, and then cooled down to designed temperature. The DRIFT of pyridine (Py) adsorption was conducted by the same equipment as above using a common method which can be found everywhere. The basicity and acidic of the Zr_6 UiO66 were measured by temperature-programmed desorption of carbon dioxide (CO_2-TPD) and ammonia (NH_3-TPD) method, respectively. In each measurement, 50 mg of the MOF sample was used and pretreated for 2h in He flow (30 mL/min) at 150°C to remove any adsorbed impurities. The sample was subsequently exposed it to consecutive pulses of CO_2/NH_3 (10% in He) until saturation and then purged with He flow at room temperature for 1.5h. Then, a 5K/min linear heating ramp was applied up to 500°C and the desorbed products were monitored and quantified on a Micromeritics automatic temperature programmed chemical adsorption instrument (AutoChem II 2920). The morphology and chemical composition of the Zr_6 UiO66 was analyzed using a field emission scanning electron microscope (FESEM, Hitachi S4800) equipped with energy-dispersive X-ray analysis (EDX, Oxford Instrument, UK). High-Resolution Transmission Electron Microscopy (HRTEM, Tecnai G2 F30, FEI, USA) was used to obtain the microstructure of the samples.

4.4.3. Reaction conditions

The reagents used in this study were CPO (CPO, Aldrich, >99%), 2-propanol anhydrous (IPA, Sigma-Aldrich, >99.5%), toluene anhydrous (Sigma-Aldrich, 99.8%), cyclopentene (CPEN, Aldrich, 96%), cyclopentanol (CPOL, Aldrich, 99%) and acetone (Sigma-Aldrich, >99.5%). Cyclohexane (anhydrous, 99.5%) and decahydronapthalene anhydous (Sigma-Aldich, >99%, mixture of cis + trans) were used as solvent in the CPO self-condensation and probing reactions of aldol condensation, dehydration and alkylation reactions, respectively. CPO was further treated by distillation process at 110°C under a N_2 (Airgas, Ultra high purity) environment, achieved by bubbling N_2 into the solution, in order to separate oligomers from the reagent. The purity of the CPO was verified using a GC-FID.

The CPO self-condensation reactions were carried out in a batch reactor (Parr Instruments, USA Mod. 4564). For each reaction, 50 mg of Zr_6 UiO66 and 40.265 ml of cyclohexane were added into a 100 ml reactor vessel, repeatedly purged with N_2 at room temperature for 3 times and then pressurized up to 300 psig. Afterwards, the agitation was initiated with a stirring speed of 450 rpm and heated up to 150 °C. Then, 8 ml of CPO and 2 ml of toluene (internal stand) were pressurized to 450 psig in a 30 ml cylinder and entered into the system when temperature was satisfied. Finally, a steady pressure and temperature were maintained throughout the scheduled reaction period. After reaction, the reactor was quenched to room temperature by ice water. The catalyst was separated by vacuum filtration before being analyzed by PXRD, BET and DRIFT.

A series of probing reactions have been carried out to further understand the acidity and basicity of the active site of the Zr_6 UiO66. The probing reactions were carried out in

a Mini Bench Top Parr high pressure reactor of 160 mL (Model Parr 4564) equipped with a Parr 4848 Reactor Controller for temperature and stirring. In a typical experiment, 50, 100, or 200 mg of catalyst were mixed with the initial solvent (80 mL) and pressurized to 300 psi with N_2 followed by increasing the temperature to 250°C. In a separated vessel the reactants were blended in the desired concentrations and the solvent was added to achieve a volume of 20 mL and bring the total volume in the reaction to 100 mL. The reactants solution was placed in a separate vessel and injected into the reactor reaching a final pressure of 850 psi.

Pyridine anhydrous (Sigma-Aldrich 99.8%) and propionic acid (Sigma-Aldrich, >99.5%) were used as titrant molecules to understand the role of the active sites during the catalytic aldol condensation. In these experiments, the reactions were carried out as above with the incorporation of the titrant compound in the mixture of reagents. The catalyst amount used was 50 mg and 150°C in order to decrease the reversibility in the adsorption.

The conversion of the limiting reagent was calculated as follows:

$$Conversion\ (\%) = \frac{\sum_{i=0}^{n} \Upsilon_i \eta_{P,i}}{\eta_{R0}} * 100 \quad (1)$$

Where Υ_i is the reaction coefficient and η_i is the moles of the products i of the reaction. Another important parameter calculated was the carbon balance described by the equation (2). With Υ_j representing the reaction coefficient of the reactant and products j and η_j the moles of the reactive and the products after the reaction. The subscript $R0$ indicates the initial moles of the reactant.

$$Carbon\ Balance\ (\%) = \frac{\sum_{j=0}^{n} \Upsilon_j \eta_j}{\eta_{R0}} * 100 \quad (2)$$

The resulting product of the reaction was filtered using a PTFE filter of 0.22 µm and analyzed for product identification with GC-FID equipped with a Phenomenex capillary column (ZB-1701, 15 m x 0.25 mm x 0.25 µm) for polar compounds analysis and a Phenomenex capillary column (ZB-5MS, 30 m x 0.25 mm x 0.25 µm) for non-polar compounds. To identify the products a GC-MS equipped with Phenoomenex capillary column (ZB-1701, 15 m x 0.25 mm x 0.25 µm) was used.

4.4.4. Density Functional Theory Calculations

The calculations were carried out using periodic plane-wave gradient-corrected density functional theory methods implemented in the Vienna ab initio Simulation Package (VASP)[115,116]. The PBE functional was used to calculate the exchange correlation energy within the generalized gradient approximation (GGA)[117]. The projector augmented wave method (PAW) was employed to describe the electron-ion interactions[118]. The cutoff energy of 400 eV was applied for the plane-wave basis set to represent valence electrons. The electronic energies were converged within 10^{-6} eV limit.
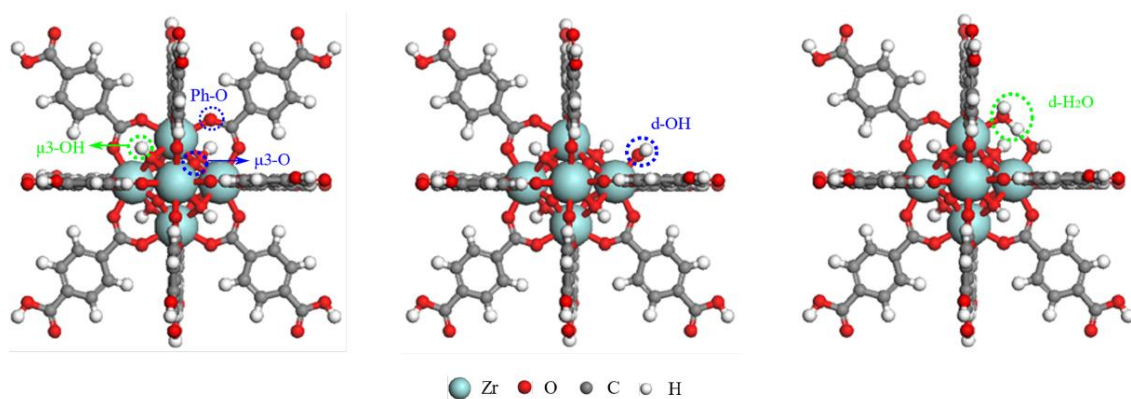
Figure 23 Models for Zr$_6$ UiO66 with (a) perfect structure; (b) with a defect; and (c) with water adsorbed on the defect

The structure with one Zr$_6$ node and twelve H-terminated BPC linkages as shown in Figure 23.*a* was used to model the Zr$_6$ UiO66 with no defect. The defected Zr$_6$ UiO66 (*d*-

Zr₆ UiO66) was modeled by replacing one BPC linkage with OH as shown in Figure 23*b*

The unit cell is 30Å × 30Å × 30Å. The geometric structures were optimized until the

forces were converged to below 0.01 eV/ Å. The 1×1×1 Γ only k-point mesh was used to

sample the first Brillouin zone[119].

The periodic monoclinic ZrO_2 (111) slab surface with 15 Å in the z-direction was used

to model the ZrO_2 catalyst. Each unit cell consisted of four Zr_4O_8 layers along the z

direction and contained 64 Zr and 128 O atoms. The bottom layer atoms were fixed ai

their buld posiions while the others were allowed to relax in all optimizations. The 4×4×1

Monkhorst-pack k-point mesh was used to sample the first Brillouin zone[119].

For a Brønsted acid, the deprotonation energy (DPE) is used to describe its acidity,

which was calculated via Equation (1), where $E(AH)$, $E(A^-)$ and $E(H^+)$ are total energy of

the Brønsted acid *AH*, its conjugated base A⁻ and the proton H^+. For a Brønsted base, the

proton affinity (PE) is used to describe its basicity, which was calculated via Equation

(2), where *E(B)* and *E(BH⁺)* represent the total energy of the base B and its conjugated

acid BH^+.

$$AH \rightarrow A^- + H^+$$

$$DPE\ (AH) = E(A^-) + E(H^+) - E(AH) \qquad (1)$$

$$B + H^+ \rightarrow BH^+$$
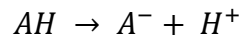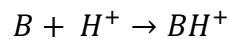
$$PA\ (B) = E(BH^+) - E(B) - E(H^+) \qquad (2)$$

For reaction paths, the transition state searches were performed using the dimer

method[120] with the initial guesses for the transition state structure and the reaction

trajectory obtained through the nudged elastic band (NEB) method[121].

67

4.5. Results and discussion

4.5.1. Physicochemical properties of Zr$_6$ UiO66

The PXRD pattern of the synthesized Zr$_6$ UiO66 MOF is shown in Figure 24. The results indicate that the PXRD pattern of the synthesized MOF agree quite well with simulated PXRD pattern of pristine UiO66 frameworks, indicating that the prepared sample has an isostructural UiO66 framework topology[101]. In addition, the result shows good crystallinity of the Zr$_6$ UiO66 samples for the two high intensity peaks at 7.4° and 8.5° which representing the (111) and (002) crystal plane. The SEM and HRTEM images (Figure 27) also shows that Zr$_6$ UiO66 has uniformly distributed and well-crystallized individual and octahedral crystalline morphologies with the particle size of around 300 nm.
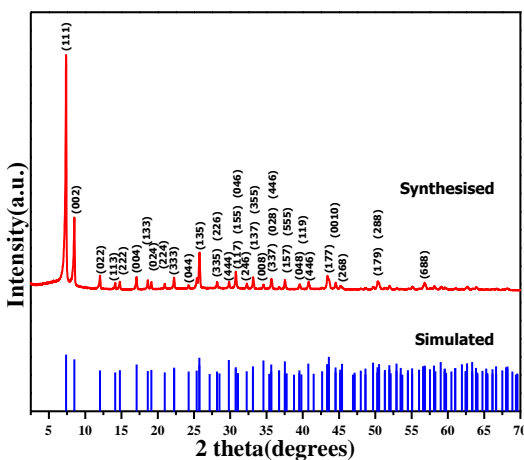
Figure 24 PXRD patterns of simulated and synthesized Zr$_6$ UiO66

Weight loss profiles from TG analysis showed that the as-prepared Zr$_6$ UiO66 samples present mainly two stages in weight loss, as shown in Figure 25. A nearly continuous mass loss up to 450°C was observed in the TG plots. The endothermic DSC results suggest this mass loss probably corresponds to the removal of water and all organic

material, including the evaporation of guest molecules from the pores such as solvent DMF, modulator formic acid and methanol[122].
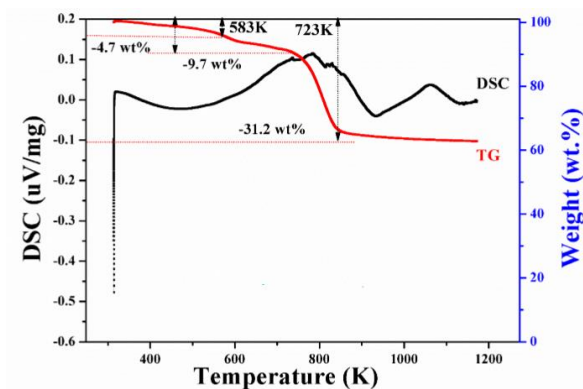
Figure 25 Thermal analysis (TG and DSC) profiles for d-Zr6 UiO66.

Between 310 and 450°C, the weight loss was very slow indicating the loss of a small fraction of none effective coordinated H_2BDC linkers. The samples maintained their structure up to 450°C and after that a sudden weight loss and an obvious exothermic peak were observed, which was attributed to decomposition of the Zr_6 UiO66 to ZrO_2. This suggests that the highly thermal stable Zr_6 UiO66 has been successfully obtained from this modulated synthesis procedure.
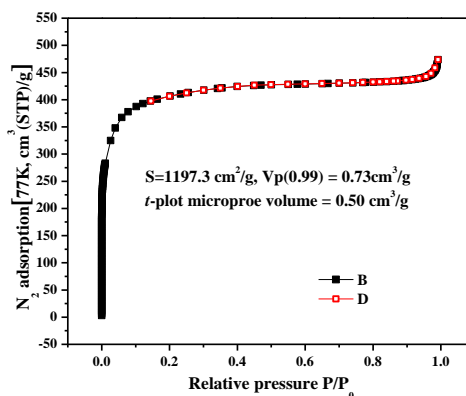
Figure 26 N_2 adsorption (filled squares) and desorption (open squares) isotherms of Zr_6 UiO66

The porous structure of Zr_6 UiO66 was measured by N_2 adsorption, shown in Figure 26. The adsorption of N_2 follows a type I isotherm with no hysteresis and possesses with a BET surface area of 1197.3 m^2/g. The total pore volume at $p/p_0 = 0.995$ and the micropore volume obtained from the t-plot method of Zr_6 UiO66 are 0.73 and 0.50 $cm^3 \cdot g^{-1}$, respectively. The mesopore volume portion is around 30% and the average pore size is 2.5 nm.
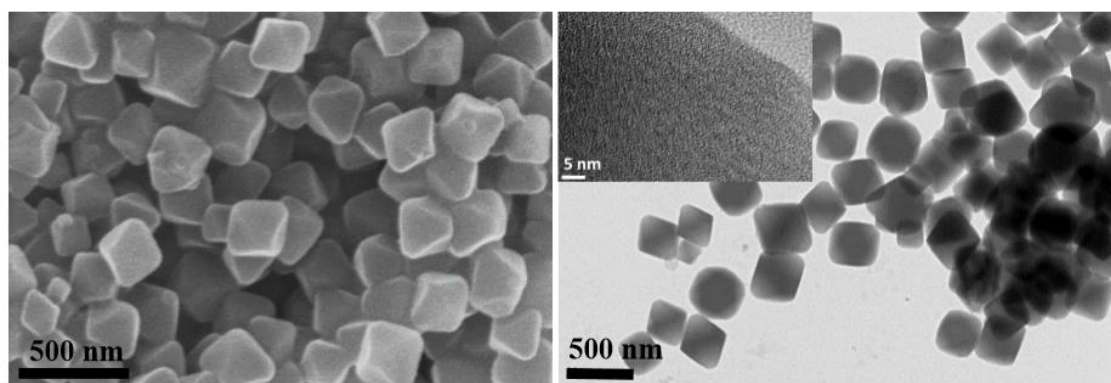
Figure 27 SEM and HRTEM images of d-Zr$_6$ UiO66

The DRIFT spectra of the prepared Zr_6 UiO66 in OH region from 3500-4000 cm^{-1} pretreated at different temperatures *in situ* are shown in **Figure 28**, which is similar to the literature[101,123,124]. The sharp band at 3674 cm^{-1} derives from a combination of the terminal OH groups with the majority of v(O–H) stretching of μ_3-OH. The signal at 3903 cm^{-1} is assigned to the μ_3-OH stretching mode. Furthermore, a band was observed at 3780 cm^{-1}, which have been assigned to the non-hydrogen bonded OH groups at the defect sites[125], which is formed by the reaction of water with the BPC linkage. This suggests the defects exist in our prepared Zr_6 UiO66. When changing the pretreatment temperature from 50 to 300 ℃, the signal at the 3780 cm^{-1} gradually disappear, suggesting that the gradual removal of the OH groups at the defect sites.
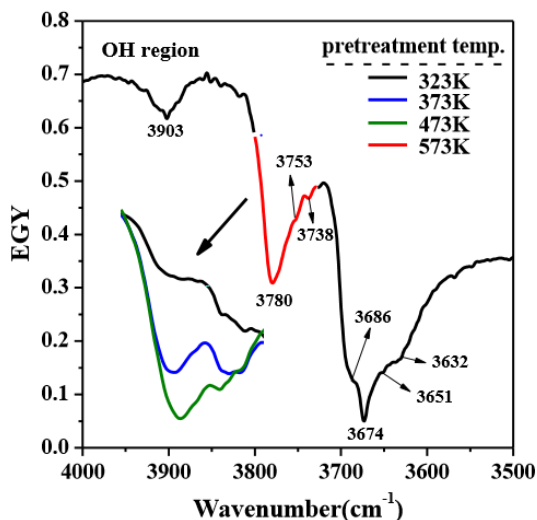
Figure 28 DRIFT spectra of d-Zr$_6$ UiO66 in the OH region (3500-4000 cm^{-1}) pretreated in situ at different temperatures

The CO$_2$-TPD and NH$_3$-TPD profiles of Z$_6$ UiO66 were shown in *Figure 6*. The result indicates that the adsorption amount of CO$_2$ degassed at the temperature of 525K, which corresponds to the medium to strong (450-773 K) basicity groups[126]. According to Topsøe *et al*.'s [107,127] results, the acidity measured by NH$_3$-TPD can be classified into three groups: weak (323–373 K), medium (423–473 K), and strong (593–773 K). In this work, we found two kinds of acid sites which correspond to weak (372K) and medium (528K) acidity.

Wang *et al*. recently showed that the *in situ* titration of some probe molecule such as propanoic acid during the aldol condensation reaction can accurately measure the number of Zr-O site pairs on ZrO$_2$(m) through the uptake of propanoic acid required to suppress the reactant conversion rate. Here, we also applied this strategy in Z$_6$ UiO66. As shown in Figure 29, the reaction rate of the aldol condensation of CPO decreases linearly with the amount of the propanoic acid added, and the number of the acid-base pair in Z$_6$ UiO66 is calculated to be 2.54 *mmol/g*.
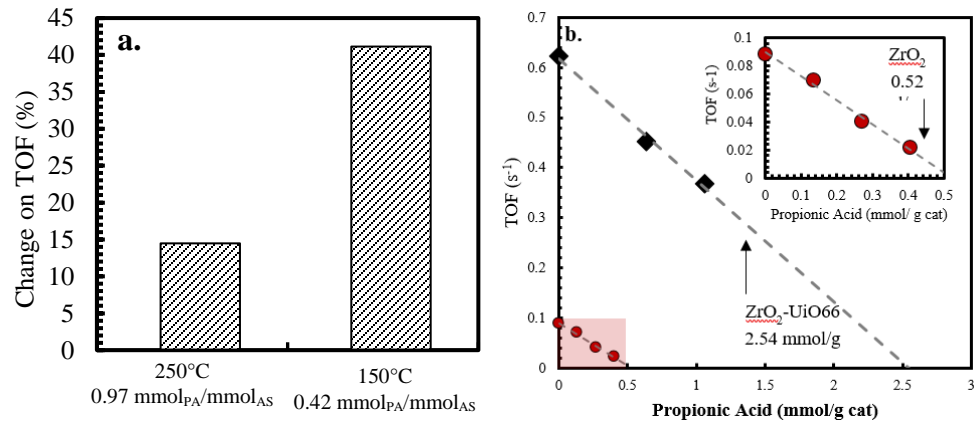
Figure 29 (a) Turn over frequencies change during the in-situ titration of propionic acid at 250°C and 150°C with different amount of PA over active sites in the catalyst, the change of TOF was evaluated as the absolute change $(TOF_0-TOF_{PA})/TOF_0$ (b) Initial turn over frequencies for the aldol condensation reaction of CPO at 150°C and 850 psi of N_2 during the catalytic titration of Zr_6-UiO66 and ZrO_2 with propionic the insertion is the zoom in of the ZrO_2 titration.

4.5.2. High activity self-condensation of CPO in the presence of Zr_6 UiO66

The aldol condensation of CPO over Zr_6 UiO66 and the product distribution were analized in *Table 2*. The main product is the dimer 2-cyclopentylidene-cyclopentanone (D) with the selectivity of 94.3% and the trimer (2, 5-dicyclopentylidene cyclopentanone) (T1) with the selectivity of 3.4% at the conversion of 59.2%. Another trimer product 2,3,4,5,6,7,8-octahydro-1-H-cyclopenta[e]-as-indacene (T2) (Figure 30) was detected but with very small amount (<0.1%). Based on the number of the active sites measured by the in situ propionic acid titration and the conversion, the TOF of the self-condensation of CPO over Zr_6 UiO66 can be calculated, which is 0.19 s^{-1} (*Table 2*). The same reaction was conducted over ZrO_2 as shown in Table 1. The product distribution is similar over ZrO_2, however the TOF is lower (0.08 s^{-1}).
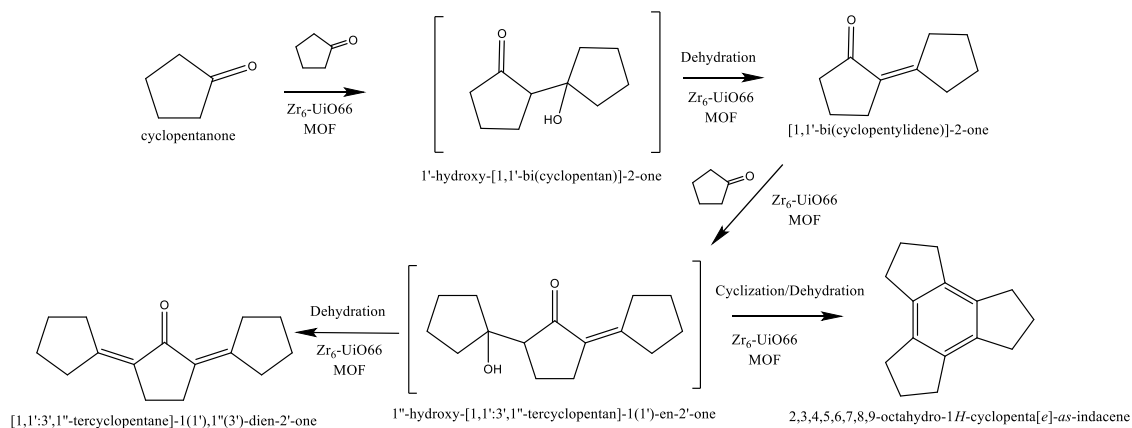
Figure 30 Pathway of reaction for the self-aldol condensation of cyclopentanone, the compounds on the brackets have concentration below of the detection limit.

The conversion of CPO and the yields of products along with time was shown in Figure 31, which suggested that although the Zr_6 UiO66 catalyst showed high activity in the aldol condensation reaction of CPO, it lost its activity in 2 hours.

Table 3 Conversion and product distribution for the aldol condensation of CPO over d-Zr_6 UiO66 and ZrO_2 catalysts.*

	Conversion (%)	Selectivity (D) (%)	Selectivity (T1) (%)	Mass balance (%)	TOF (s^{-1})
Pristine d-Zr_6 UiO66	43.8	94.7	5.7%	90.7	0.19
Partially dehydrated	20.5	97.5	2.5%	100	0.04
ETS functionalized	6.8	99.3	0.7%	101.3	0.02
Feed with H_2O	34.2	97.7	2.3%	95.3	0.08
ZrO_2	45.2	98.3	1.7%	87.0	0.09

*Reaction conditions: 50mg catalyst, reaction at 423K, 450 rpm and 450 psig pressure for 60 mins, feeding CPO 8 ml + toluene 2 ml in solvent cyclohexane 40.3 ml.

4.5.3. Deactivation Analysis of Zr_6 UiO66

Several characterization methods, such as N_2-adsorption, PXRD and DRIFT, have been employed to analyze how the deactivation happens in the aldol condensation of CPO. The N_2 adsorption isotherms of Zr_6 UiO66 before and after the CPO self-condensation reaction was compared as shown Figure 32.*a*, which showed that the uptake of N_2, especially in low relative pressure range (p/p_0), drops a lot in the deactivated Zr_6

73

UiO66 compared with that of the pristine one, thus resulting in dramatically BET surface area drop and micropore volume lost (*vide infra*). Figure 32.*b* shows the pore size distribution and pore volume information (insert table) of Zr_6 UiO66 before and after deactivation.
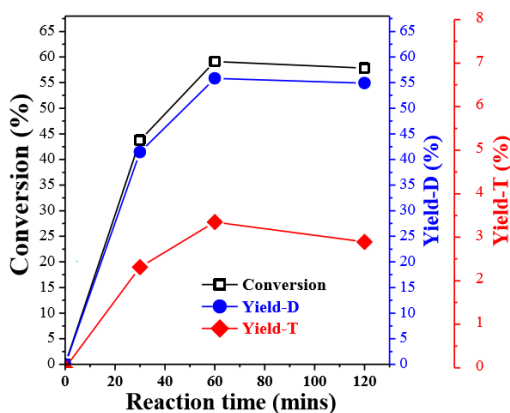
Figure 31 Conversion of CPO and yield of products along reaction time over d-Zr$_6$ UiO66

The results revealed that both the micro-and mesopore volume of the Zr_6 UiO66 significantly decreased after reaction. However, no obvious macropore developed in the deactivated catalyst, which indicates its good pore structure stability. Figure 32.*c* shows the PXRD patterns of Zr_6 UiO66 before and after reaction. The results illustrated that the structural integrity of the catalyst partially decreased after the CPO self-condensation reaction, while the Zr_6 UiO66 still possesses good diffraction intensity and representative crystal faces information. From the HRTEM image of the deactivated Zr_6 UiO66 shown in Figure 32.b insert which shows no evidence of the microstructure change after reaction, we can conclude that the Zr_6 UiO66 maintains most of its pore structure and crystalline intensity after deactivation. Thus we consider that the deactivation of the Zr_6 UiO66 catalyst is not because of the structure collapse, but would probably the blocking of the

74

active sites by organic molecules (e.g. reactants, solvent), polymerized products or the water molecules come from the condensation reaction.
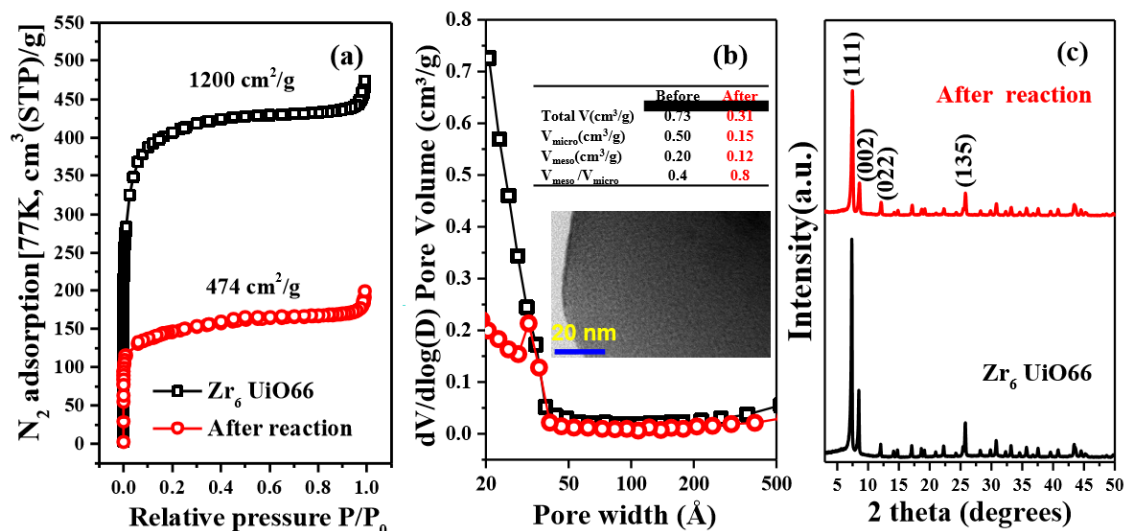
Figure 32 (a) N2 adsorption isotherms; (b) pore size distribution and (c) PXRD patterns of d-Zr6 UiO66 MOF before and after the CPO condensation reaction.

DRIFT spectrometer of the deactivated catalyst was analyzed andshown in Figure 33.*a*. No obvious change was found in the deactivated catalyst comparing with pristine Zr_6 UiO66, except the disappearance of the band in the OH region (3870 and 3686 cm^{-1}) which is attributed to the non-hydrogen bonded OH groups at the defect site, indicating that the active sites in Z_6 UiO66 should be related to the OH groups at the defect. To confirm this hypothesis, the number of the OH groups at the defect sites are tuned in the Zr_6 UiO66 by partially dehydration through vacuum treatment at 280 °C for 48h[122]. The disappearance of the signal at 3780 and 3668 cm^{-1} in the DRIFT spectrum of the partially dehydrated Z_6 UiO66 revealed that a large proportion of the OH groups at the defect sites have been removed, as shown in Figure 33.b. The activity of the partially dehydrated Zr_6 UiO66 was tested and compared with pristine Zr_6 UiO66 at the same reaction conditions. As shown in Table 1, the activity of the partially dehydrated Zr_6 UiO66 dramatically

decreased by 60%, due to the decrease of the number of OH groups at the defected Zr_6 UiO66.
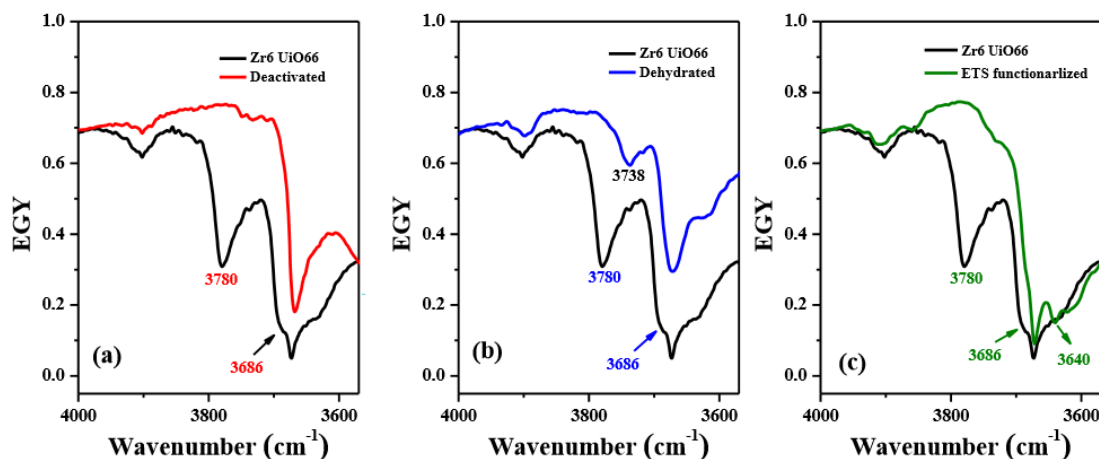
Figure 33 DRIFT spectra of (a) spent, (b) dehydrated, and (c) ETS-functionalized samples, compared to pristine d-Zr6 UiO66

Further, we tried to continue removing more OH groups by a silylation method which has been widely used to functionalize zeolites[128]. Briefly, 0.2 g of pristine Zr_6 UiO66 was dispersed in 10 mL of toluene by sonication with a Horn sonicator (Fisher Scientific, 600 W, 20 kHz) at 25% amplitude for 30min. Then, the Zr_6 UiO66 suspension was added to a 50 mL solution of ethyltrichlorosilane (ETS, 99%) in toluene to get a ratio of 0.15 mmol ETS/g Zr_6 UiO66. The final suspension was stirred for 4 h at 350 rpm at room temperature. The MOF sample was collected by centrifugation and washed thoroughly with methanol. Finally, the functionalized Zr_6 UiO66 was dried in a vacuum oven at 120 °C for 24h. From the DRIFT spectrum of ETS functionalized Zr_6 UiO66 shown in Figure 33.*c,* we can found that the band at 3780 and 3686 cm^{-1} totally disappeared after functionalization compared with pristine sample, indicating the further removal of OH groups. However, the intensities of the 3674 and 3640 cm^{-1} bands characterizing μ_3-OH groups remained essentially unchanged during the chemisorption,

76

showing that, as the ETS reacted with the hydroxyl groups connected to Zr atoms at the defect sites, it did not react with bridging μ_3-OH groups. Similarly, the ETS functionalized catalyst were used in the aldol condensation of CPO, and it was found that about 90 % activity has been lost, further confirming the active site is related to the OH groups at the defect site rather than the μ_3-OH.

Then, we investigated the possibility of water molecules formed in the condensation reaction resulting in the catalyst deactivation.1.8g of water, 4 times more compared with the theoretical yield of water molecules in the initial condensation reaction, was added to the mixture of solvent and catalyst before the catalytic reaction. The results showed that the activity of the Zr_6 UiO66 decreases about 50% because of the water addition, suggesting the deactivation of Zr_6 UiO66 in the CPO condensation may be partly because of the water that is formed in the reaction.

4.5.4. Comparative study of the acid base properties of the active site in Zr_6 UiO66

To further investigate the nature of the active sites, a series of probing reactions were employed to comparative study the acid base properties of Zr_6 UiO66. Table 4 summarize the probing reactions used to find evidence for the catalytic active site in the Zr_6 UiO66. The Meerwein-Ponndorf-Verley (MPV) reaction has been widely studied and it has been proven the reaction happens over a Lewis acid site (LAS)[129]. The MPV reaction was tested between CPO and IPA and no products (Acetone and CPOL) were identified. The alkylation reaction, which has been proven to require Brønsted acidity[130,131], was used as a probe reaction to study the Brønsted acidity of the active sites (BAS). As was expected, the Zr_6 UiO66 does not show any activity for the alkylation between toluene and CPEN. The presented results are in agreement with the results shown

above where negligible effect was detected by the pyridine adsorption over the catalyst TOF, despite no-selective adsorption of pyridine over the Lewis and Brønsted acid sites.

An interesting result was found when the dehydration reaction was evaluated. The Zr_6 UiO66 does not have activity for the dehydration of secondary alcohols such as cyclopentanol or isopropanol in which the dehydration of the alcohol was expected because of the basic oxygen linked to the Zr atoms in the material, however, the dehydration of tertiary alcohols is possible and is noticeable in the pathway presented in the Figure 30, where the dehydration is an intermediary step in the aldol condensation reaction. The expected behavior of MOFs acting as a ZrO_2 was tested. It was found that the dehydration of CPOL and IPA can take place over ZrO_2 and is attributed to the active acid-base pair on the surface.

The aldol condensation reaction has been shown to take place over BAS or acid-base sites[132]. Zr_6 UiO66 has high activity for this reaction assigned to the acid-base pair found in the Zr_6 UiO66 as is shown by DFT studies as follows. Despite the similarity of the active sites (acid-base pair) in both catalysts. However, clearly evidence shows that the behavior of the Zr_6 UiO66, which acts as an acid-base pair, is different with respect to ZrO_2 which is correlated to the higher basicity of the MOFs than the corresponding oxide as is shown in the DFT calculations presented in this study.

Table 4 Comparative study of the acidity and basicity of the active site by probing reactions

Reaction	Catalyst	Temperature (°C)	Conversion[g] (%)	Carbon Balance[h] A (%)	B (%)	Site
MPV[a] [IPA (A) + CPO (B)]	MOF (100 mg)	110	0.00	~100	~100	LAS
Alkylation[d] [Toluene (A) + CPEN (B)]	MOF (200 mg)	200	0.00	~100	~100	BAS
Dehydration[b] [CPNOL (A)]	MOF (100 mg)	250	0.00	~100	-	
Dehydration[b] [CPNOL (A)]	ZrO$_2$ (100 mg)	250	27.30	76.7	-	Acid and Basic sites
Dehydration[c] [IPA (A)]	MOF (100 mg)	250	0.00	96.8	-	
Aldol Condensation[e] [CPO (A)]	MOF (50 mg)	250	50.69	83.06	-	
Aldol Condensation[e] [CPO (A)]	MOF (50 mg)	150	5.70	90.58	-	BAS or acid-base pair
Aldol Condensation[f] [CPO (A) +Acetone (B)]	MOF (200 mg)	250	77.5	60.5	39.2	
Aldol Condensation[f] [CPO (A) +Acetone (B)]	ZrO$_2$ (100 mg)	250	71.2	75.0	71.5	

[a] Meerwein-Ponndorf-Verley reduction CPO (0.5M) and IPA used as a solvent, 1 h, 110°C and 850 psi of N$_2$
[b] Alkylation between toluene (1.0M) and CPEN (0.5M), 2 h, 200°C and 850 psi of N$_2$ using decalin as a solvent
[c] Dehydration of CPNOL (0.5M), 1 h, 250°C and 850 psi of N$_2$ using decalin as a solvent.
[d] Dehydration of IPA (0.5M), 1 h, 250°C and 850 psi of N$_2$ using decalin as a solvent.
[e] Aldol condensation of CPO (0.5M), 1 h, 250°C and 850 psi of N$_2$ using decalin as a solvent.
[f] Cross aldol condensation between CPO (0.5M) and acetone (0.5M) 1 h, 250°C and 850 psi of N$_2$ using decalin as a solvent. The conversion reported is based of CPO.
[g] The conversion was calculated as shown in the Equation (1)
[h] The carbon balance was calculated as shown in the Equation (2)

Recent studies in our group suggested that in cross condensation reaction between acetone and cyclopentanone the ratio between the cross activated products [C]C and [C]A follows the ratio of the feedstock (Cyclopentanone to Acetone) in acid catalyst as HY zeolites unlike the basic catalyst, where the yield to [C]C products is higher in comparison with the [C]A ratio. Figure 34 is presenting the ratio between those two products and is evident Zr_6-UiO66 behaves as a basic catalyst. The presented results agree with the in-situ titrations presented.
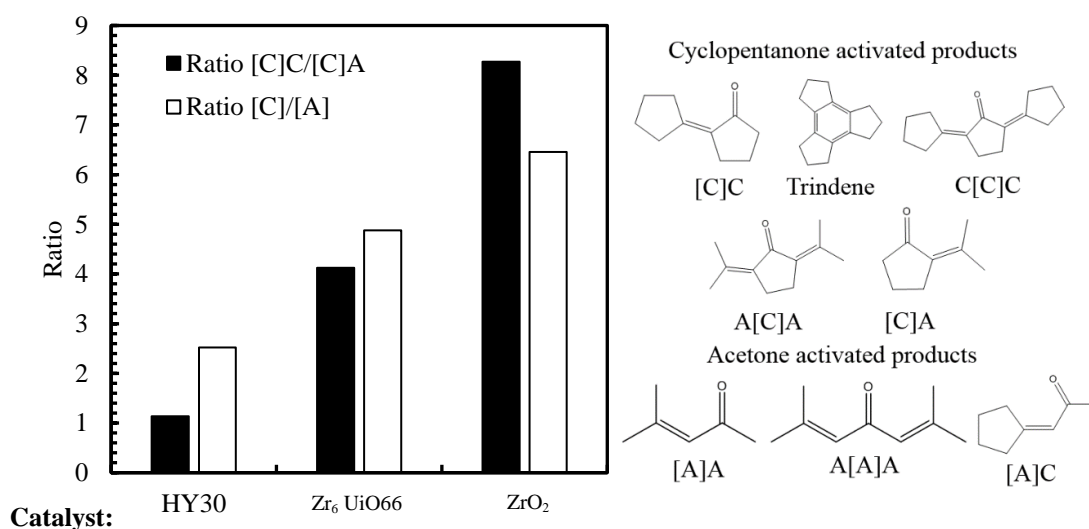
Figure 34 Ratio of [C]C to [C]A and [C] and [A] products obtained from the cross aldol condensation reaction between CPO (0.5 M) and acetone (0.5 M) at 250°C and 850 psi of N_2. The [ ] symbolize the activated product cyclopentanone [C] or acetone [A].

4.5.5. DFT calculations of the acidity and basicity on Zr_6 UiO66

As our experiments show and the literature reported[108], both acid and base sites exist in Zr_6 UiO66 with different strength. DFT calculations were carried out here to explore the nature of these possible acid/base sites. As shown in Figure 1, in the structure of the perfect Zr_6 UiO66, there's one Brønsted acid site μ3-OH, and two possible Brønsted base

sites μ3-O and Ph-O, although the protonation of Ph-O may break the linkage structure. The acidity and basicity of these three sites were thus calculated. As shown in Table 5, the deprotonation energy (*DPE*) of the μ3-OH site is calculated to be 13.24 eV, indicative of low acidity, comparing with the *DPE* of the Brønsted acid sites in the range of 10~11 eV on zeolites [133]. Similarly, the proton affinity (*PA*) of the μ3-O base site was calculated to be -11.36 eV as listed in Table 4. This value is similar to the reported *PA* of the O_{2c} sites on the rutile TiO_2 (110) surface (-11.33 eV)[134], which is the weakest base sites on rutile TiO_2 (110) and anatase TiO_2(101) surfaces, thus also indicating its weak basicity. Even weaker basicity was found at the Ph-O site with less negative PA (-10.89 eV). Both the low acidity and basicity of the acid sites and base sites in the perfect Zr_6 UiO66 suggests that they're not likely to be the active sites for the aldol condensation reactions of CPO here and other similar reactions reported in the literature[108]. This is also consistent with the above experimental observations that the μ3-OH signal in the DRIFT spectra does not change although the Zr_6 UiO66 totally loses its activity.

Similarly, in the defected Zr_6 UiO66 structure (d-Zr_6 UiO66) (Figure 23.*b*), there're two possible Brønsted acid sites: μ3-OH and d-OH. The deprotonation energy of these two sites were thus calculated as shown in Table 4. It is found that the acidity of μ3-OH near the defect site is even weaker with more positive *DPE* (13.33 eV). The 14.48 eV of *DPE* for the d-OH site indicated its almost negligible acidity. Similarly, the basicity of the μ3-O and Ph-O group near the defect sites almost does not change comparing to the perfect Zr_6 UiO66 structure with the *PA* of -11.39 eV and -10.54 eV respectively. It is noted that the d-OH can be both acid and base site, thus the *PA* of d-OH was also calculated. The *PA* of d-OH was calculated to be -12.17 eV, much more negative than the

μ3-O and Ph-O group, indicative of its stronger basicity. This *PA* value is similar to the reported O_{2c} site on the anatase $TiO_2(101)$ surface (-12.16 eV)[134], the strongest base site on the anatase $TiO_2(101)$ and rutile TiO_2 (110) surfaces. The strongest basicity of the d-OH among all the base sites suggests that it is most likely to be related to the active site of Zr_6 UiO66. This agrees with the previous experimental observations that decreasing the number of d-OH sites leads to the decreasing activity of Zr_6 UiO66.

Table 5 Summary of deprotonation energy (DPE) and proton affinity (PA) of different acid and basic sites on the Zr₆ UiO66 and defective d-Zr6 UiO66, with and without water

		DPE (eV)	PA (eV)
Zr_6UiO66	μ3-OH	13.24	-
	μ3-O	-	-11.36
	Ph-O	-	-10.89
$d\text{-}Zr_6UiO66$	μ3-OH	13.33	-
	d-OH	14.48	-12.17
	μ3-O	-	-11.39
	Ph-O	-	-10.54
$d\text{-}Zr_6UiO66\text{-}H_2O$	μ3-OH	13.39	-
	d-OH	13.46	-11.64
	d-OH₂	13.47	-
	μ3-O		-11.39
	Ph-O		-11.05

The less coordinated Zr at the defect site of Zr_6 UiO66 (d-Zr) can perform as a Lewis acid. The adsorption energy of a base molecule such as NH_3 or pyridine at the Lewis acid site is used to probe it acidity. As shown in Table 6, the adsorption energy of NH_3 at the d-Zr site is calculated to be -1.07 eV. It worth noting that the NH_3 can also

adsorbs at the μ3-OH Brønsted acid site with much less adsorption energy of -0.59 eV. This is consistent with the experimental observations of two peaks in the NH_3-TPD spectra of Zr_6 UiO66 that the first peak at about 98.8 $^{\circ}$C is attributed to the μ3-OH Brønsted acid site and the second peak at 255.3 $^{\circ}$C is attributed to the d-Zr Lewis acid site. The adsorption energy of NH_3 at the mono-ZrO_2 (111) was also calculated for comparison, which is -0.90 eV, less than its adsorption energy at the d-Zr site of Zr_6 UiO66, suggesting the stronger acidity of d-Zr in Zr_6 UiO66 than the Zr_{6c} in m-ZrO_2(111). Similar trend was found in the adsorption of pyridine at the d-Zr site of Zr_6 UiO66 and the Zr_{6c} site on m-ZrO_2(111) with the adsorption energy of -0.73 eV vs -0.61 eV as shown in Table 6.

Table 6 Adsorption energy (eV) for different molecules at the defect site of d-Zr6 UiO66 and ZrO2 (111) surface.

	d-Zr6 UiO66	*m-ZrO$_2$(111)*
CO_2	-0.45	-0.17
NH_3	-1.07	-0.90
Pyridine	-0.73	-0.61
Propionic acid	-1.36	-1.25
H_2O	-1.14	-0.84
CPO	-0.60	-0.55

The stronger acidity of the d-Zr site of Zr_6 UiO66 than the Zr_{6c} site in m-ZrO_2(111) may result in higher activity in the aldol condensation of CPO. It's been reported that the first α-H abstraction is likely to be the rate limiting step in the aldol condensation[3]. Here, the α-H abstraction reaction of CPO was conducted on both Zr_6 UiO66 and the m-ZrO_2(111) surface as shown in Figure 35. CPO firstly adsorbs at the d-Zr site of Zr_6

UiO66 with the adsorption energy of -0.60 eV. It then removes the α-H to form the enolate. The removed α-H is then bound at the d-OH site. In the transition state, the α-C-H is partially broken with the C-H elongated from 1.10 Å in the reactant to 1.37 Å, and the α-H is partially bound to the d-OH with the O-H distance of 1.25 Å. At the same time, the carbonyl O is stabilized by the d-Zr with the Zr-O distance decreased from 2.31 Å in the reactant to 2.17 Å in the transition state.
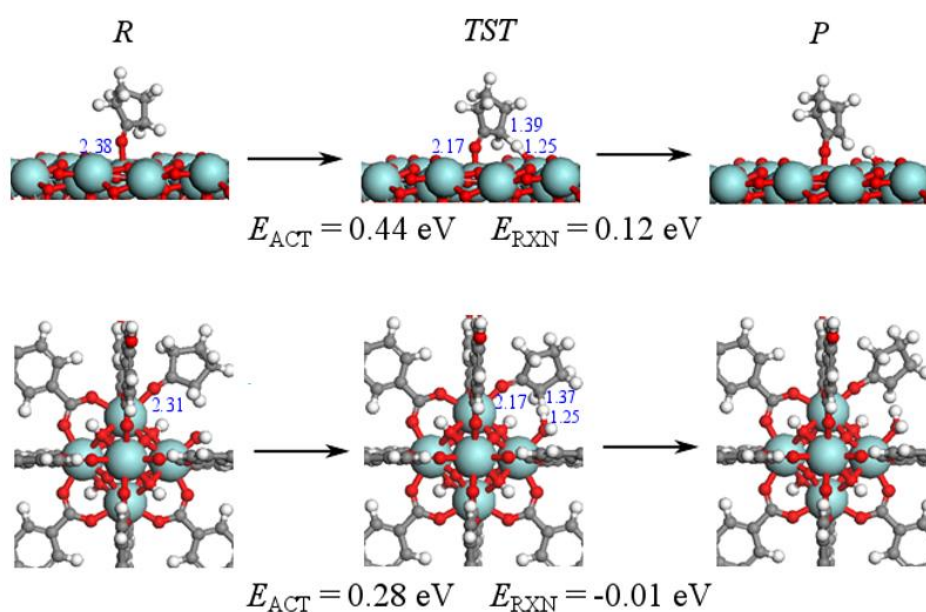
Figure 35 DFT calculations of reactant (R), transition state (TST) and product (P) for the first step in aldol condensation corresponding to the abstraction of an α-H from CPO over ZrO2 (top) and d-Zr6 UiO66 (bottom).

This transition state structure suggests that both a stronger acid and a stronger base can help facilitate the transition state, and hence lower the energy barrier. The energy barrier for the α-H abstraction of CPO on Zr_6 UiO66 is calculated to be 0.28 eV and the reaction energy is calculated to -0.01 eV. The transition state structure for the α-H abstraction of CPO on m-ZrO_2(111) is similar to that on Zr_6 UiO66 as shown in Figure 35. However, the energy barrier is higher (0.44 eV) and the reaction energy is also higher

(0.12 eV). This is consistent with the acidity trend we showed above. This also agrees with the experiment that Zr_6 UiO66 is more active than ZrO_2 in the aldol condensation of CPO with higher TOF.

Finally, the adsorption of propionic acid and water on the Zr_6 UiO66 were calculated as shown in Table 6. Both the propionic acid and H_2O adsorb at the d-Zr and d-OH acid-base pairs of Zr_6 UiO66 strongly with the adsorption energy of -1.36 eV and -1.14 eV respectively, which are higher than the adsorption energy of CPO (-0.60 eV). The strong bonding of propionic acid and H_2O and the d-Zr and d-OH acid-base pair explains our experimental observation that the addition of propionic acid or H_2O can deactivate the aldol condensation reaction of CPO over Zr_6 UiO66.

4.6. Conclusions

In conclusion, the Zr_6-based metal-organic frameworks UiO66 showed high catalytic activity for the aldol condensation of biomass-derived cyclopentanone, thus provides a promising route for the synthesis of high-density biofuel over MOF-based catalysts. In addition, we developed the strategy to combine different experimental techniques with DFT calculations in an interactive and synergic way to disclose and fully understand the nature of the active sites in Zr_6 UiO66. Using this technique, the plausible active site in the Zr_6 UiO66 has been assigned to the "acid-base" pair of the less coordinated Zr (acid) and the OH (base) at the defect sites. The energy barriers for the H-abstraction reaction of CPO over Zr_6 UiO66 is calculated to be lower than over m-ZrO_2, which agrees with the experimental observation that much higher activity of Zr_6 UiO66 than ZrO_2 in the aldol condensation of CPO. The understanding of the active sites in the Zr_6

UiO66 is very crucial for its future application as catalyst in other important reactions as

well as other MOF structures.

APENDIX

Apendix A: Thermal Stability of MCM-41-SO₃H (CG)

Catalytic measurements

The catalytic activity was evaluated trough the liquid phase dehydration in a Mini Bench Top Parr pressure reactor of 160 mL (Model Parr 4564) equipped with a Parr 4848 Reactor Controller for temperature, stirring and a transducer for pressure measurement. In a typical experiment, the functionalized mesostructured silica (150 mg) were mixed with the reaction solvent (decahydronaphthalene, 80 mL) in the reaction vessel. The reactor was sealed and pressurized with 300 psi and heated up to the reaction temperature. In a separated vessel, a solution, in base with reaction conditions, of 0.5 M of 1,3 methyl cyclohexanol was prepared. The solvent was added until complete 100 mL of total volume in the reaction. The resulted solution, was placed in a separated pressurized cylinder (1000 psi of N_2) and injected into the reactor reaching a final pressure of 800 psi and stirred at 425 rpm. After the reaction, the stirring and temperature was stopped and the reactor was cooldown to room temperature, the solid were separated from the reaction mixture using a syringe filtration system with a PTFE filter of 0.22 µm. The collected liquid was analyzed with a GC-FID (Phenol was used as a GC internal standard) equipped with a Phenomenex capillary column (ZB-1701, 15 m x 0.25 mm x 0.25 µm). The product identification was carried out with GC-MS equipped with the same column described above.

Thermal Stability

The MCM-41-SO$_3$H was fabricated at mentioned in the *Chapter 3* with an acid density of 0.505 mmol H$^+$/g cat determined by TGA. The solid was pretreated under N$_2$ environment at different temperatures for 6 h and the results are presented in the Figure 36. Initially, the catalyst lost some of the activity that is attributed to the leaching of the most external physisorbed functionalization. However, the catalyst results stable under temperatures of 320° after of this temperature the activity of the catalyst decreases around 50% because of the thermal decomposition and subsequent loss of the functionalization. No leaching was observed due of the non/polar nature of the reaction environment.
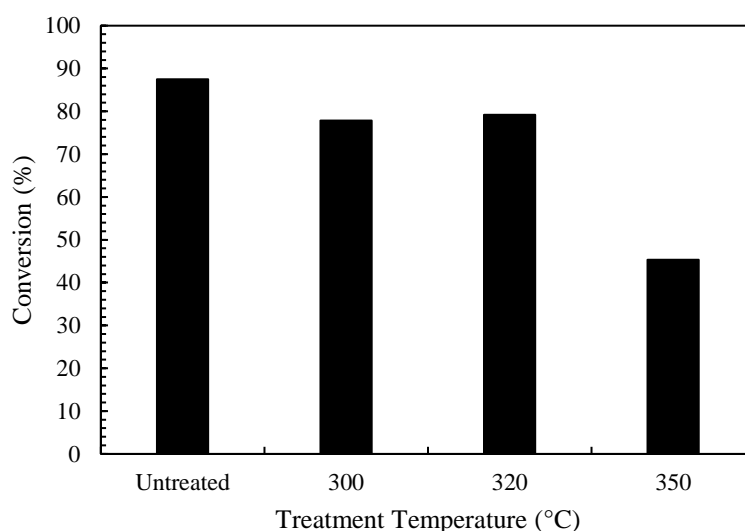

Figure 36 Catalytic activity of MCM-41-SO$_3$H (CG) for the dehydration of 1,3 methyl cyclohexanol (0.5M) to 1,3 methyl cyclohexene at 200°C and 800 psi of N$_2$ after thermal treatment at 300°C, 320°C and 350°C under inert atmosphere.

REFERENCES

1. Basu, P. & Basu, P. in *Biomass Gasification and Pyrolysis* 117–165 (2010). doi:10.1016/B978-0-12-374988-8.00005-2
2. Bridgwater, A. . & Peacocke, G. V. . Fast pyrolysis processes for biomass. *Renew. Sustain. Energy Rev.* **4,** 1–73 (2000).
3. Wang, S., Goulas, K. & Iglesia, E. Condensation and esterification reactions of alkanals, alkanones, and alkanols on TiO2: Elementary steps, site requirements, and synergistic effects of bifunctional strategies. *J. Catal.* **340,** 302–320 (2016).
4. U.S. Energy Information Administration. Monthly Crude Oil and Natural Gas Productionle. (2017). Available at: https://www.eia.gov/petroleum/production/. (Accessed: 1st January 2017)
5. Huber, G. W. & Dumesic, J. A. An overview of aqueous-phase catalytic processes for production of hydrogen and alkanes in a biorefinery. *Catal. Today* **111,** 119–132 (2006).
6. Bui, T. V., Crossley, S. & Resasco, D. E. *Chemicals and Fuels from Bio-Based Building Blocks.* (Wiley-VCH Verlag GmbH & Co. KGaA, 2016). doi:10.1002/9783527698202
7. Yaman, S. Pyrolysis of biomass to produce fuels and chemical feedstocks. *Energy Convers. Manag.* **45,** 651–671 (2004).
8. Perlack, R. D., L.L. Wright, A. . & Turhollow, R. L. G. Biomass as Feedstock for a Bioenergy and Bioproducts Industry: The Technical Feasibility of a Billion-Ton Annual Supply. *U.S. Department of Agriculture* (2005).
9. U.S. Government. Biomass Research and Development Technical Advsiory Committee Roadmap for Biomass Technologies in the U.S,. (2002). Available at: http://www1.eere.energy.gov/biomass/publications.html.
10. Stöcker, M. Methanol-to-hydrocarbons: catalytic materials and their behavior. *Microporous Mesoporous Mater.* **29,** 3–48 (1999).
11. Higman, van der B. *Gasification. Gulf Professional Publishing* (Elseiver, 2008).
12. Klass, D. . Biomass for Renewable Energy, Fuels, and Chemicals. *Acad. Press* (1998).
13. Knoef, H. A. M. *Handbook Biomass Gasification.* (BTG Publisher, 2005).
14. Couto, N., Rouboa, A., Silva, V., Monteiro, E. & Bouziane, K. Influence of the Biomass Gasification Processes on the Final Composition of Syngas. *Energy Procedia* **36,** 596–606 (2013).
15. Resasco, D. E. & Crossley, S. P. Implementation of concepts derived from model compound studies in the separation and conversion of bio-oil to fuel. *Catal. Today* **257,** 185–199 (2015).
16. Pollard, A. S., Rover, M. R. & Brown, R. C. Characterization of bio-oil recovered as stage fractions with unique chemical and physical properties. *J. Anal. Appl. Pyrolysis* **93,** 129–138 (2012).
17. Pham, T. N., Shi, D. & Resasco, D. E. Evaluating strategies for catalytic upgrading of pyrolysis oil in liquid phase. *Appl. Catal. B Environ.* **145,** 10–23 (2014).
18. Pham, T. N., Sooknoi, T., Crossley, S. P. & Resasco, D. E. Ketonization of Carboxylic Acids: Mechanisms, Catalysts, and Implications for Biomass Conversion. *ACS Catal.* **3,** 2456–2473 (2013).

19.	Liu, Q., Wang, S., Zheng, Y., Luo, Z. & Cen, K. Mechanism study of wood lignin pyrolysis by using TG–FTIR analysis. *J. Anal. Appl. Pyrolysis* **82,** 170–177 (2008).

20.	Bejblová, M., Procházková, D. & Cejka, J. Acylation reactions over zeolites and mesoporous catalysts. *ChemSusChem* **2,** 486–99 (2009).

21.	Gumidyala, A., Wang, B. & Crossley, S. Direct carbon-carbon coupling of furanics with acetic acid over Bronsted zeolites. *Sci. Adv.* **2,** e1601072–e1601072 (2016).

22.	Nie, L. & Resasco, D. E. Improving carbon retention in biomass conversion by alkylation of phenolics with small oxygenates. *Appl. Catal. A Gen.* **447–448,** 14–21 (2012).

23.	Gonzalez-Borja, M. Á. & Resasco, D. E. Reaction Pathways in the Liquid Phase Alkylation of Biomass-Derived Phenolic Compounds. *AIChE J.* **61,** 598–609 (2015).

24.	Hronec, M. & Fulajtarová, K. *Selective transformation of furfural to cyclopentanone*. *Catalysis Communications* **24,** (2012).

25.	Pham, T. N., Shi, D., Sooknoi, T. & Resasco, D. E. Aqueous-phase ketonization of acetic acid over Ru/TiO2/carbon catalysts. *J. Catal.* **295,** 169–178 (2012).

26.	Gumidyala, A., Sooknoi, T. & Crossley, S. Selective ketonization of acetic acid over HZSM-5: The importance of acyl species and the influence of water. *J. Catal.* **340,** 76–84 (2016).

27.	Guo, J. *et al.* Selective Conversion of Furfural to Cyclopentanone with CuZnAl Catalysts. *ACS Sustain. Chem. Eng.* **2,** 2259–2266 (2014).

28.	Hronec, M. *et al.* Carbon supported Pd–Cu catalysts for highly selective rearrangement of furfural to cyclopentanone. *Appl. Catal. B Environ.* **181,** 210–219 (2016).

29.	Nakagawa, Y., Tamura, M. & Tomishige, K. Catalytic Reduction of Biomass-Derived Furanic Compounds with Hydrogen. *ACS Catal.* **3,** 2655–2668 (2013).

30.	Wang, S., Vorotnikov, V. & Vlachos, D. G. Coverage-Induced Conformational Effects on Activity and Selectivity: Hydrogenation and Decarbonylation of Furfural on Pd(111). *ACS Catal.* **5,** 104–112 (2015).

31.	Vorotnikov, V., Mpourmpakis, G. & Vlachos, D. G. DFT Study of Furfural Conversion to Furan, Furfuryl Alcohol, and 2-Methylfuran on Pd(111). *ACS Catal.* **2,** 2496–2504 (2012).

32.	Taylor, M. J. *et al.* Catalytic Hydrogenation and Hydrodeoxygenation of Furfural over Pt(111): A Model System for the Rational Design and Operation of Practical Biomass Conversion Catalysts. *J. Phys. Chem. C* **121,** 8490–8497 (2017).

33.	Audemar, M. *et al.* Selective Hydrogenation of Furfural to Furfuryl Alcohol in the Presence of a Recyclable Cobalt/SBA-15 Catalyst. *ChemSusChem* **8,** 1885–1891 (2015).

34.	Corma, A., de la Torre, O., Renz, M. & Villandier, N. Production of High-Quality Diesel from Biomass Waste Products. *Angew. Chemie Int. Ed.* **50,** 2375–2378 (2011).

35.	Boonyasuwat, S., Omotoso, T., Resasco, D. E. & Crossley, S. P. Conversion of Guaiacol over Supported Ru Catalysts. *Catal. Letters* **143,** 783–791 (2013).

36.	Santillini, D. The mechanism of aromatic transalkylation in ZSM-5. *J. Catal.* **99,** 327–334 (1986).

37.	Zapata, P. A., Huang, Y., Gonzalez-Borja, M. A. & Resasco, D. E. Silylated

hydrophobic zeolites with enhanced tolerance to hot liquid water. *J. Catal.* **308,** 82–97 (2013).

38. Zapata, P. A., Faria, J., Ruiz, M. P., Jentoft, R. E. & Resasco, D. E. Hydrophobic Zeolites for Biofuel Upgrading Reactions at the Liquid–Liquid Interface in Water/Oil Emulsions. *J. Am. Chem. Soc.* **134,** 8570–8578 (2012).

39. Ehrhardt, K., Suckow, M. & Lutz, W. Hydrothermal decomposition of aluminosilicate zeolites and prediction of their long-term stability. *Stud. Surf. Sci. Catal.* **94,** 179–186 (1995).

40. Ravenelle, R. M. *et al.* Stability of Zeolites in Hot Liquid Water. *J. Phys. Chem. C* **114,** 19582–19595 (2010).

41. Hoffmann, F., Cornelius, M., Morell, J. & Fröba, M. Silica-based mesoporous organic-inorganic hybrid materials. *Angew. Chem. Int. Ed. Engl.* **45,** 3216–51 (2006).

42. Gholamzadeh, P., Mohammadi Ziarani, G., Lashgari, N., Badiei, A. & Asadiatouei, P. Silica functionalized propyl sulfonic acid (SiO2-Pr-SO3H): An efficient catalyst in organic reactions. *J. Mol. Catal. A Chem.* **391,** 208–222 (2014).

43. Mohammadi Ziarani, G., Lashgari, N. & Badiei, A. Sulfonic acid-functionalized mesoporous silica (SBA-Pr-SO3H) as solid acid catalyst in organic reactions. *J. Mol. Catal. A Chem.* **397,** 166–191 (2015).

44. Sad, M. E., Neurock, M. & Iglesia, E. Formation of C–C and C–O Bonds and Oxygen Removal in Reactions of Alkanediols, Alkanols, and Alkanals on Copper Catalysts. *J. Am. Chem. Soc.* **133,** 20384–20398 (2011).

45. Gürbüz, E. I., Hibbitts, D. D. & Iglesia, E. Kinetic and Mechanistic Assessment of Alkanol/Alkanal Decarbonylation and Deoxygenation Pathways on Metal Catalysts. *J. Am. Chem. Soc.* **137,** 11984–11995 (2015).

46. Herrmann, S. & Iglesia, E. Elementary steps in acetone condensation reactions catalyzed by aluminosilicates with diverse void structures. *J. Catal.* **346,** 134–153 (2017).

47. Nitta, M., Aomura, K. & Yamaguchi, K. Alkylation of Phenols. II. The Selective Formation of Thymol from m-Cresol and Propylene with a γ-Alumina Catalyst. *Bull. Chem. Soc. Jpn.* **47,** 2630–2364 (1974).

48. Grabowska, H., Syper, L. & Zawadzki, M. Vapour phase alkylation of ortho-, meta- and para-cresols with isopropyl alcohol in the presence of sol–gel prepared alumina catalyst. *Appl. Catal. A Gen.* **277,** 91–97 (2004).

49. Grabowska, H., Miśta, W., Trawczyński, J., Wrzyszcz, J. & Zawadzki, M. A method for obtaining thymol by gas phase catalytic alkylation of m-cresol over zinc aluminate spinel. *Appl. Catal. A Gen.* **220,** 207–213 (2001).

50. Ryoo, R. & Jun, S. Improvement of Hydrothermal Stability of MCM-41 Using Salt Effects during the Crystallization Process. *J. Phys. Chem. B* **101,** 317–320 (1997).

51. Sander, R. Compilation of Henry's law constants (version 4.0) for water as solvent. *Atmos. Chem. Phys* **15,** 4399–4981 (2015).

52. Bali, S., Leisen, J., Foo, G. S., Sievers, C. & Jones, C. W. Aminosilanes Grafted to Basic Alumina as CO 2 Adsorbents-Role of Grafting Conditions on CO 2 Adsorption Properties. *ChemSusChem* **7,** 3145–3156 (2014).

53. Brunelli, N. A., Venkatasubbaiah, K. & Jones, C. W. Cooperative Catalysis with Acid–Base Bifunctional Mesoporous Silica: Impact of Grafting and Co-

condensation Synthesis Methods on Material Structure and Catalytic Properties. *Chem. Mater.* **24,** 2433–2442 (2012).

54. Davis, M. E., Jones, C. W. & Tsuji, K. Organic-functionalized molecular sieves as shape-selective catalysts. *Nature* **393,** 52–54 (1998).

55. Taborga Claure, M. *et al.* Tuning of higher alcohol selectivity and productivity in CO hydrogenation reactions over K/MoS2 domains supported on mesoporous activated carbon and mixed MgAl oxide. *J. Catal.* **324,** 88–97 (2015).

56. Rahmat, N., Abdullah, A. Z. & Mohamed, A. R. A Review: Mesoporous Santa Barbara Amorphous-15, Types, Synthesis and Its Applications towards Biorefinery Production. *Am. J. Appl. Sci.* **7,** 1579–1586 (2010).

57. Carniato, F. *et al.* On the hydrothermal stability of MCM-41 mesoporous silica nanoparticles and the preparation of luminescent materials. *J. Mater. Chem.* **20,** 5504 (2010).

58. van der Graaff, W. N. P., Olvera, K. G., Pidko, E. A. & Hensen, E. J. M. Stability and catalytic properties of porous acidic (organo)silica materials for conversion of carbohydrates. *J. Mol. Catal. A Chem.* **388,** 81–89 (2014).

59. Kim, J. M., Kwak, J. H., Jun, S. & Ryoo, R. Ion Exchange and Thermal Stability of MCM-41. *J. Phys. Chem.* **99,** 16742–16747 (1995).

60. Tatsumi, T., Koyano, K. A., Tanaka, Y. & Nakata, S. Mechanical Stability of Mesoporous Materials, MCM-48 and MCM-41. *J. Porous Mater.* **6,** 13–17 (1999).

61. Gusev, V. Y., Feng, X., Bu, Z., Haller, G. L. & O'Brien, J. A. Mechanical Stability of Pure Silica Mesoporous MCM-41 by Nitrogen Adsorption and Small-Angle X-ray Diffraction Measurements. *J. Phys. Chem.* **100,** 1985–1988 (1996).

62. Galacho, C., Ribeiro Carrott, M. M. L. & Carrott, P. J. M. Evaluation of the thermal and mechanical stability of Si-MCM-41 and Ti-MCM-41 synthesised at room temperature. *Microporous Mesoporous Mater.* **108,** 283–293 (2008).

63. Das, D., Lee, J.-F. & Cheng, S. Selective synthesis of Bisphenol-A over mesoporous MCM silica catalysts functionalized with sulfonic acid groups. *J. Catal.* **223,** 152–160 (2004).

64. M. Van Rhijn, W. *et al.* Sulfonic acid functionalised ordered mesoporous materials as catalysts for condensation and esterification reactions. *Chem. Commun.* 317–318 (1998). doi:10.1039/a707462j

65. Dacquin, J. P., Lee, A. F., Pirez, C. & Wilson, K. Pore-expanded SBA-15 sulfonic acid silicas for biodiesel synthesis. *Chem. Commun.* **48,** 212–214 (2012).

66. Grieken, R. van, Melero, J. A. & Morales, G. Fries rearrangement of phenyl acetate over sulfonic modified mesostructured SBA-15 materials. *Appl. Catal. A Gen.* **289,** 143–152 (2005).

67. Karaki, M. *et al.* Synthesis and characterization of acidic ordered mesoporous organosilica SBA-15: Application to the hydrolysis of cellobiose and insight into the stability of the acidic functions. *J. Catal.* **305,** 204–216 (2013).

68. García, N. *et al.* Functionalization of SBA-15 by an acid-catalyzed approach: A surface characterization study. *Microporous Mesoporous Mater.* **106,** 129–139 (2007).

69. Huang, Y. Functionalization of mesoporous silica nanoparticles and their applications in organo-, metallic and organometallic catalysis. *Functionalization of mesoporous silica nanoparticles and their applications in organo-, metallic and*

organometallic catalysis (Iowa University, 2009).

70. Gholami, M., Talaie, M. R. & Aghamiri, S. F. CO2 adsorption on amine functionalized MCM-41: Effect of bi-modal porous structure. *J. Taiwan Inst. Chem. Eng.* (2015). doi:10.1016/j.jtice.2015.07.021

71. Qisheng Huo, †, David I. Margolese, † & and Galen D. Stucky* †, ‡. Surfactant Control of Phases in the Synthesis of Mesoporous Silica-Based Materials. *Chem. Mater.* **8,** 1147–1160 (1996).

72. Testa, M. L., La Parola, V. & Venezia, A. M. Transesterification of short chain esters using sulfonic acid-functionalized hybrid silicas: Effect of silica morphology. *Catal. Today* **223,** 115–121 (2014).

73. Canilho, N. *et al.* Isocyanate-mediated covalent immobilization of Mucor miehei lipase onto SBA-15 for transesterification reaction. *Colloids Surfaces B Biointerfaces* **112,** 139–145 (2013).

74. Samolada, M. Selective O-Alkylation of Phenol with Methanol over Sulfates Supported on γ-Al2O3. *J. Catal.* **152,** 52–62 (1995).

75. Chen, S.-Y. *et al.* Sulfonic acid-functionalized platelet SBA-15 materials as efficient catalysts for biodiesel synthesis. *Green Chem.* **13,** 2920 (2011).

76. Margolese, D., Melero, J. A., Christiansen, S. C., Chmelka, B. F. & Stucky, G. D. Direct Syntheses of Ordered SBA-15 Mesoporous Silica Containing Sulfonic Acid Groups. *Chem. Mater.* **12,** 2448–2459 (2000).

77. Zhao, X. S., Lu, G. Q., Whittaker, A. K., Millar, G. J. & Zhu, § and H. Y. Comprehensive Study of Surface Chemistry of MCM-41 Using 29Si CP/MAS NMR, FTIR, Pyridine-TPD, and TGA. *J. Phys. Chem. B* **101,** 6525–6531 (1997).

78. Chen, C.-Y., Burkett, S. L., Li, H.-X. & Davis, M. E. Studies on mesoporous materials II. Synthesis mechanism of MCM-41. *Microporous Mater.* **2,** 27–34 (1993).

79. Kailasam, K. & Müller, K. Physico-chemical characterization of MCM-41 silica spheres made by the pseudomorphic route and grafted with octadecyl chains. *J. Chromatogr. A* **1191,** 125–135 (2008).

80. Chen, C.-Y., Li, H.-X. & Davis, M. E. Studies on mesoporous materials: I. Synthesis and characterization of MCM-41. *Microporous Mater.* **2,** 17–26 (1993).

81. Ortlam, A., Rathouský, J., Schulz-Ekloff, G. & Zukal, A. MCM-41 as-synthesized and calcined materials: temporal development of X-ray reflection intensity and pore volume. *Microporous Mater.* **6,** 171–180 (1996).

82. Dasgupta, D. *et al.* in *Progress in Rubber Nanocomposites* 231–247 (2017). doi:10.1016/B978-0-08-100409-8.00007-3

83. Zhang, W., Camino, G. & Yang, R. Polymer/polyhedral oligomeric silsesquioxane (POSS) nanocomposites: An overview of fire retardance. *Prog. Polym. Sci.* (2016). doi:10.1016/j.progpolymsci.2016.09.011

84. Yang, Q.-H., Ma, Z.-H., Ma, J.-Z. & Nie, J. Mesoporous silica supported water-stable perfluorobutylsulfonylimide and its catalytic applications in esterification. *Microporous Mesoporous Mater.* **172,** 51–60 (2013).

85. Hoffmann, F., Cornelius, M., Morell, J. & Fröba, M. Silica-Based Mesoporous Organic–Inorganic Hybrid Materials. *Angew. Chemie Int. Ed.* **45,** 3216–3251 (2006).

86. Cano-Serrano, E., Blanco-Brieva, G., Campos-Martin, J. M. & Fierro, J. L. G.

Acid-Functionalized Amorphous Silica by Chemical Grafting−Quantitative Oxidation of Thiol Groups. *Langmuir* **19,** 7621–7627 (2003).

87.   González, M. D., Cesteros, Y., Llorca, J. & Salagre, P. Boosted selectivity toward high glycerol tertiary butyl ethers by microwave-assisted sulfonic acid-functionalization of SBA-15 and beta zeolite. *J. Catal.* **290,** 202–209 (2012).

88.   Zeidan, R. K. & Davis, M. E. *The effect of acid–base pairing on catalysis: An efficient acid–base functionalized catalyst for aldol condensation*. *Journal of Catalysis* **247,** (2007).

89.   Zhang, X., Zhang, L. & Yang, Q. Designed synthesis of sulfonated polystyrene/mesoporous silica hollow nanospheres as efficient solid acid catalysts. *J. Mater. Chem. A* **2,** 7546 (2014).

90.   Mbaraka, I. K., McGuire, K. J. & Shanks, B. H. Acidic Mesoporous Silica for the Catalytic Conversion of Fatty Acids in Beef Tallow. *Ind. Eng. Chem. Res.* **45,** 3022–3028 (2006).

91.   Peña, L., Hohn, K. L., Li, J., Sun, X. S. & Wang, D. Synthesis of Propyl-Sulfonic Acid-Functionalized Nanoparticles as Catalysts for Cellobiose Hydrolysis. *J. Biomater. Nanobiotechnol.* **5,** 241–253 (2014).

92.   Yaghi, O. M. *et al.* Reticular synthesis and the design of new materials. *Nature* **423,** 705–714 (2003).

93.   Li, H., Eddaoudi, M., O'Keeffe, M. & Yaghi, O. M. Design and synthesis of an exceptionally stable and highly porous metal-organic framework. *Nature* **402,** 276–279 (1999).

94.   Long, J. R. & Yaghi, O. M. The pervasive chemistry of metal-organic frameworks. *Chem. Soc. Rev.* **38,** 1213–1214 (2009).

95.   Furukawa, H., Cordova, K. E., O'Keeffe, M. & Yaghi, O. M. The Chemistry and Applications of Metal-Organic Frameworks. *Science (80-.).* **341,** (2013).

96.   Zhou, H.-C. 'Joe' & Kitagawa, S. Metal–Organic Frameworks (MOFs). *Chem. Soc. Rev.* **43,** 5415–5418 (2014).

97.   Slater, A. G. & Cooper, A. I. Function-led design of new porous materials. *Science (80-.).* **348,** aaa8075-aaa8075 (2015).

98.   Corma, A., García, H. & Llabrés i Xamena, F. X. Engineering Metal Organic Frameworks for Heterogeneous Catalysis. *Chem. Rev.* **110,** 4606–4655 (2010).

99.   Hu, Z. & Zhao, D. De facto methodologies toward the synthesis and scale-up production of UiO-66-type metal–organic frameworks and membrane materials. *Dalt. Trans.* **44,** 19018–19040 (2015).

100.   Vermoortele, F. *et al.* Synthesis Modulation as a Tool To Increase the Catalytic Activity of Metal–Organic Frameworks: The Unique Case of UiO-66(Zr). *J. Am. Chem. Soc.* **135,** 11465–11468 (2013).

101.   Cavka, J. H. *et al.* A New Zirconium Inorganic Building Brick Forming Metal Organic Frameworks with Exceptional Stability. *J. Am. Chem. Soc.* **130,** 13850–13851 (2008).

102.   Schaate, A. *et al.* Modulated Synthesis of Zr-Based Metal-Organic Frameworks: From Nano to Single Crystals. *Chem. - A Eur. J.* **17,** 6643–6651 (2011).

103.   Kandiah, M. *et al.* Synthesis and Stability of Tagged UiO-66 Zr-MOFs. *Chem. Mater.* **22,** 6632–6640 (2010).

104.   Wu, H. *et al.* Unusual and Highly Tunable Missing-Linker Defects in Zirconium

Metal–Organic Framework UiO-66 and Their Important Effects on Gas Adsorption. *J. Am. Chem. Soc.* **135,** 10525–10532 (2013).

105. Katz, M. J. *et al.* A facile synthesis of UiO-66, UiO-67 and their derivatives. *Chem. Commun.* **49,** 9449 (2013).

106. Lammert, M. *et al.* Cerium-based metal organic frameworks with UiO-66 architecture: synthesis, properties and redox catalytic activity. *Chem. Commun.* **51,** 12578–12581 (2015).

107. Kim, J., Kim, S.-N., Jang, H.-G., Seo, G. & Ahn, W.-S. CO2 cycloaddition of styrene oxide over MOF catalysts. *Appl. Catal. A Gen.* **453,** 175–180 (2013).

108. Timofeeva, M. N. *et al.* Effects of linker substitution on catalytic properties of porous zirconium terephthalate UiO-66 in acetalization of benzaldehyde with methanol. *Appl. Catal. A Gen.* **471,** 91–97 (2014).

109. Panchenko, V. N. *et al.* Catalytic behavior of metal–organic frameworks in the Knoevenagel condensation reaction. *J. Catal.* **316,** 251–259 (2014).

110. Hajek, J. *et al.* Mechanistic studies of aldol condensations in UiO-66 and UiO-66-NH 2 metal organic frameworks. *J. Catal.* **331,** 1–12 (2015).

111. Canivet, J., Vandichel, M. & Farrusseng, D. Origin of highly active metal–organic framework catalysts: defects? Defects! *Dalt. Trans.* **45,** 4090–4099 (2016).

112. Klet, R. C., Liu, Y., Wang, T. C., Hupp, J. T. & Farha, O. K. Evaluation of Brønsted acidity and proton topology in Zr- and Hf-based metal–organic frameworks using potentiometric acid–base titration. *J. Mater. Chem. A* **4,** 1479–1485 (2016).

113. Yang, J. *et al.* Synthesis of Jet-Fuel Range Cycloalkanes from the Mixtures of Cyclopentanone and Butanal. *Ind. Eng. Chem. Res.* **54,** 11825–11837 (2015).

114. Shearer, G. C. *et al.* Defect Engineering: Tuning the Porosity and Composition of the Metal–Organic Framework UiO-66 via Modulated Synthesis. *Chem. Mater.* **28,** 3749–3761 (2016).

115. Kresse, G. & Hafner, J. Ab initio molecular dynamics for liquid metals. *Phys. Rev. B* **47,** 558–561 (1993).

116. Kresse, G. & Hafner, J. Ab initio molecular-dynamics simulation of the liquid-metal–amorphous-semiconductor transition in germanium. *Phys. Rev. B* **49,** 14251–14269 (1994).

117. Perdew, J. P., Burke, K. & Ernzerhof, M. Generalized Gradient Approximation Made Simple. *Phys. Rev. Lett.* **77,** 3865–3868 (1996).

118. Kresse, G. & Joubert, D. From ultrasoft pseudopotentials to the projector augmented-wave method. *Phys. Rev. B* **59,** 1758–1775 (1999).

119. Monkhorst, H. J. & Pack, J. D. Special points for Brillouin-zone integrations. *Phys. Rev. B* **13,** 5188–5192 (1976).

120. Henkelman, G. & Jónsson, H. A dimer method for finding saddle points on high dimensional potential surfaces using only first derivatives. *J. Chem. Phys.* **111,** 7010–7022 (1999).

121. Henkelman, G. & Jónsson, H. Improved tangent estimate in the nudged elastic band method for finding minimum energy paths and saddle points. *J. Chem. Phys.* **113,** 9978–9985 (2000).

122. Valenzano, L. *et al.* Disclosing the Complex Structure of UiO-66 Metal Organic Framework: A Synergic Combination of Experiment and Theory. *Chem. Mater.*

23, 1700–1718 (2011).

123. Shearer, G. C. *et al.* Tuned to Perfection: Ironing Out the Defects in Metal–Organic Framework UiO-66. *Chem. Mater.* **26,** 4068–4071 (2014).

124. Yang, D. *et al.* Tuning Zr 6 Metal–Organic Framework (MOF) Nodes as Catalyst Supports: Site Densities and Electron-Donor Properties Influence Molecular Iridium Complexes as Ethylene Conversion Catalysts. *ACS Catal.* **6,** 235–247 (2016).

125. Planas, N. *et al.* Defining the Proton Topology of the Zr 6 -Based Metal–Organic Framework NU-1000. *J. Phys. Chem. Lett.* **5,** 3716–3723 (2014).

126. Jiang, G. *et al.* Highly effective P-modified HZSM-5 catalyst for the cracking of C4 alkanes to produce light olefins. *Appl. Catal. A Gen.* **340,** 176–182 (2008).

127. Topsøe, N.-Y., Pedersen, K. & Derouane, E. G. Infrared and temperature-programmed desorption study of the acidic properties of ZSM-5-type zeolites. *J. Catal.* **70,** 41–52 (1981).

128. Zhang, L., Chen, K., Chen, B., White, J. L. & Resasco, D. E. Factors that Determine Zeolite Stability in Hot Liquid Water. *J. Am. Chem. Soc.* **137,** 11810–11819 (2015).

129. Corma, A., Domine, M. E., Nemeth, L. & Valencia, S. Al-Free Sn-Beta Zeolite as a Catalyst for the Selective Reduction of Carbonyl Compounds (Meerwein−Ponndorf−Verley Reaction). *J. Am. Chem. Soc.* **124,** 3194–3195 (2002).

130. Román-Leshkov, Y. & Davis, M. E. Activation of Carbonyl-Containing Molecules with Solid Lewis Acids in Aqueous Media. *ACS Catal.* **1,** 1566–1580 (2011).

131. Gounder, R. & Iglesia, E. Catalytic Alkylation Routes via Carbonium-Ion-Like Transition States on Acidic Zeolites. *ChemCatChem* **3,** 1134–1138 (2011).

132. Huber, G. W., Chheda, J., Barrett, C. & Dumesic, J. A. Production of Liquid Alkanes by Aqueous-Phase Processing of Biomass-Derived Carbohydrates. *Science (80-.).* **308,** 1446–1450 (2005).

133. Janik, M. J., Macht, J., Iglesia, E. & Neurock, M. Correlating Acid Properties and Catalytic Function: A First-Principles Analysis of Alcohol Dehydration Pathways on Polyoxometalates. *J. Phys. Chem. C* **113,** 1872–1885 (2009).

134. Wang, S. & Iglesia, E. Experimental and theoretical assessment of the mechanism and site requirements for ketonization of carboxylic acids on oxides. *J. Catal.* **345,** 183–206 (2017).